TU Delft Delft University of Technology

Solidification cracking during laser beam welding

A study on advanced high strength steels

Arjun Sood

Materials Science & Engineering

SOLIDIFICATION CRACKING DURING LASER BEAM WELDING

A STUDY ON ADVANCED HIGH STRENGTH STEELS

by

Arjun Sood

in partial fulfillment of the requirements for the degree of

Master of Science

in Materials Science and Engineering at the Delft University of Technology,

to be defended publicly on **14 July, 2020**.

Student number	4736389
Project duration	August 2019 – June 2020

Daily Supervisors

Dr. Marcel Hermans,	Delft University of Technology.
Dr. Gautam Agarwal,	Delft University of technology.

Thesis Committee

Dr. Marcel Hermans,	Delft University of Technology.
Dr. Jie Zhou,	Delft University of Technology.
Dr. Gautam Agarwal,	Delft University of Technology.
Dr. He Gao,	Tata Steel Europe.

TU Delft

CONTENTS

Abstract vii

Acknowledgements ix

List of Figures xi

List of Tables xv

1 Introduction 1

1.1 **Introduction** . . . 1

1.2 **Research goals** . . . 3

1.3 **Outline of the report** . . . 3

2 Theoretical background 5

2.1 **Laser beam welding** . . . 5

2.1.1 **Laser beam welding operation modes** . . . 6

2.1.2 **Laser beam spot size adjustment** . . . 7

2.1.3 **Features of the weldment** . . . 8

2.2 **Advanced high strength steels** . . . 9

2.2.1 **First generation AHSS** . . . 10

2.2.2 **Second Generation AHSS** . . . 10

2.2.3 **Third Generation AHSS** . . . 11

2.3 **Introduction to solidification cracking** . . . 13

2.3.1 **Theories on Solidification cracking** . . . 14

2.3.2 **Shrinkage brittleness theory** . . . 15

2.3.3 **Strain theory** . . . 15

2.3.4 **Generalised theory** . . . 15
2.3.5 **Modified generalised theory** . . . 16
2.3.6 **Technological strength theory** . . . 17
2.3.7 **Summary** . . . 17
2.4 **Factors that influence solidification cracking** . . . 18
2.4.1 **Metallurgical factors** . . . 18
2.4.2 **Thermo-mechanical factors** . . . 20
2.4.3 **Summary** . . . 22
2.5 **Weldability testing** . . . 22

3 Experimental and numerical methodology **27**

3.1 **Material selection** . . . 27
3.2 **Laser beam welding set-up** . . . 29
3.2.1 **Hot cracking tests at Tata Steel** . . . 29
3.2.2 **Laser beam welding set-up at Delft** . . . 30
3.3 **Analysis of the laser beam** . . . 31
3.4 **Microstructural characterisation** . . . 33
3.4.1 **Sample preparation** . . . 33
3.4.2 **Optical microscopy** . . . 33
3.4.3 **Scanning electron microscope** . . . 33
3.5 **Finite element modelling** . . . 34

4 Experimental evaluation of hot cracking susceptibility **39**

4.1 **Introduction** . . . 39
4.2 **Experimental results obtained using laser-1** . . . 40
4.2.1 **Crack length in DP-1 steel** . . . 40
4.2.2 **Crack length in DP-2 steel** . . . 42
4.2.3 **Crack length in TRIP steel** . . . 44

4.3 **Experimental results obtained using laser-2** . . . 46

4.3.1 **Crack length in DP-1 steel** . . . 46

4.3.2 **Crack lengths in DP-2 steel and TRIP steel** . . . 47

4.4 **Summary of the results** . . . 48

5 Experimental and numerical evaluation- weld pool shape and process efficiency 53

5.1 **Introduction** . . . 53

5.2 **Experimental setup** . . . 53

5.3 **Results** . . . 55

5.3.1 **Temperature cycle during laser beam welding of DP-1 steel and TRIP steel** . . . 55

5.3.2 **Weld Pool shape and mushy zone of DP-1 steel** . . . 58

5.3.3 **Weld Pool shape and mushy zone of TRIP steel** . . . 59

5.3.4 **Efficiency of the laser beam welding process** . . . 60

5.3.5 **Summary of the results** . . . 61

6 Discussion 65

6.1 **Variations in measured average crack lengths** . . . 65

6.2 **Effect of laser beam spot size and welding speed** . . . 67

6.3 **Effect of de-focusing manner** . . . 71

6.4 **Weld pool shape and process efficiency** . . . 72

6.5 **Metallurgical contribution to solidification cracking** . . . 74

7 Conclusions and scope for further research 77

7.1 **Conclusions** . . . 77

7.2 **Scope for future research** . . . 78

Glossary 79

Bibliography 81

ABSTRACT

Third-generation advanced high strength steels (AHSS) are a new class of steels that offer superior functional properties and significant weight savings in the body-in-white (BIW) structure of a car. Weight savings directly translate to reduced CO_2 emissions from cars which aids automotive manufactures to meet the vehicle emission guidelines put forth by regulatory bodies around the world. Further increase in weight savings and productivity can be realised when BIW components are fabricated using laser beam welding (LBW). However, the phenomenon of solidification cracking of AHSS during LBW poses challenges to not only its application in the automotive industry, but also in the production lines of steel manufacturers. From the body of literature pertaining to solidification cracking two fundamental conditions can be identified that result in solidification cracking in alloys. First is the development of thermo-mechanical stresses/strains during liquid melt solidification and second, is the formation of a crack susceptible microstructure. In addition to this, the welding conditions can influence the susceptibility of alloys to solidification cracking. The objective of the present study is to understand the influence of variable processing conditions during LBW on solidification cracking tendency of AHSS and how to control these conditions to minimise it. In particular, an attempt is made to understand the effect of keyhole configuration, welding speed and laser beam spot size on solidification cracking. Furthermore, finite element analysis is used to predict the size and shape of the weld pool during LBW, and to determine the net process efficiency which in turn is compared with the calculated process efficiency from the existing analytical model.

Bead-on-plate LBW following the testing procedure of the VDEh (German Steel Institute) standard hot cracking test was performed on three third-generation AHSS at two LBW facilities with different beam quality. Due to this, the keyhole during the tests at the two facilities was identified to exist in the closed keyhole configuration and more towards the open keyhole configuration. The susceptibility to solidification cracking was found to increase when the keyhole prevailed in the closed keyhole configuration during LBW. The keyhole configuration was varied by altering the process parameters (welding speed and spot size of the laser beam) in comparison to the parameters corresponding to the closed keyhole configuration. Reducing the welding speed, while keeping the laser power and spot size constant, resulted in the open keyhole configuration and subsequent reduction in the solidification cracking tendency but, until a limit. Similarly, reducing the spot size, while keeping the welding speed and laser power constant, also reduced the solidification cracking tendency as the open keyhole configuration was enforced. The macroscopic area of the fusion zone (weld size) was found to corroborate with the solidification cracking tendency of the alloys. Consequently, the spot size of the laser beam was varied to determine the critical spot size which resulted in a critical weld size at which solidification cracking did not occur. Corresponding to this, the critical process efficiency was determined which is representative of the critical heat input above which solidification cracking occurs. However, the magnitude of the critical spot size, weld size and process efficiency is dependent on the solidification cracking susceptibility of the alloy in question.

ACKNOWLEDGEMENTS

I'd like to take this opportunity to thank everyone who has helped me in this journey, and specifically over the course of my M.Sc thesis. In view of the ongoing COVID-19 pandemic their immense contribution in providing safe working conditions cannot be overlooked.

Firstly, I would like to thank the faculty of Materials Science and Engineering, Delft University of Technology for providing students with a vibrant environment conducive to learning. I'd like to express my sincere gratitude to my supervisors, dr. Marcel Hermans, and dr. Gautam Agarwal for their valuable guidance and discussions during this thesis. I thank Jurriaan van Slingerland for his technical input on laser beam welding and helping me get comfortable with the new 8 kW laser. A special thanks to my friends in Delft for making regular evenings memorable.

My parents and brother have been a source of constant emotional support and encouragement during this journey. There is no dictionary that can provide me with words to express how thankful I am for having you. I will always be indebted to my girlfriend, Sharon, for her companionship and unending support. Finally, I am grateful to God for blessing me with the means to have an education.

Arjun Sood
Delft, June 2020

LIST OF FIGURES

1.1 Materials used in Audi A4 structure 2

1.2 Global CO_2 concentration 2

2.1 LBW modes 6

2.2 Keyhole modes in LBW 7

2.3 Laser spot size adjustment 8

2.4 Zones in a fusion weld 9

2.5 Weld pool shape 9

2.6 Properties and generations of AHSS 10

2.7 Properties of second generation steels 11

2.8 DP steel processing 12

2.9 TRIP steel processing 12

2.10 Crack in a DP steel 13

2.11 Factors influencing hot cracking 14

2.12 Crack surface in DP steel 14

2.13 Stages in shrinkage brittleness theory 15

2.14 Stages of generalised theory 16

2.15 Stages in modified generalised theory 16

2.16 The Brittle temperature range 17

2.17 Factors in solidification cracking 18

2.18 Brittle temperature range of plain carbon steels 19

2.19 Surface tension and grain boundary liquid 20

2.20 Ductility curve with CST 21

2.21 Interactions between factors during solidification 22

2.22 Weldability tests 23

2.23 Holdcroft test 23

2.24 Standard hot cracking test VDEh 24

2.25 Varestraint test 24

2.26 U-type test 25

3.1 Phase diagram DP-1 28

3.2 Phase diagram DP-2 28

3.3 Phase diagram TRIP 29

3.4 LBW experiments schematic 30

3.5 PRIMES beam analyser 31

3.6 Laser beam profile 32

3.7 Sensitivity analysis of the mesh 34

3.8 Thermo-physical properties of materials 35

3.9 Thermo-physical properties of materials 35

3.10 Intensity dependence on n 36

4.1 Top surface of weld 40

4.2 Crack length for DP-1 steel 40

4.3 Fracture surface of DP-1 steel 41

4.4 Cross section for DP-1 steel 41

4.5 Cross section with 0.2 mm spot diameter 42

4.6 Crack length for DP-2 steel 42

4.7 Fracture surface of DP-2 steel 43

4.8 Cross section for DP-2 steel 43

4.9 Cross section with 0.2 mm spot diameter 44

4.10 Crack length for TRIP steel 44

4.11 Fracture surface of TRIP steel . . . 45

4.12 Cross section for TRIP steel . . . 45

4.13 Cross section with 0.2 mm spot diameter for TRIP steel . . . 46

4.14 Crack length for DP-1 steel . . . 46

4.15 Cross section for DP 1 steel with laser 2 . . . 47

4.16 Crack length for DP 2 steel . . . 47

4.17 Cross section of DP-2 steel and TRIP steel with 0.6 mm spot diameter . . . 48

4.18 Summary of the results . . . 49

4.19 Average crack length vs. weld area . . . 50

4.20 Measured weld size of DP 1, DP 2 and TRIP steel . . . 50

4.21 cross section of DP-2 steel . . . 51

5.1 Experiment schematic . . . 54

5.2 Thermal cycle of DP-1 steel . . . 56

5.3 Thermal cycle of TRIP steel . . . 57

5.4 DP-1 steel weld pool shape . . . 58

5.5 TRIP steel weld pool shape . . . 59

5.6 TRIP steel weld pool shape . . . 60

5.7 TRIP steel critical weld pool shape . . . 60

5.8 Numerical and calculated process efficiency . . . 62

6.1 Micrograph of OK configuration . . . 66

6.2 Micrograph of CK configuration . . . 67

6.3 Measured weld size of DP-1 steel . . . 67

6.4 Micrograph of OK configuration . . . 68

6.5 Effect of spot size on crack length . . . 68

6.6 Measured weld size of DP 1 steel . . . 69

6.7 Effect of welding speed on crack length . . . 70

6.8 Measured weld size of TRIP steel 71

6.9 Measured weld size of DP-1 steel 71

6.10 Top surface of weld 73

6.11 Phosphorous map in TRIP steel 75

LIST OF TABLES

3.1 Material composition 28

3.2 Liquidus and solidification temperature range 29

3.3 Testing parameters 29

3.4 Testing parameters 30

3.5 Laser beam properties 32

3.6 Volume of elements 34

4.1 Average Crack length from tests at Delft 49

4.2 Average Crack length from tests at Delft 49

4.3 Average Crack length from tests at Tata Steel 49

5.1 Testing parameters 54

5.2 Thermocouple positions on DP-1 steel 54

5.3 Thermocouple positions on TRIP steel 54

5.4 Temperature gradient in DP-1 steel 55

5.5 Temperature gradients in TRIP steel 55

5.6 Weld pool size in DP-1 steel 59

5.7 Weld pool size in TRIP steel 60

5.8 Critical efficiency of alloys 61

5.9 Summary of weld pool properties in DP-1 steel 61

5.10 Summary of weld pool properties in TRIP steel 62

6.1 Critical efficiency of alloys 74

1

INTRODUCTION

1.1 INTRODUCTION

The steel industry has experienced tremendous growth over the last few decades [1]. Higher production rates, improved material properties and performance are direct results of this growth. Naturally, the automotive sector is at the forefront of utilising and promoting the growth to their benefit. The automotive industry accounts for almost 12% of the total world steel consumption and Fig. 1.1 shows the use of steel among other materials in the body-in-white (BIW) structure of a car [2]. Modern materials and advanced fabrication techniques has made it possible to increase the added product value in cars through incorporating features such as aesthetics, occupant safety, durability and dynamics. A deeper understanding of materials science has allowed for generation of complex microstructures resulting in thinner gauge steels with superior performance in terms of strength, ductility and toughness. Therefore, the demands and needs of automotive industry are a priority for steel manufacturers around the world.

At the core of automotive engineering lies a challenging task of maximising fuel efficiency. Automobiles with internal-combustion engines employ fuels derived from a finite supply of fossils, which release CO_2 as a by-product during the combustion stage. The adverse effects of CO_2 on the surrounding environment are witnessed through increasing ambient temperatures triggered by globally rising CO_2 levels, as shown in Fig. 1.2. Therefore, improving vehicle fuel efficiency is not only important from an engineering viewpoint but also from a socio-environmental standpoint. With the aim to tackle increasing CO_2 levels, regulatory bodies around the world have laid down strict directives to control carbon emissions from vehicles. The european union regulation on CO_2 emission sets the target to 95 g CO_2/km for 2021, to be phased in from 2020 [5]. A direct approach to tackle increasing emissions is to reduce vehicle weight; a 5.5% improvement in fuel economy can be achieved by a 10% reduction in weight [2]. To counter increasing vehicle emissions and considering the finite supply of fossil fuels, 35 steel producers from 18 different countries jointly conducted the Ultra-Light Steel Auto Body (ULSAB) project. The study concluded with a body structure weighing 25 % less compared to the existing benchmarked structure [4]. One of the key materials in the ULSAB project were Advanced High Strength Automotive Steels (AHSS) and from there on this new class of steels have been extensively incorporated in automobiles owing to their superior strength and formability [5]. In addition to

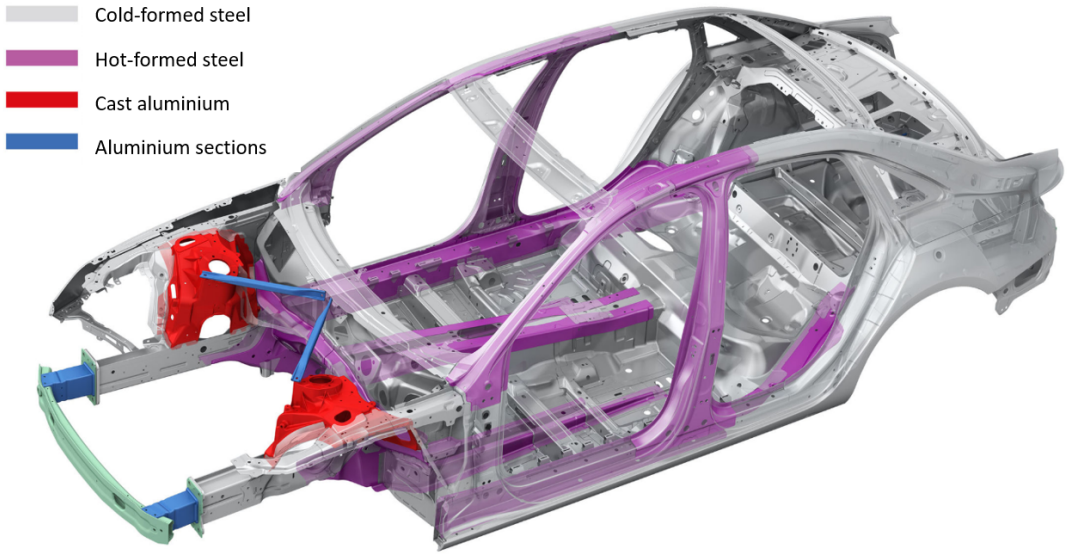

Figure 1.1: Materials used in Audi A4 body-in-white components [3]

the superior mechanical properties, weldability of the newly developed AHSS is also important. The ULSAB project had over 18 m of laser welded seams [6]. Furthermore, modern day BIW parts comprise of laser-welded blanks (LWBs) to maximise cost savings, weight reduction and part integration [7]. However, the weldability of certain AHSS is of concern as they are rendered susceptible to solidification cracking, owing to thermo-mechanical and metallurgical interactions during welding.

Solidification cracking is often reported by steel manufacturers (entry and exit coil joining in rolling mills) and automotive industry (fabrication of sheet metal components for body structure) using laser welding. Therefore, to minimise production downtimes and produce weldable steels it is important to develop a fundamental understanding of solidification cracking.

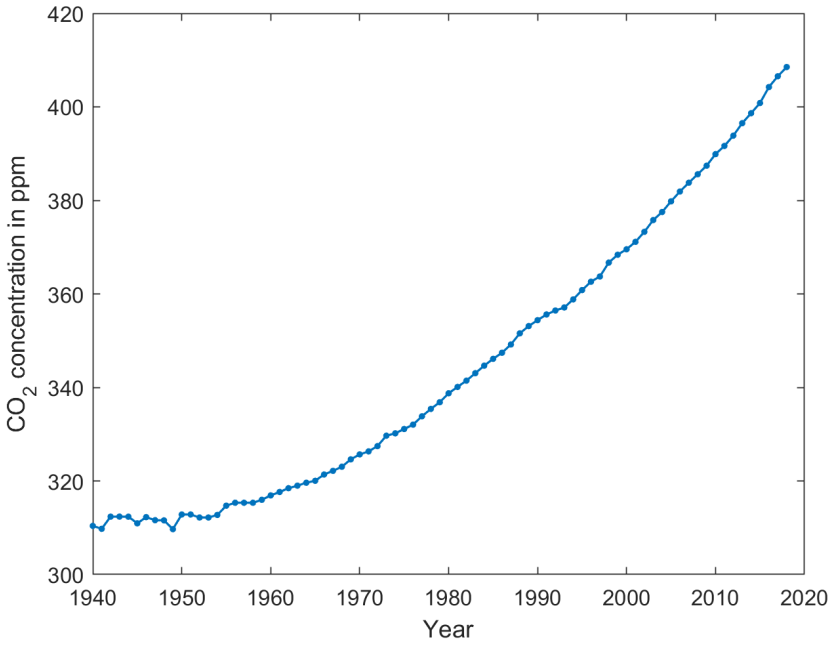

Figure 1.2: Atmospheric CO_2 levels corrected for seasonal variations [8].

1.2 RESEARCH GOALS

The application of certain AHSS to automobiles can sometimes be limited due to their low weldability. As mentioned earlier, solidification cracking is encountered during welding of AHSS if the right conditions for cracking persist. Based on literature, two fundamental conditions can be identified which are necessary for solidification cracking to occur. First, is the development of transient stresses/strains due to mechanical and thermal contraction/expansion of a material on welding, which can further be influenced by the externally imposed restraint through the use of fixtures/clamps. Second, is the formation of a crack susceptible microstructure. The above two conditions are generally referred to as the thermo-mechanical and metallurgical factors, respectively. In addition to these factors, during full penetration laser welding of steel sheets process related conditions (laser spot size, heat input and keyhole configuration) can influence the solidification cracking tendency of materials.
In the present study, three AHSS are analysed using experimental and numerical tools. Of the three AHSS, two are dual-phase steels (DP steel) and one is a transformation-induced plasticity steel (TRIP steel). The materials are ranked for their solidification cracking tendency using the VDEh (German Steel Institute) standard hot cracking test for thin steel sheets during laser welding. Tests are conducted for various processing conditions (welding speed, spot size and multiple laser beam welding facilities) to understand its influence on cracking. An attempt is made to identify the factors that promote cracking. Microstructural features were analysed to gain insight on the identified factors. To further build upon the understanding of process related factors a finite element heat transfer model was utilised to calculate the net process efficiency of bead-on-plate laser welding. The possibility to avoid cracking or improve the weldability of steels by adjusting the process parameters was also explored.

The main objectives of this study are:

"*Understanding the influence of processing conditions on solidification cracking*"
-Laser beam spot size
-Laser beam characteristics
-Welding speed
-Laser beam de-focusing manner

"*Developing a set of safe process parameters to improve the weldability of AHSS*"

1.3 OUTLINE OF THE REPORT

In Chapter 2, the requisite theoretical background of laser beam welding (LBW), AHSS, solidification cracking and weldability testing is provided. A description of the experimental setup, process parameters, characterisation tools and modelling approach is given in Chapter 3. In Chapter 4, results of the VDEh standard hot cracking tests for the three alloys used in this study and corresponding microstructural evaluation using characterisation tools are described. In Chapter 5, the numerically and analytically calculated process efficiency for bead-on-late laser welding is presented. In Chapter 6, the results obtained from the study are discussed. Finally, in Chapter 7 the report is concluded with recommendations for future work.

2

THEORETICAL BACKGROUND

This chapter deals with the requisite theoretical background needed to gain a more comprehensive understanding of the contents of this study. An introduction to the laser welding process and the corresponding microstructural features of a weld joint is provided followed by an overview of AHSS with a description of the steels used in the present study. Finally, the phenomenon of solidification cracking and the factors contributing to it are discussed.

2.1 LASER BEAM WELDING

Laser beam welding is a joining technique that utilises a laser to generate a highly collimated, coherent and monochromatic light beam. Using an optical system, the resulting light beam can be focused to a tiny spot (typically 0.2-0.6 mm in diameter) which is used to create a weld joint. Commonly used industrial lasers can be classified as solid-state or gas lasers. CO_2 laser is an example of a classic gas laser that generates a light beam with an infrared wavelength of 10.6 µm. Whereas, Nd:YAG- disk and Yb:YAG- disk are examples of solid-state lasers that operate at wavelengths of 1.030-1.064 µm [9][10]. The laser beam absorption by a material depends on the wavelength of the beam which is derived from the active material in the laser. Therefore an array of materials can be processed using LBW.

Due to multiple advantages of LBW, it is becoming increasingly popular in the automotive industry. In recent years the advent of weldable AHSS, has made it possible to achieve significant reductions in vehicle weight thereby limiting CO_2 emissions. Thinner gauge sheet metal parts can be produced with superior mechanical properties and increasing weight savings. Extensive use of laser beam welding for producing tailor welded blanks, body-in-white applications and gear components is recognised by the automobile industry [11]. High production rates due to higher welding speeds, large degree of process automation, low heat application to the workpiece and small heat-affected zone are a few of the many merits offered by laser beam welding over more conventional arc welding methods [9][12][13].

Furthermore, the process is gaining precedence over more commonly used resistance spot welding as a recent study conducted by Klinger showed a weight saving of 12.2 kg in BIW by switching from a spot welded

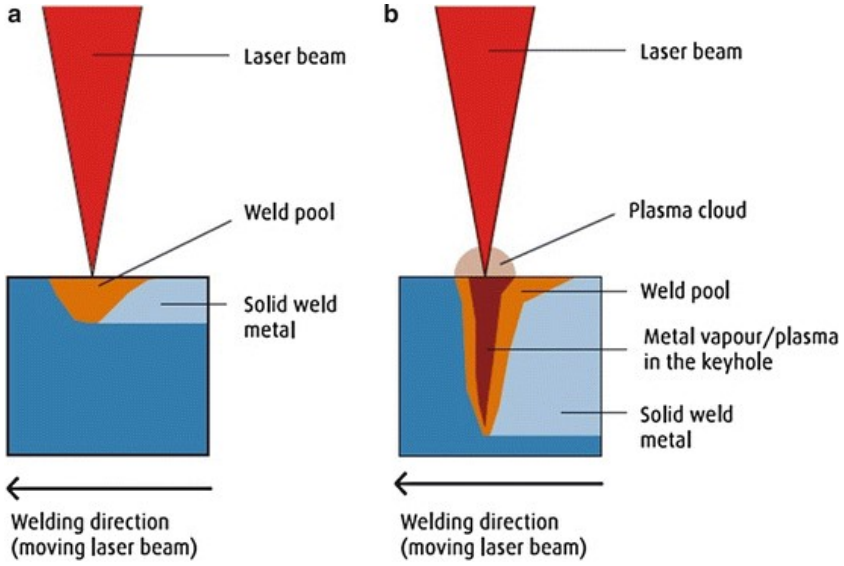

Figure 2.1: A schematic of the common operational modes of laser beam welding (a), conduction mode and (b), keyhole mode [12].

structure to a laser welded structure [13]. Therefore, laser beam welding is an interesting joining technique for automotive manufacturers around the world.

2.1.1 LASER BEAM WELDING OPERATION MODES

Laser beam welding can be performed in two fundamentally distinct modes, namely, conduction mode and keyhole mode. Fig. 2.1 provides a schematic overview of the two modes. The two modes are briefly described below.

Conduction mode- In conduction mode, the power density is low- typically below 10^5 W·cm^{-2} [9][12]. Only part of the laser beam is absorbed at the surface and the rest reflected (via direct Fresnel absorption/reflection). The absorbed beam is utilised to melt the material, resulting in a weld. The welds formed in conduction mode have a high width to depth ratio [14].

Keyhole mode- During keyhole mode laser welding the power density is in the order of 10^6 W·cm^{-2} or even larger [13]. The larger power density not only melts the material, but also vaporises it and results in the formation of a cavity, so-called keyhole. The metal vapour filled cavity further refracts the laser beam passing through it and causes multiple reflections of the laser beam at the keyhole walls. Therefore, the energy absorption in the case of keyhole mode is larger which results in deep narrow welds with a high depth to width ratio [14]. Welding in keyhole mode requires a certain minimum power level to be met (high power density for keyhole formation). Factors such as welding speed, material composition, plate thickness, focal plane position, beam profile and shielding conditions influence the minimum power level for the onset of keyhole mode welding.

Other phenomena that occur during full penetration keyhole mode welding is the formation of either an open keyhole (OK) or a closed keyhole (CK) configuration [15][16]. Fig. 2.2 illustrates both phenomena schematically. During laser welding of thin steel sheets in keyhole mode an open keyhole (OK) configuration exists when the keyhole is open at both top and bottom surface of the workpiece. As shown in Fig. 2.2 a, the openings act as escape routes (from reflection/scattering within the keyhole) for the incident laser beam. Welding in OK configuration during keyhole mode is possible until a certain maximum power level while keeping the welding speed and spot size constant. Any further increase in the power (maintaining other factors constant)

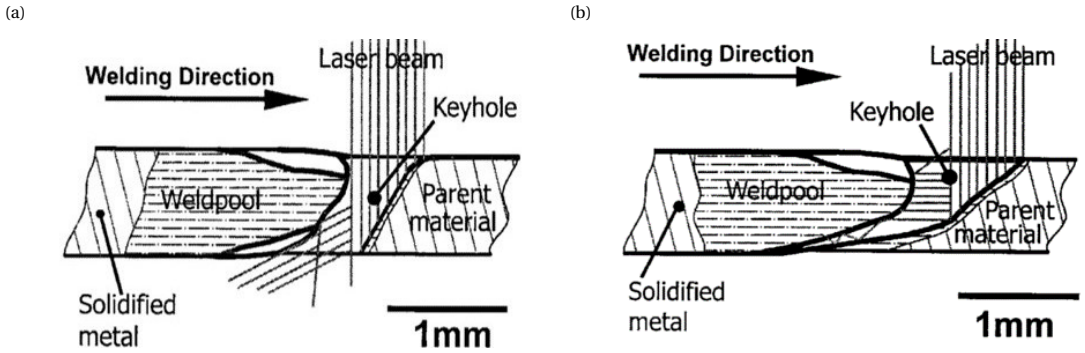

Figure 2.2: Keyhole configurations during LBW (a), OK configuration and (b),CK configuration [15].

enforces a cutting action rather than welding. Whereas, in a closed keyhole (CK) configuration, the keyhole is open only at the top surface of the workpiece. Therefore, the incident laser beam can only escape from the top surface as the molten metal at the root closes the keyhole and acts as a barrier for the beam to escape from the bottom as shown in Fig. 2.2 b. Welding in CK configuration is only possible in a narrow range of process parameters (laser power and welding speed). Also, CK configuration is sensitive to fluctuations of the incident power and external mechanical vibrations that tend to shift the welding configuration while welding in CK configuration to either OK configuration or partial penetration welding. A simple way to identify whether a weld is made in an OK or CK configuration is by visual inspection of the welded workpiece. Opening of the keyhole on the bottom surface of the workpiece allows for the vaporised metal from the keyhole to escape. As the vapor is warmer than the surrounding air it rises and condenses on the bottom surface of workpiece. The condensed gas leaves a dark residue on the bottom surface of the sheet when welded in OK configuration, which is not observed in welds made in CK configuration.
Additionally, the extra opening in an OK configuration translates to increased energy losses from the workpiece, thereby dropping the efficiency of the process when compared to welding in a CK configuration. Therefore, the resulting size and shape of the weld can differ significantly for the two welding configurations.

2.1.2 LASER BEAM SPOT SIZE ADJUSTMENT

An industrial laser welding machine consists of high precision optics (collimator lens and an objective lens) that can focus the laser beam to an extremely small diameter spot, for example, 0.2 mm. Fig.2.3 illustrates one of the two ways in which the focused spot position can be adjusted to suit the needs of a user by adjusting the distance between an assembly of a collimator and an objective lens.
In Fig. 2.3 b, the collimator lens generates a nearly perfect parallel laser beam which is incident on the objective lens resulting in the smallest possible spot size of the laser beam on the top surface of the workpiece. Or, in other words, the focal plane of the objective lens coincides with the top surface of the workpiece. When the collimator lens is moved downwards, positive direction in Fig. 2.3 b, the beam incident on the objective lens becomes convergent. As a result, the objective lens generates a focused laser beam spot above the workpiece surface as shown in Fig. 2.3 a. In the other case, by moving the collimator lens upwards, negative direction in Fig. 2.3 b, causes a divergent beam to be incident on the objective lens which, generates a focused spot below the workpiece as shown in Fig. 2.3 c. Another possibility exists for users with a laser assembly mounted on a 3-axis servo-controlled positioning system. Using the positioning system the entire optical assembly or the laser head marked as 3 in Fig. 2.3 b can be moved in either direction. This results in the placement of the focused spot at different positions with regards to the workpiece in a similar manner as described previously.

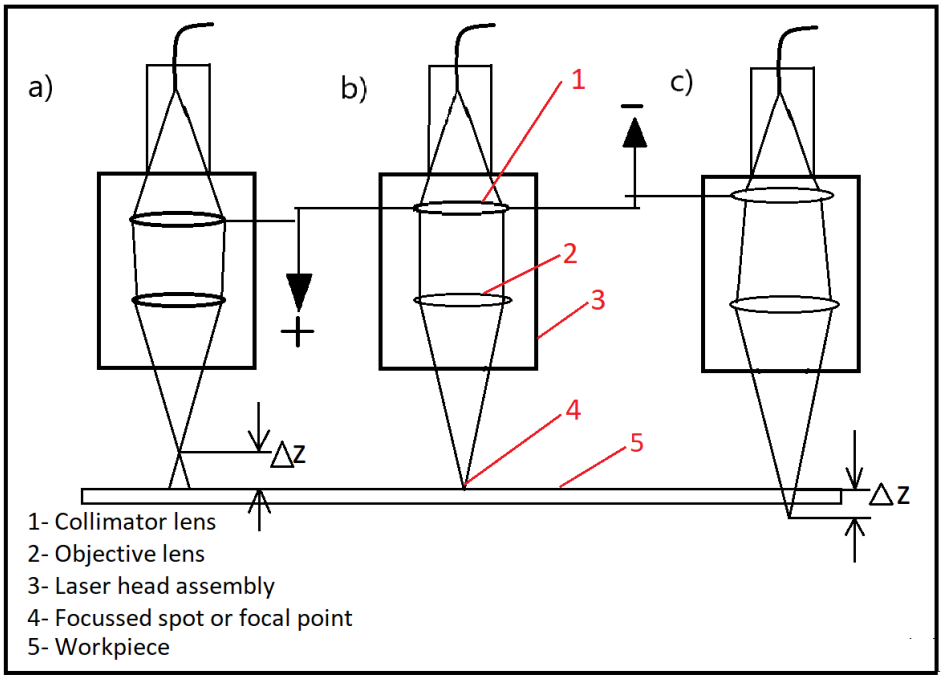

Figure 2.3: A schematic demonstrating laser beam focusing in (a), above the workpiece surface (b), on the workpiece surface (focus spot of laser beam) and c) below the workpiece. Switching between the three possibilities by varying the distance between the collimator lens (1) and the objective lens (2) or by moving the laser head (3).

The difference between the two lies in the movement of the collimator lens for the former and the vertical movement of the entire laser head for the latter.

2.1.3 FEATURES OF THE WELDMENT

Weld zones- A weld can be characterised into three distinct regions: fusion zone (FZ), heat-affected zone (HAZ) and the unaffected base metal (BM) [17]. The FZ experiences complete melting and solidification, whereas HAZ and BM are the parts of the weld where no melting occurs. Additionally, in alloys a partially melted zone (PMZ) also exists between HAZ and FZ. The FZ experiences the highest temperature owing to complete melting, followed by HAZ and BM, respectively. As heat is conducted away from the FZ and into the material, a HAZ develops whose extent depends on the material composition and thermodynamics. Further conduction of heat from HAZ into the material results in a temperature field which is not significant to cause any microstructural changes and forms the BM whose microstructure is identical to the material prior to welding. The above mentioned weld zones are shown in a schematic manner in Fig. 2.4.
Weld pool shape- Factors pertaining to the process (laser power, welding speed, voltage and current (in arc welding)) and material (physical properties, composition) determine the shape and size of the weld pool. Generally, teardrop and elliptical shape of a weld pool are observed during welding as shown in Fig. 2.5 [19]. Materials with high thermal conductivity and welding at lower speed favour the formation of an elliptical weld pool. In an elliptical weld pool, the direction of the maximum thermal gradient (G_L in Fig. 2.5) changes continuously over the trailing edge of the weld pool or the rear solid-liquid interface. Due to the continuously changing direction, grains start to solidify from the fusion lines and bend towards the trailing edge of the weld pool (in the direction of maximum thermal gradient) as shown in Fig. 2.5 a. When welding at higher speeds, a teardrop shaped weld pool forms as shown in Fig. 2.5 b. In this case, the direction of the maximum

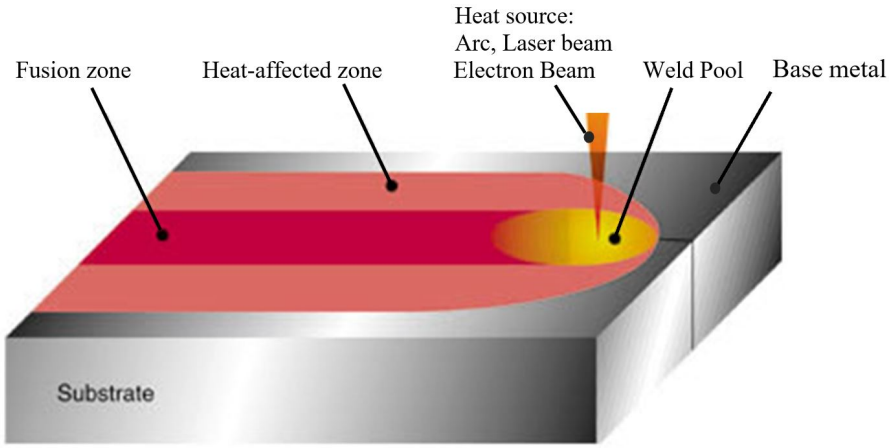

Figure 2.4: Schematic of the zones that develop as a result of fusion welding [18].

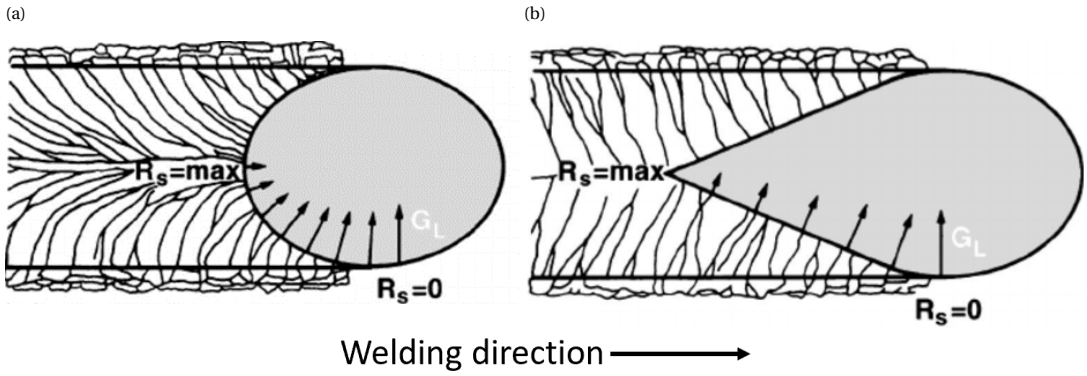

Figure 2.5: A schematic diagram showing commonly observed weld pool shapes during welding (a), elliptical pool and (b) teardrop pool [20].

thermal gradient does not change and remains nearly perpendicular to the trailing edge of the weld pool. Therefore, grains developing in a teardrop weld pool tend to grow straight from the fusion lines towards the rear solid-liquid interface and impinging at the weld centre-line.

2.2 ADVANCED HIGH STRENGTH STEELS

Dual-Phase (DP steels), Transformation Induced Plasticity (TRIP steels), Complex Phase (CP steels) and Martensitic (MART steels) steels form the pool of AHSS [21]. The standard naming practice for AHSS follows, XX aaa/bbb notation, where, XX states the type of steel, aaa is minimum yield strength and bbb is minimum tensile strength, both in MPa [21]. Typical yield strength and tensile strength for AHSS lie upwards of 300 and 550-600 MPa, respectively [21][22] . Superior properties of AHSS validate their use in automotive components which are a result of complex multi-phase microstuctures obtained through carefully controlled metallurgy [23]. The general classification of AHSS is shown in Fig. 2.6. Three distinct classes can be identified, namely-

1. First generation AHSS
2. Second generation AHSS
3. Third Generation AHSS.

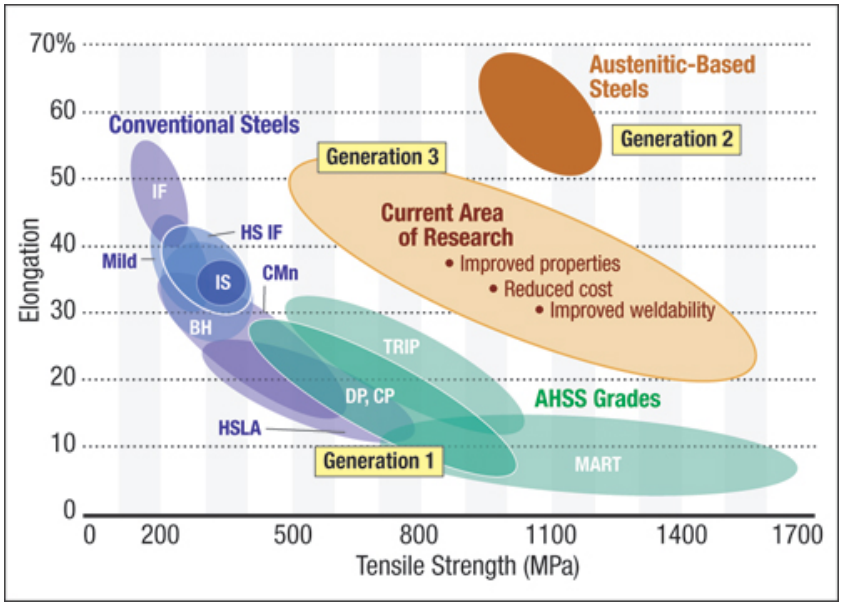

Figure 2.6: Schematic of different steel grades in an elongation vs. tensile strength map [24].

2.2.1 FIRST GENERATION AHSS

First generation AHSS comprises of DP, TRIP, MART and CP steels. TS-E1 product (tensile strength-per cent elongation) for this category falls under 25,000 MPa % [25]. Microstructure comprises of a ferrite-based matrix along with a second phase (martensite, retained austenite, bainite). Mechanical properties are derived from the constituent phase distribution, volume fraction, composition and grain size [21][22]. This class of steels provide higher strength than conventional steels. DP steels contain martensite (hard phase) within the ferrite (soft phase) based matrix. The amount of martensite determines the strength of the final product. Typical tensile strength range varies from 450-1200 MPa depending on the microstructure [26]. The volume fraction of martensite can range from 5-50 %, with a possibility of 100% martensite as well [27]. In the latter case, martensitic islands are lined with the soft ferrite phase [27]. Multiple advantages offered by DP steels justifies its use in automobiles. Higher strengths can be achieved by controlling the microstructure and with bake hardening during the paint baking step. DP steels offer good weldability, provided carbon contents are low [25]. DP steels also happen to be the most used steels in automotives from the pool of AHSS [26].

2.2.2 SECOND GENERATION AHSS

Twinning induced plasticity (TWIP), lightweight induced plasticity (L-IP) and shear band induced plasticity (SIP) constitute second-generation AHSS [28]. This class of steel has a TS-E1 product over 50,000 MPa % and is also referred to as Ultra AHSS [22][25]. As shown in Fig. 2.6, these steels are austenitic- gamma phase in iron which is stable at high temperatures (above 720 °C). An ample amount of alloying elements (Ni, Mn, Co) are used to stabilise austenite at room temperature in these steels and addition of such elements comes at an expense. Thus, rendering the second generation of AHSS as relatively expensive but, with a superior strength and ductility combination when compared to first-generation AHSS, as shown in Fig. 2.7. However, the additional costs and processing difficulties have pushed researchers to explore newer possibilities, resulting in the third-generation of AHSS [25][28].

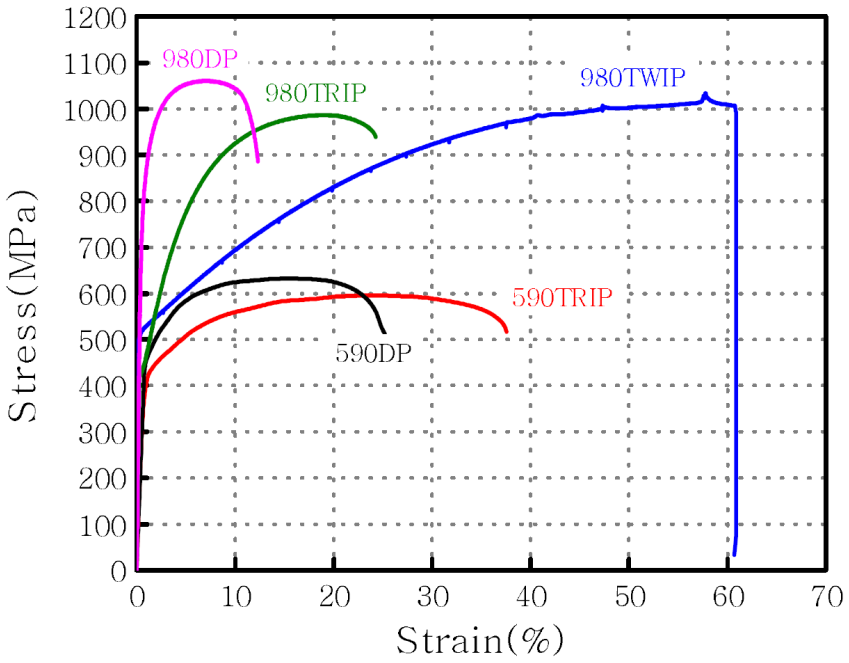

Figure 2.7: tensile curve of 980TWIP compared to first generation AHSS [25].

2.2.3 THIRD GENERATION AHSS

To produce cost-effective steels with superior formability, third-generation or Extra AHSS are being tested and developed for commercial use. The idea is to enhance the properties of first- generation AHSS and generate desired microstructure (ultra-fine ferrite, retained austenite, carbide free bainite, martensite) by utilizing Q&P technique, TRIP, TWIP effect and micro-alloying [28] [29] . The TS-E1 product for this class of materials is intermediate to that of first and second-generation AHSS. Use of alternative processing techniques, grain refinement and multi-phase microstructure allows for developing third-generation AHSS with significantly better properties than first-generation AHSS while keeping them economically cost-effective by maintaining lean compositions when compared to second-generation AHSS [28]. Three types of third-generation AHSSs are used in the present study, two are DP steels and one is a TRIP steel, which are briefly described below.

DP Steel- As explained in section 2.2.1, DP steels comprise of a soft ferrite matrix with a distribution of secondary phase martensitic islands. The processing technique employs heat treatment cycle to obtain the dual phase microstructure as shown in 2.8. The first step of the heat treatment cycle involves heating the material to reach a temperature within the intercritical region (between Ac_1 and Ac_3 temperature) where a ferrite-austenite structure prevails. During the annealing step austenite is enriched with carbon as a result of carbon diffusion. Annealing is followed by quenching to a temperature below the martensite start where the material is held isothermally for the transformation of austenite to martensite. Finally, cooling to room temperature to obtain the dual-phase ferrite-martensite microstructure. Owing to their superior mechanical properties (toughness and fatigue strength) and formability, cold rolled DP steels are vastly used for producing automotive components. [30][31].

TRIP steel- TRIP steels have a high energy absorption capacity, good drawability and formability which makes

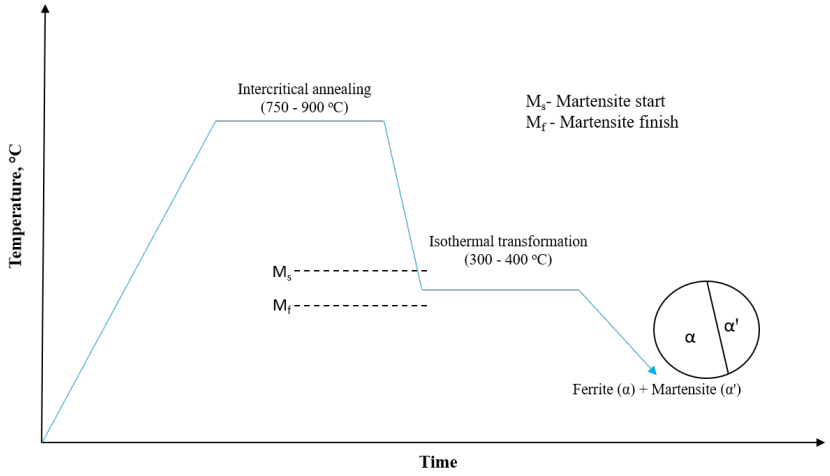

Figure 2.8: A schematic of the heat treatment cycle for DP steel [17].

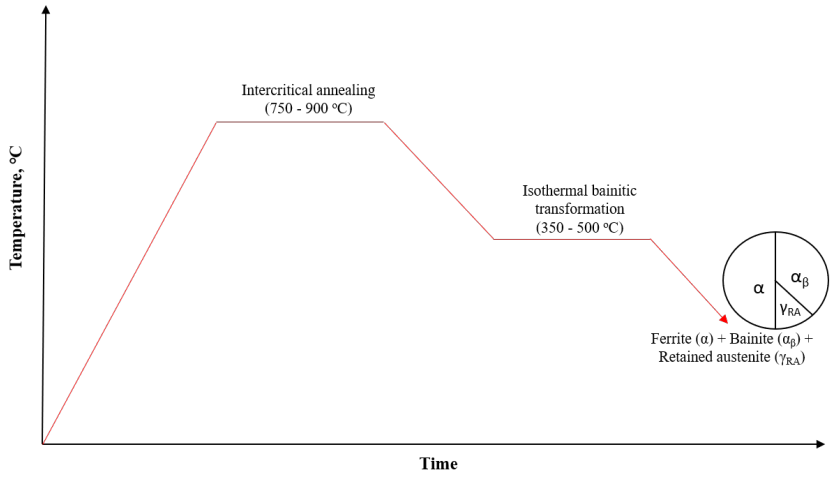

Figure 2.9: A schematic of the heat treatment cycle for TRIP steel [17].

them suitable for automobile applications. The TRIP effect was first observed by Schielin in 1930s and later in 1980s, Matsumura *et al.* were able to demonstrate the TRIP effect in low alloy steels comprising of 0.2–0.4 wt. % C, 1–2 wt. % Mn, and 1–2 wt. % S [32]. Since then the TRIP phenomena has remained a topic of interest for both researchers and industry. The subsequent understanding of the microstructural evolution of TRIP steels using modern processing techniques has made it possible to produce alloys with lean compositions thereby making the production and use financially feasible. The multi-phase microstructure is obtained through a carefully controlled heat treatment cycle as shown in Fig. 2.9. The first step of the heat treatment cycle is analogous to the one followed for DP steel. Thereafter, intercritical annealing is followed by fast cooling to an intermediate temperature (above the M_s temperature) which is maintained for bainite formation. This step is known as isothermal bainitic formation. Formation of other phases like pearlite and cementite is inhibited by addition of alloying elements like Al, P and S. The final microstructure comprises of ferrite, retained austenite-through addition of austenite stabilisers like Mn and a fast cooling rate, bainite and a possibility of some amount of martensite. The TRIP effect is primarily obtained from transformation of retained austenite to martensite during loading.

2.3 INTRODUCTION TO SOLIDIFICATION CRACKING

Solidification cracking refers to the phenomenon of formation of an irreparable defect in solidifying metal alloys [33][34]. Weld-centreline cracking, hot cracking and hot tearing are all synonyms to solidification cracking. Welding, just like the age-old practice of casting, involves solidification of liquid metal, during which hot cracks may form if appropriate conditions for cracking persist [35][36]. Solidification cracking occurs in the fusion zone of the weld, as shown in Fig. 2.10. Whereas, other forms of welding associated cracking- liquation and lamellar cracking, occur in the PMZ and HAZ of the weld respectively [37][38].

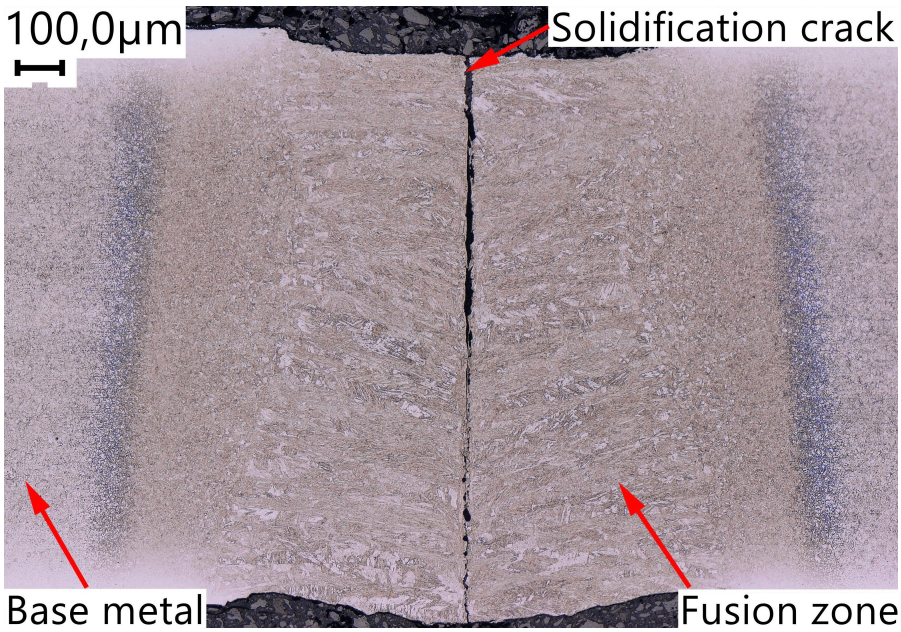

Figure 2.10: Cross section of bead-on-plate laser welded DP steel showing the weld-centreline solidification crack (perpendicular to welding direction).

Solidification of alloys proceed with the formation of a two phase solid-liquid mixture before completely transforming into solid. The dual phase mixture can be referred to as the mushy zone. As temperature decreases a solid network develops rapidly and close to the solidus temperature when little liquid remains an extensive solid network exists. At this stage, the remaining liquid can be present in the form of intergranular films. Because of negative volume change on solidification and non-uniform thermal contraction/expansion, a complex stress state develops in and around the mushy zone. Solidification cracking during welding occurs if the thermal cycle imposed stress/strains are high enough to cause rupture of intergranular liquid films in the mushy zone resulting in the formation of a solidification crack. Inspection of fracture surface of solidification cracks reveals their dendritic (egg-crate structure) appearance, which indicates that the cracks form in the mushy zone during terminal stages of solidification as shown in Fig. 2.12 [39].
Fundamental factors that influence solidification cracking can mainly be grouped under thermo-mechanical and metallurgical factors. Thermo-mechanical factors determine the resulting thermal/mechanical loads and metallurgical factors control the solidifying microstructure. In addition to this, full penetration LBW of steel proceeds in keyhole mode and process related conditions determine the keyhole behaviour. The thermal cycle imposed thermo-mechanical and metallurgical interactions along with process related conditions impact the solidification cracking susceptibility of a material. To summarize, it is in the mushy zone where

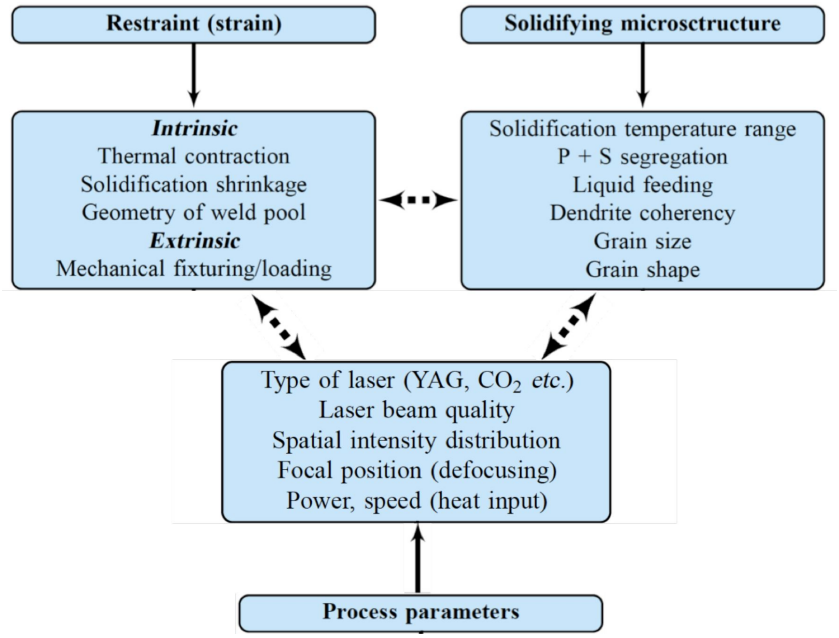

Figure 2.11: Fundamental conditions contributing to weld solidification cracking.

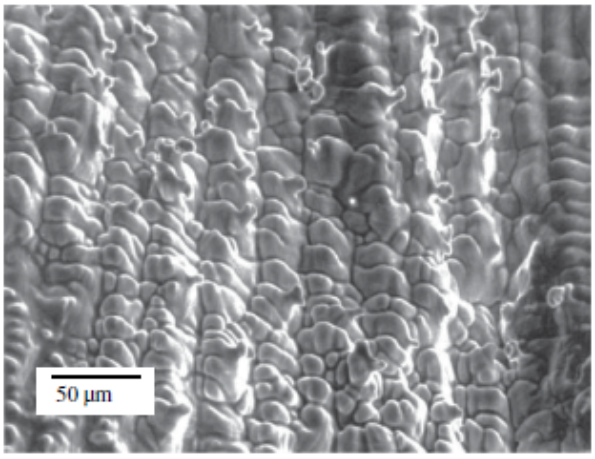

Figure 2.12: Scanning electron micrograph of the solidification crack surface in a DP steel [39].

an alloy is most susceptible to solidification cracking under the influence of a complex interaction between different factors as pointed out in Fig. 2.11. A number of these highlighted factors and relevant hot cracking theories are discussed in the proceeding sections.

2.3.1 THEORIES ON SOLIDIFICATION CRACKING

Hot cracking in castings is a well-studied subject providing a library of relevant literature from the past five decades. To elucidate the mechanisms of hot cracking in casting multiple theories have been proposed. Metal casting involves solidification of metals and their alloys in a constrained environment, similar to welding where, a solidifying melt pool is constrained by the surrounding cold material. Hence, theories applied to understand hot cracking in castings are also extended for gaining insight on solidification cracking during welding. Various theories are briefly discussed below.

2.3.2 SHRINKAGE BRITTLENESS THEORY

Works of Pumphrey *et al.* [40] and Bochvar [41] formulated the ideas for Shrinkage-Brittleness theory. This theory relates the development of strains on cooling to crack formation. Within the solidification range of the alloy an effective interval, below the coherency temperature, is identified where solid-solid interactions occur. Hence, according to the theory, cracks form within the effective interval, as shown in Fig. 2.13, due to strain build-up during solidification (solidification shrinkage, thermal contraction and/or external clamping).

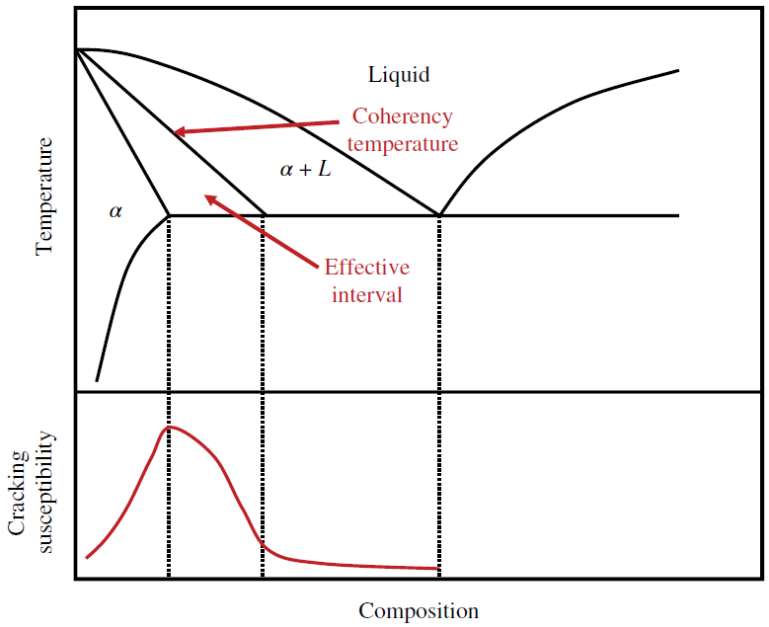

Figure 2.13: Schematic presentation of the shrinkage-brittleness theory using a eutectic phase diagram [39].

2.3.3 STRAIN THEORY

The strain theory was proposed by Pellini [42] in the 1950s. On cooling, the solid fraction increases, and if wetting is good the remaining liquid can persist in the form of continuous liquid films (intergranular films) around the solidified grains [43]. These liquid films can exist well below the equilibrium solidus temperature because of segregation. As solidification proceeds, strain accumulates in the liquid film boundaries and according to the strain theory, cracking occurs if the accumulated strain exceeds the ductility of the boundary [39].

2.3.4 GENERALISED THEORY

In 1960, Borland [44] proposed the generalised theory, which, splits the solidification range into different stages. Four stages can be identified as shown in Fig. 2.14. In stage 1, any applied stress is countered by the free movement of the solid and liquid phase. Stage 2, experiences the formation of a coherent solid network, allowing only the liquid phase to move. Stage 3, is identified by Borland as the critical solidification range due to the formation of an extensive solid network. Cracking in stage 3 is either caused by the surrounding solidified network hindering the melt flow or the limited availability of liquid to heal newly formed cracks [39][45]. At last, stage 4 does not experience any cracking because solidification is complete. Borland also

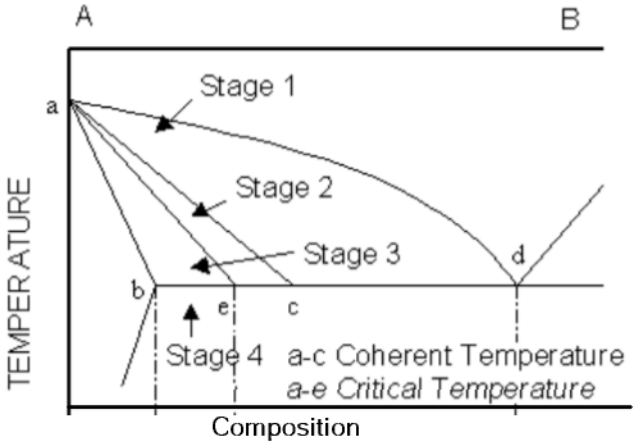

Figure 2.14: A schematic illustrating solidification stages according to the generalised theory [45].

emphasises on how liquid film wetting influences susceptibility to cracking: formation of continuous grain boundary liquid films when wetting is good can lead to cracking when the accumulated strain exceeds the strength of the liquid boundaries in stage 3.

2.3.5 MODIFIED GENERALISED THEORY

Based on dynamic observation of solidification cracking under an optical microscope, Matsuda et al. modified Borland's theory and developed the modified generalised theory [46]. Stage 3 of the generalised theory is split into a film stage and droplet stage, indicated as stage 3H and 3L in Fig. 2.15, respectively. Additionally, the extent of stage 1 as suggested by Borland was shortened to a smaller temperature range. A distinction between crack initiation and propagation is also made as the modified theory suggests crack initiation only in film stage-3H, whereas, propagation is possible in both stages [39][45][47].

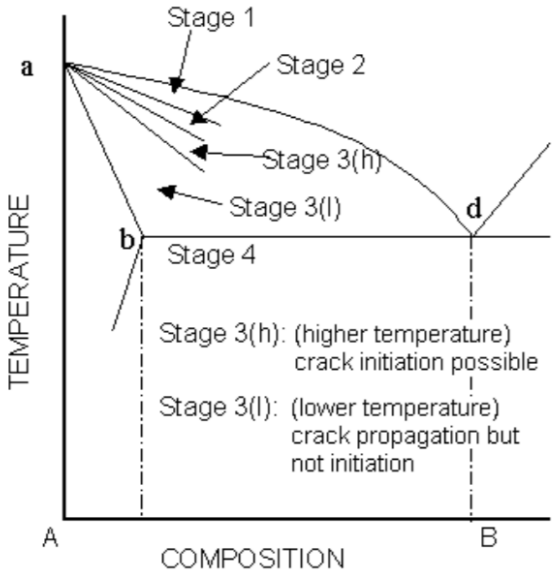

Figure 2.15: A schematic of the solidification stages as identified by the modified generalised theory based on direct experimental observation of solidification during welding.

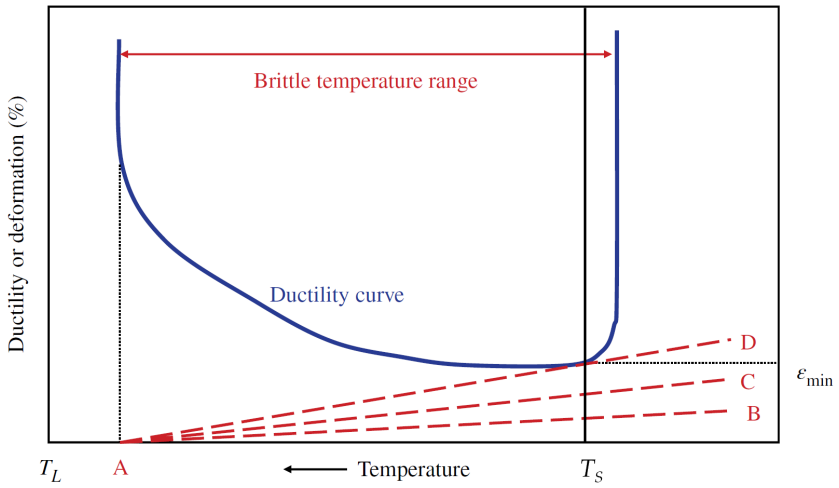

Figure 2.16: A schematic of critical strain in BTR according to technological strength theory [39].

2.3.6 TECHNOLOGICAL STRENGTH THEORY

In 1960s, Prokhorov [48] put forth the technological strength theory. Prokhorov considers a Brittle Temperature Range (BTR) over which an alloy experiences a loss in ductility. Solidification of the liquid melt after welding leads to the formation of thermally and/or mechanically induced strains. Outside the BTR the alloy has sufficient ductility to respond to these strains. According to this theory, solidification cracking will occur if the total accumulated strain on cooling exhausts the ductility of the material in the BTR [39][47][48]. The schematic ductility curve, as shown in Fig. 2.16, illustrates the loss of ductility in a material within the (BTR), line A-D defines the critical amount of strain, a higher deformation than that of line A-D (line with a larger slope than A-D) will result in cracking.

2.3.7 SUMMARY

The above-mentioned theories provide a basis to help understand and elaborate factors that can play a role in solidification cracking. Shrinkage brittleness theory and strain theory, considers accumulation of strain during solidification in the effective interval and at the liquid boundaries, respectively, to be the cause of cracking. Borland's generalised theory holds the developing stresses during melt solidification responsible for cracking in stage 3. The technological strength theory emphasises on a critical amount of accumulated strain to exceed the ductility limit for the onset of cracking. From these theories two conditions critical for cracking can be derived. First, is the presence of liquid films (continuous boundary films) along solidifying grain boundaries. Second, is the accumulation of strains or stresses at these boundaries which facilitate in rupture of liquid films eventually leading to cracking. The importance of these conditions is realised when solidification cracking can sometimes be avoided by adjusting the alloy composition to control the amount and morphology of the solidifying liquid during welding [37][39][49]. On the other hand, from the perspective of solidification cracking not all theories are entirely true. For example, cracking in the generalised theory is a result of solid-solid separation in stage 3, but observations of fracture surfaces of solidification cracks reveals a dendritic structure as shown in Fig. 2.12, suggesting that cracking is more likely a solid-liquid separation. Nevertheless, the concepts of liquid feeding, brittle temperature range, liquid film characteristics and ductility curves, critical to understand and evaluate solidification cracking in alloys, can be deduced from the existing theories. The thermal cycle during welding and the degree of external restraint imposes a complex

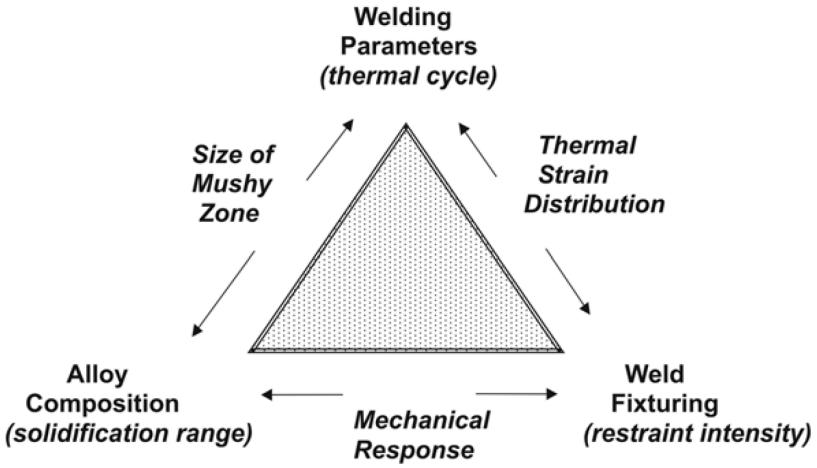

Figure 2.17: Multi-faced interaction between factors leading to weld solidification cracking [52].

stress state on the material. The material may or may not crack under the influence of these stresses/strains depending on its solidifying microstructure, which is derived from its metallurgy. Therefore, solidification cracking can be understood to arise from a mutli-faced interaction between a variety of factors as shown in Fig. 2.17 [50][51]. Possible factors influencing weld solidification cracking are discussed in the next section.

2.4 FACTORS THAT INFLUENCE SOLIDIFICATION CRACKING

Solidification cracking occurs as a result of various factors that control the solidification behaviour and the extent of local forces in the liquid melt. These factors result in a build up of local stresses/strains and evolution of a crack susceptible microstructure, and are termed as thermo-mechanical and metallurgical factors, respectively [36][39][52]. Thermo-mechanical factors can be external (caused by clamping) and internal (solidification shrinkage and thermal contraction) whereas, metallurgical factors control the structure and morphology of the solidifying grains. Eventually, the interaction between thermo-mechanical, metallurgical factors and processing conditions determine the susceptibility of a material to cracking.

2.4.1 METALLURGICAL FACTORS

Solidification temperature range- The temperature range during solidification of an alloy over which solid and liquid phases co-exist is referred to as the solidification temperature range of an alloy [52]. During non-equilibrium solidification, the solidifying liquid can be enriched with solute elements rejected from the solid phase which causes a drop in local solidus temperature and widens the solidification temperature range. For example, segregation of sulphur in steel results in the formation of a low melting point Fe-S compound which decreases the solidus temperature to 988 °C, thereby increasing the solidification temperature range in steel [36][37][39][52]. During the last stages of solidification the remaining liquid can exist in the form of continuous films around the solidified grain boundaries with high levels of stress/strain accumulated at these boundaries, due to an extended solidification temperature range, which decreases the resistance of an alloy to cracking. Therefore, a wider solidification range generally increases the susceptibility of an alloy to solidification cracking. Additionally, the brittle temperature range as identified in the technological strength theory, is also influenced by the solidification temperature range. Matsuda et al. utilised the transverse vare-

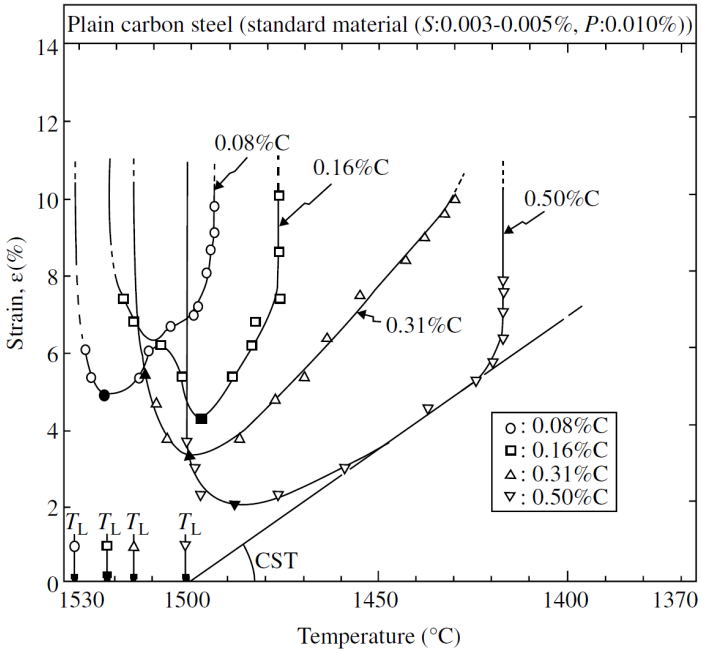

Figure 2.18: Brittle temperature range of plain carbon steels as measured by Matsuda et al. indicating the susceptibility to cracking as a measure of the angle of critical strain tangent (CST) [39].

straint test with a high-speed camera for dynamic observation of solidification and cracking during welding to quantify the BTR [46][53]. The results of their experiments on plain carbon steels indicate an increase in BTR with increasing levels of carbon. A larger BTR corresponds to an increased susceptibility to cracking due to a decreasing value of critical strain as indicated in Fig. 2.18 (smaller angle of critical strain tangent (CST)).

Primary solidification mode- Solidification of stainless steels proceeds in one of the following solidification modes- austenite (A), ferrite (F), primary austenite with ferrite (AF), primary ferrite with austenite (FA) [54]. In austenitic stainless steels, the effect of primary solidification mode is such that solidification in F or FA mode increases the resistance to cracking compared to A or AF mode [36][39][45]. Various researchers, Borland [44] and Matsuda [53] and Hull [55], have presented ideas in favour of cracking resistance of δ-ferrite that largely forms during F/FA solidification mode [45]. Higher solubility of elements like S, P and Si in δ-ferrite compared to austenite limits the extension of solidification temperature range, which increases resistance to cracking [36][37][45]. In Fig. 2.18, an increase in BTR is noticed for increasing carbon content which is attributed to a shift from F to A solidification mode and the enhanced segregation of impurity elements in the A mode.

Segregation- Micro-segregation (local changes in composition) of certain alloying or impurity element during solidification can decrease the resistance of a material to cracking. Segregation occurs during non-equilibrium solidification of alloys and results in an enrichment of the solidifying liquid with the solute elements due to partitioning of these elements. The tendency or degree of partitioning of the solute elements is determined by the partition coefficient k, defined as,

$$k = X_s / X_l \tag{2.1}$$

where, X_s and X_l are mole fraction of solute in the solid and liquid phase, respectively. Segregation of certain elements, for example, S, P and B with a low partition coefficient in steel enrich the solidifying liquid and lead to the formation of low melting point compounds (FeS, Fe_3P). These low melting point compounds are likely

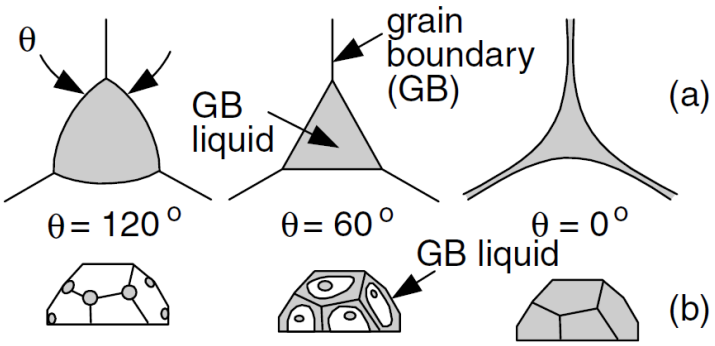

Figure 2.19: A schematic showing the effect of surface tension on distribution of grain boundary liquid a), dihedral angle and b), corresponding distribution of grain boundary liquid [36].

to form continuous liquid films along solidifying grain boundaries during terminal stages of solidification which increases the susceptibility of steel to solidification cracking [38].

Grain boundary liquid film and surface tension- Two extreme situations can exist for the amount and distribution of grain boundary liquid during solidification of an alloy. First, some alloys on solidification have little to no liquid distributed as grain boundary films and as a result, cracking does not occur. Second, is the availability of a large amount of grain boundary liquid generated at a composition that can heal or fill cracks emerging during solidification. For solidification cracking to occur, a situation exists between the two extremes where susceptibility to cracking is the highest for a particular composition (lambda curves) [34][56]. The susceptibility at this composition is a result of a continuous distribution of thin liquid films determined by the surface tension. If the surface tension is high, wetting does not occur and liquid exists as droplets. Whereas, low surface tension gives rise to wetting and subsequent formation of continuous liquid films with a low dihedral angle that facilitate cracking. Fig. 2.19 shows the effect of dihedral angle on distribution of grain boundary liquid [36].

Back-filling- During solidification liquid metal is drawn interdendritically to compensate for thermal contraction and solidification shrinkage. As the fraction of solid increases, the permeability of the mushy zone decreases which hinders the liquid metal flow. Due to increased resistance to liquid metal flow during terminal stages of solidification, cavities may form which can act as crack initiation sites [34]. The concept of back filling is central to the model proposed by Feurer [57] on solidification cracking. According to it, solidification cracking is likely to occur if the rate of feeding (ROF) is less than the rate of shrinkage (ROS). Also, the weldability of aluminium copper alloys can sometimes be improved by adjusting the composition so that sufficient amount of liquid is formed in order to promote back-filling to avoid solidification cracking [36].

2.4.2 THERMO-MECHANICAL FACTORS

Thermo-mechanical factors can arise due to the imposed weld thermal cycle and/or the external restraint by means of clamps or fixtures used to keep the workpiece in place. Therefore, the extent of the stress/strain state or the strain rate that develops during solidification is influenced by these factors. Cracking is likely to occur when the solidifying microstructure cannot withstand the developing forces.

Stress- Stress based models have been proposed that predict cracking once a critical or a fracture stress (strength of the semi-solid mush) is exceeded. Zacharia [58] in his stress based model shows how the na-

ture of stresses at the trailing edge of the weld pool changes from compressive to tensile. The length behind the weld pool at which the shift happens is characteristic to a material [59]. According to the model, cracking is believed to occur when the mushy zone extends to the zone in which tensile stresses prevail. Locally, stresses in the transverse direction of the melt (weld pool) can be high enough so that strength of the solidifying structure is exhausted. In this case cracking is likely to occur. Additionally, external restraint arising from clamping or fixtures can also add to the level of tensile stress.

Strain- The strain theory (discussed in Section 2.3.3), highlights the rupture of intergranular liquid films when a critical strain is exceeded. Building upon the concepts of strain theory Prokhorov [60] and Senda et al [61] formulated ductility curves. As shown in Fig. 2.16 ductility curves comprise of a BTR where an alloy is most susceptible to cracking due to a loss in ductility of the semi-solid material. The BTR is generally contained within the solidification temperature range but may extend over a wider temperature range due to segregation during non-equilibrium solidification which can also result in the formation of low melting point compounds. The point of minimum ductility in the BTR can be referred to as the ductility limit. As solidification proceeds strain starts to accumulate and solidification cracking occurs when the total accumulated strain exceeds the ductility limit.

Strain rate- The idea that a critical strain rate must be exceeded for cracking to occur is becoming increasingly popular as more recent models of solidification cracking take into account a critical strain rate for the onset of cracking. From the use of ductility curves it can be understood that the rate of deformation determines if the necessary critical strain for cracking is exceeded while liquid films persist. Matsuda *et al.* [46] using the slow bending transverse-varestraint test established the critical strain rate for temperature drop (CST) in ductility curves to evaluate cracking susceptibility of carbon steels and austenitic steels. As shown in Fig. 2.20 cracking occurs when the deformation curve intersects the ductility curve (a line with a larger slope than that of CST) and CST correlates well with cracking susceptibility of an alloy. However, it should be noted that application of this technique is not widely adopted due to the complicated nature of the process. Later, Lin et al. used the transverse varestraint test with rapid bending to quantify the solidification cracking temperature range (SCTR) of alloys and used it as a measure of cracking susceptibility [50]. The importance of strain rate arises from an understanding of the deformation behaviour of the semi-solid material. The mush responds to existing strains by appropriate liquid feeding, plastic deformation, reordering of the existing structure and diffusion creep [34]. For these processes to occur, a certain amount of time is required, and the application of higher strain rates leads to an absence of the necessary time therefore increasing the tendency of solidification cracking.

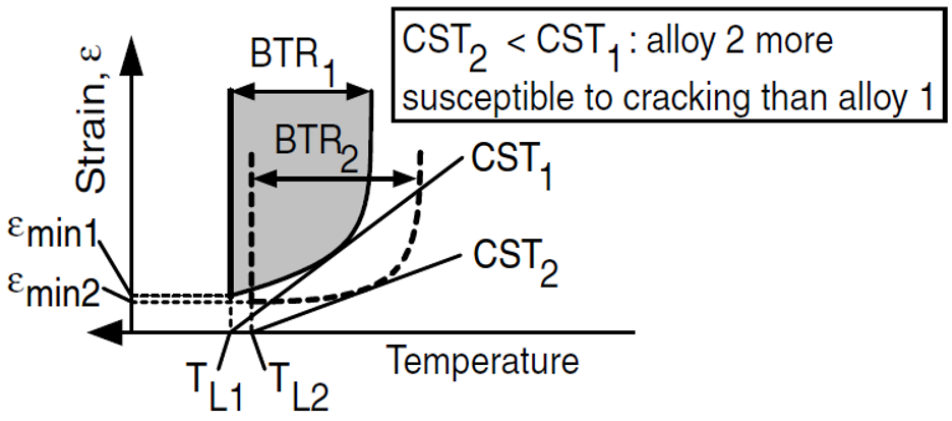

Figure 2.20: A schematic illustrating the evaluation of solidification cracking susceptibility based on the angle of CST [36].

2.4.3 SUMMARY

Apart from the factors discussed in previous sections, several other factors like grain size, grain type, liquid feeding during the last stage of solidification, weld pool shape may influence the susceptibility to solidification cracking. A fine grain structure is advantageous as it leads to lower strain accumulation per grain boundary. Fine equiaxed grains are less susceptible compared to coarse grains due to a higher fracture stress for finer grains as pointed out by Eskin *et al.* [43] in their review on hot tearing in aluminium alloys. During terminal stages of solidification, an extensive solid network can form which can drastically reduce liquid feeding to overcome cracking also, the permeability of the mush and dendrite coherency affect liquid feeding. More recently, a study conducted by Kou [35] on aluminium alloys and Agarwal *et al.* [62] on TRIP steel indicates the difficulty in liquid feeding when longer and narrower feeding channels form, respectively, making an alloy prone to cracking [63]. The Shape of the weld pool can also have an influence on the cracking tendency of an alloy. High welding speeds produce tear drop shaped weld pools, as shown in Fig. 2.5 b, which are likely to increase the susceptibility to cracking due to pronounced centre-line segregation and strain localisation [36]. Taking a closer look at the identified factors, it becomes clear that prediction of solidification cracking is not a straightforward task. During solidification a complex interaction between various factors arises as illustrated by a solidifying equiaxed dendritic melt in Fig. 2.21, which decides the tendency of an alloy to crack.

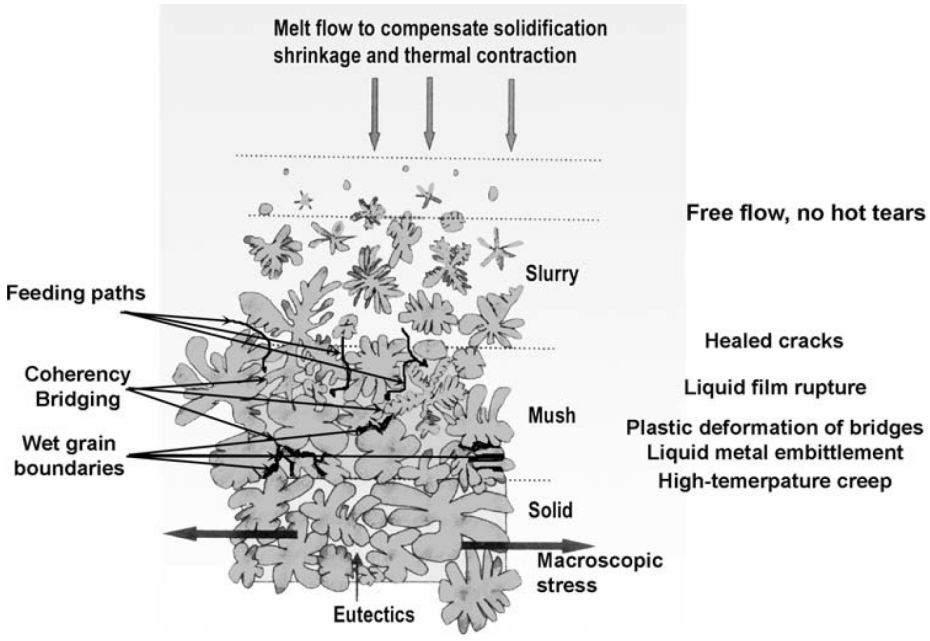

Figure 2.21: A schematic representing an equiaxed dendritic melt with interactions between multiple factors evolving during melt solidification identified to have an influence on solidification cracking [34].

2.5 WELDABILITY TESTING

Several tests have been designed for assessing the hot cracking susceptibility of materials. The existing tests are mainly classified as intrinsic or extrinsic tests. In intrinsic tests thermo-mechanical factors favourable for cracking arise due to self-restraint conditions (geometry of the specimen) whereas, external loading mechanisms are used in extrinsic tests. Intrinsic tests are used for a qualitative comparison of susceptibility to solidification cracking of alloys based on measurement of crack length. Whereas, extrinsic tests have a much

wider scope as there is a possibility to rank materials based on crack length and also evaluate weldability based on measurement of critical conditions (strain, strain rate and pre-load) for a set of welding conditions that lead to cracking. A summary of various tests is depicted in Fig. 2.22, and some test methods are discussed below.

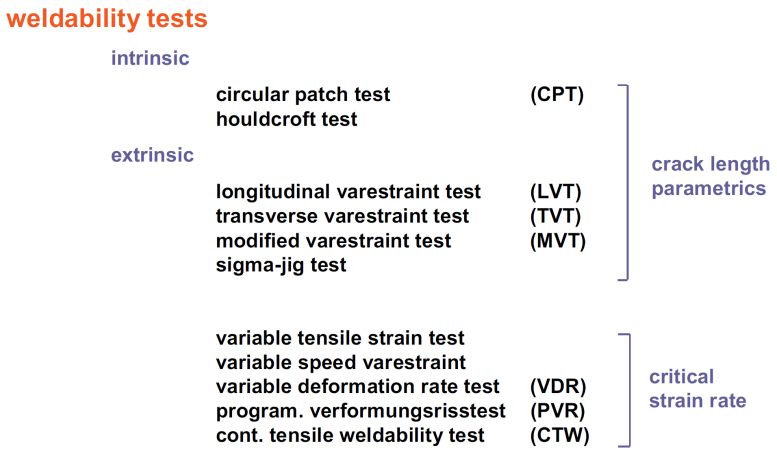

Figure 2.22: Classification of weldability tests according to generation of restraint conditions during testing [64].

Houldcroft test- It is also commonly known as the fishbone test. The specimens are prepared with increasing depth of slots which allows for a continuous decrease in material restraint. Welding is generally performed in the middle of the plate in the direction of increasing slot depth as shown in Fig. 2.23, with a possibility to weld from the other end as well. The former manner of welding has a high likelihood of solidification cracking due to greater self-restraint during start of the weld. The increasing slot depth in the welding direction makes the specimen compliant to developing stresses, which may stop the propagating crack at a certain distance from the starting point. In this manner alloys that result in longer crack lengths are ranked higher while studying the solidification cracking susceptibility of alloys.

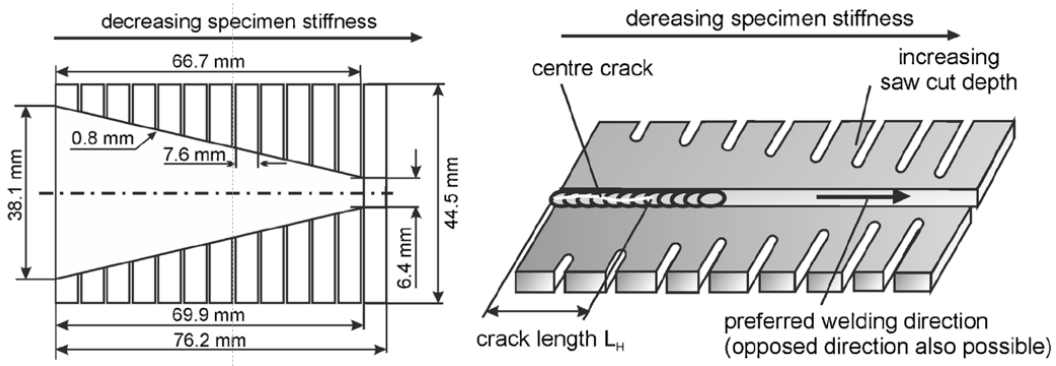

Figure 2.23: A schematic of the Holdcroft test and the commonly practiced test set-up [59].

VDEh standard hot cracking test- The standard hot cracking test was developed by the VDEh steel institute, Germany and provides a quick way to assess cracking susceptibility of thin steel sheets. The test was mainly developed for categorising weldability of automotive steels during laser welding. Sample preparation comprises of preparing rectangular sheets measuring 90×45 mm^2. Bead-on-plate laser welding is performed at an angle of 7° as shown in Fig. 2.24. External clamping in the form of point clamps (enough to keep the plate

in position) is used. Welding speed is determined by initially using 90% of the maximum power (to be used in the test) to obtain a fully penetrating stable keyhole. The determined speed is then used at the maximum power to perform 10 tests. After testing, the specimens are suspended in air for a minimum of 12 hours which allows for oxygen ingress into the crack and colours the crack surface blue. The specimens are then mechanically bent to reveal the coloured crack surface and the crack length is measured using a vernier caliper. The average crack length of the tested specimens is used to compare the cracking susceptibility of the alloys. It should be noted that the test is very sensitive to the free edge distance (3 mm in Fig. 2.24) and any deviation from it are likely to alter the resulting crack lengths.

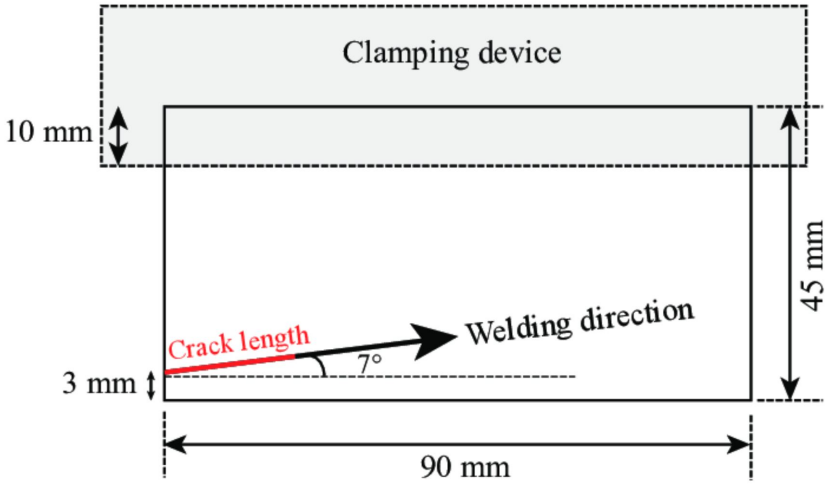

Figure 2.24: A schematic depicting of the test set-up adopted by the VDEh steel institute for the standard hot cracking test [17].

Varestraint test- Depending on the type and loading configuration, the varestraint test can be used to assess solidification, weld metal and HAZ liquation cracking [59]. The test specimen is mounted on a die as shown in Fig. 2.25 and welding is performed while the specimen is acted upon by a bending load. The bending rate is controlled to generate a pre-determined strain level on the specimen surface whose magnitude can be approximated by:

$$\epsilon_{\text{tot}} \approx 100 \times \frac{h}{2 \times R_{\text{M}}} \tag{2.2}$$

where, h is the sample thickness and R_M is the radius of the die. The test can be used to construct ductility curves and determine the critical strain/strain rate or simply measure the crack length to perform a qualitative solidification cracking susceptibility study of alloys for a set of welding conditions.

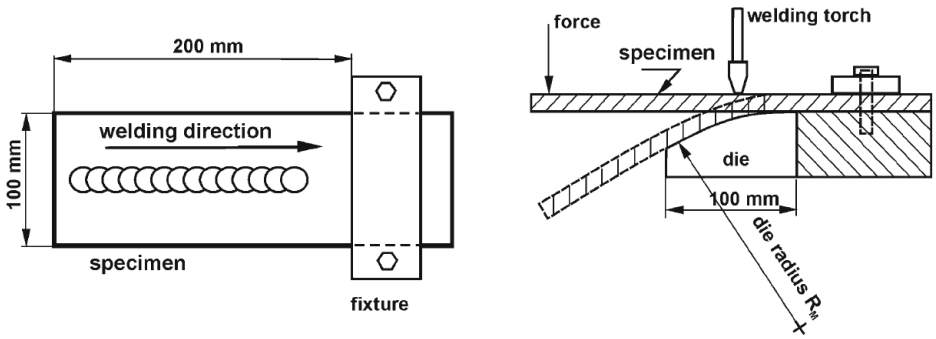

Figure 2.25: A schematic showing the test set-up for the varestraint hot cracking test [59].

U-type hot cracking test- Zhang [65] and Shinozaki *et al.* [66] developed the externally loaded U-type test for analysing cracking susceptibility of thin sheet metals. A schematic of the test set-up is shown in Fig. 2.26. Bead-on-plate welds are performed with a possibility of a static tensile pre-stress to act on the specimen. The level of pre-stress acting on the specimen can be varied by controlling the deformation of the webs prior to clamping. Regardless of the simplicity of the test it is necessary to use additional instrumentation to quantify the applied pre-stress in order to maximise repeatability.

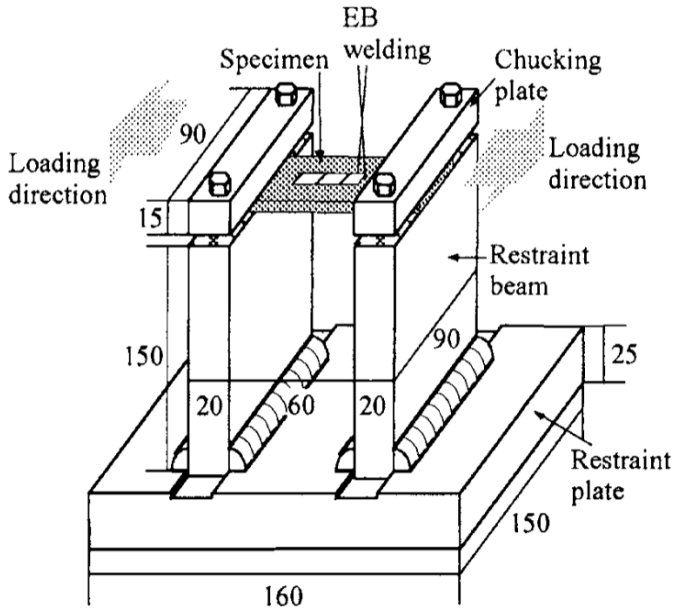

Figure 2.26: A schematic showing the test set-up for the U-type hot cracking test (all marked dimensions are in mm) [67].

3

EXPERIMENTAL AND NUMERICAL METHODOLOGY

In this chapter, materials used for the VDEh standard hot cracking test and corresponding welding parameters are discussed. The techniques used to characterise the microstructure and the laser beam are elaborated. In addition, thermal modelling to determine the laser beam welding process efficiency and weld pool shape is also described.

3.1 MATERIAL SELECTION

Three types of third generation AHSS obtained from the industrial partner of the project were used in the present study. Of the three, two are DP steels and one is a TRIP steel. For the course of this study the materials will be referred to as DP-1, DP-2 and TRIP, respectively. The material composition and the respective thickness is specified in Table 3.1. The representative binary phase diagrams for the materials obtained using Thermo-Calc are shown in Fig. 3.1, 3.2 and 3.3, respectively. Additionally, the solidification properties derived from the respective phase diagrams are also mentioned in Table 3.2. For the carbon content of the materials, as specified in Table 3.1 the solidification behavior of the three steels used in this study is similar in nature until the peritectic point. Cooling of the liquid melt proceeds with the formation of ferrite (δ) phase. The two phase (liquid (L) and ferrite (δ)) mixture undergoes a peritectic reaction resulting in the formation of the austenite phase (γ). Thereafter, for DP-2 and TRIP steel the remaining liquid and ferrite is completely transformed into austenite (γ) on cooling. However, for DP-1 the three phase (L + δ + γ) mixture following the peritectic reaction is transformed into a two phase ($\delta + \gamma$) mixture before completely transforming into austenite (γ). Also, according to the phase diagrams the three phase region is more pronounced in TRIP steel when compared to the two DP steels.

Table 3.1: Composition of the materials (major alloying elements) used in the present study.

Elements, wt. %	C	Mn	Al	Si	Cr	P	S
DP-1 (1.3 mm)	0.11	2.01	0.046	0.053	0.56	0.01	0.002
DP-2 (1.25 mm)	0.15	2.09	0.68	0.1	-	0.009	0.001
TRIP (1.25 mm)	0.19	1.63	1.1	0.35	0.019	0.089	0.005

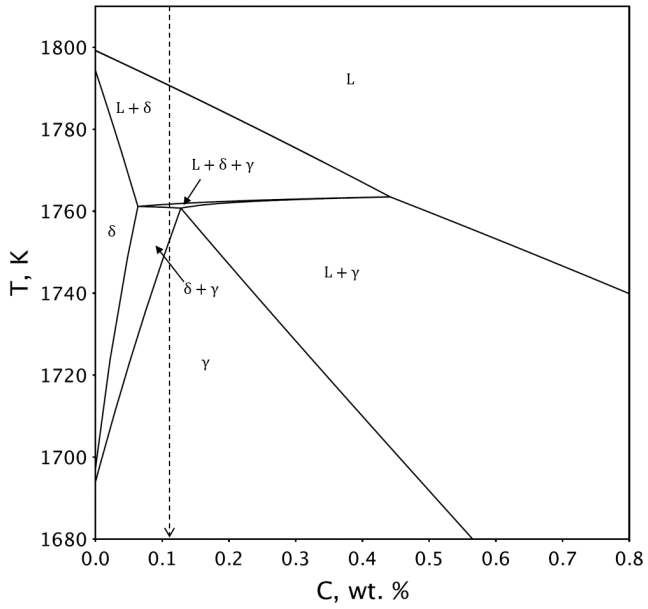

Figure 3.1: Representative binary phase diagram for DP-1 steel used in the present study (calculated using Thermo-Calc).

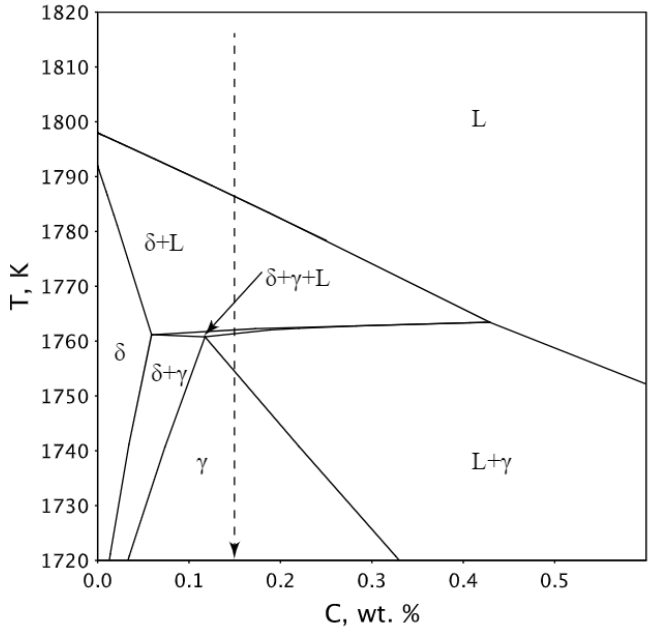

Figure 3.2: Representative binary phase diagram for DP-2 steel used in the present study (calculated using Thermo-Calc) [17].

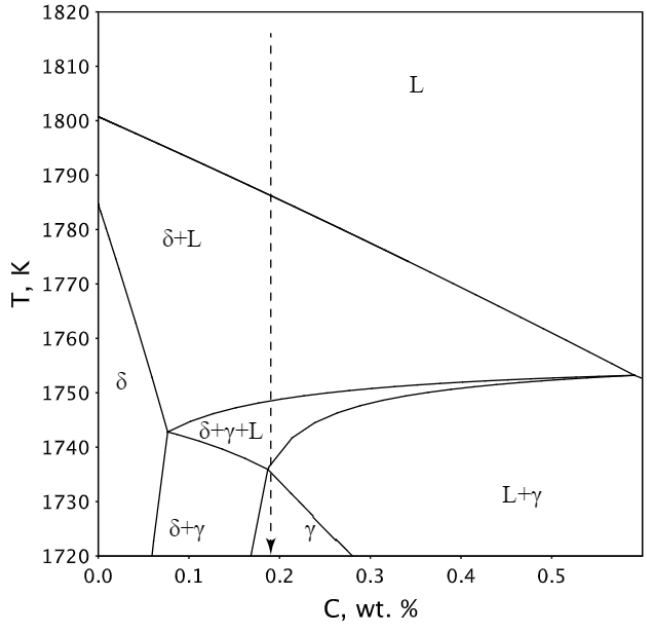

Figure 3.3: Representative binary phase diagram for TRIP steel used in the present study (calculated using Thermo-Calc) [17].

Table 3.2: Liquidus temperature and equilibrium solidification temperature range derived from the representative binary phase diagrams for materials used in the present work.

Material	Liquidus temperature (K)	Equilibrium solidification temperature range (K)
DP-1	1790	30
DP-2	1786	33
TRIP	1786	50

3.2 LASER BEAM WELDING SET-UP

3.2.1 HOT CRACKING TESTS AT TATA STEEL

As a part of the present study hot cracking tests are also performed at Tata Steel's laser welding facility. Bead-on-plate laser welding experiments according to the VDEh standard hot cracking test are performed using a Trumpf 4.5 kW Nd:YAG laser. The spot size of the laser beam at focus is 0.6 mm and the operating wavelength is 1030 nm. The testing parameters for the three materials are listed in Table 3.3.

Table 3.3: Testing parameters for the materials used in the present work tested at the external facility.

Material	Welding speed (mm/s)	Laser power (kW)	Spot size (mm)
DP-1	167.0	4.0	0.6
DP-2	176.0	4.0	0.6
TRIP	167.0	4.0	0.6

3.2.2 LASER BEAM WELDING SET-UP AT DELFT

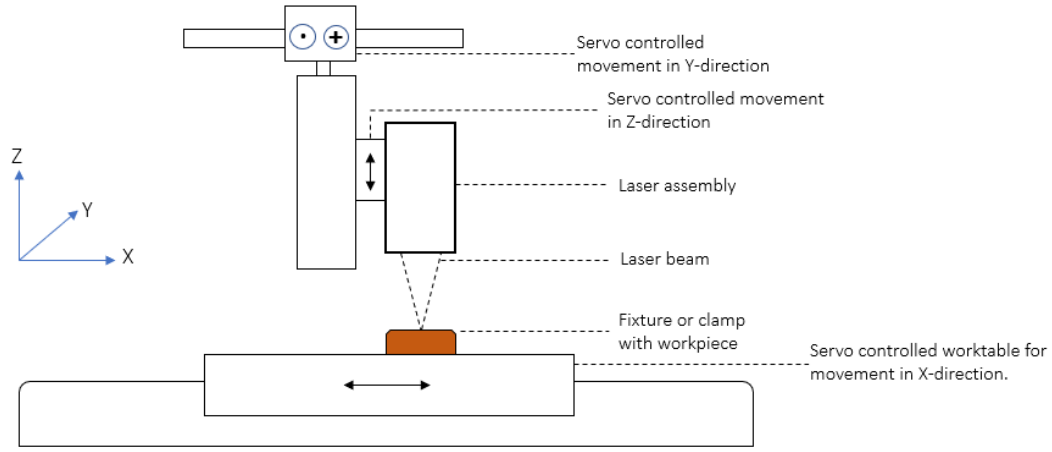

Figure 3.4: A schematic of the LBW set-up used to conduct experiments in the present study.

A 8 kW Trumpf TruDisk-8002 Nd:YAG disk laser was used to conduct bead-on-plate laser welding experiments. The focusing optics, comprised of an objective and a collimator lens, with a focal length of 200 mm. The operating wavelength is 1030 nm and the laser beam spot size at focus is 0.2 mm with a possibility to de-focus using, both collimator movement and laser head movement in Z-direction as shown in Fig. 3.4. To rank the susceptibility of materials to hot cracking, the VDEh standard hot cracking test as discussed in Section 2.5 is followed. Also, no shielding gas is used while conducting the laser welding experiments as the standard does not mention the use of a shielding gas and from a previous study use of shielding gas was found to have no impact on the cracking tendency of materials [17]. For the three materials used in this study, 90 × 45 mm^2 samples were mechanically cut under the action of a shear force. Due to the limited accuracy of the cutting machine an error of ± 0.5 mm from the specified sample dimensions is present in the samples. Prior to testing the specimen surface is cleaned with iso-propanol. The specimens are placed at the focal plane of the laser welding machine where a focused laser beam spot of 0.2 mm is attained. To match the setting of Tata Steel's laser welding facility the beam is de-focused to obtain a focused laser beam spot of 0.6 mm using both methods of de-focusing as mentioned in Section 2.1.2. The three materials used in the study are tested independently for both ways of de-focusing to obtain a spot size of 0.6 mm to understand the influence of the de-focusing manner on cracking. Additionally all three materials are also tested at a spot size of 0.2 mm. A summary of the testing parameters is listed in Table 3.4. Lastly, the resulting average crack lengths from the two facilities are compared for the three materials used in the study.

Table 3.4: Testing parameters at Delft for the materials used in the present work.

Material	Welding speed (mm/s)	Laser power (kW)	Spot size (mm)
DP-1	167.0	4.0	0.2 and 0.6
DP-2	176.0	4.0	0.2 and 0.6
TRIP	167.0	4.0	0.2 and 0.6

3.3 ANALYSIS OF THE LASER BEAM

A beam analyser is used to measure the power density distribution, beam quality and the beam parameter product of the laser beam. A schematic of the PRIMES FocusMonitor FM+ used in this study to analyse the beam is shown in Fig. 3.5.

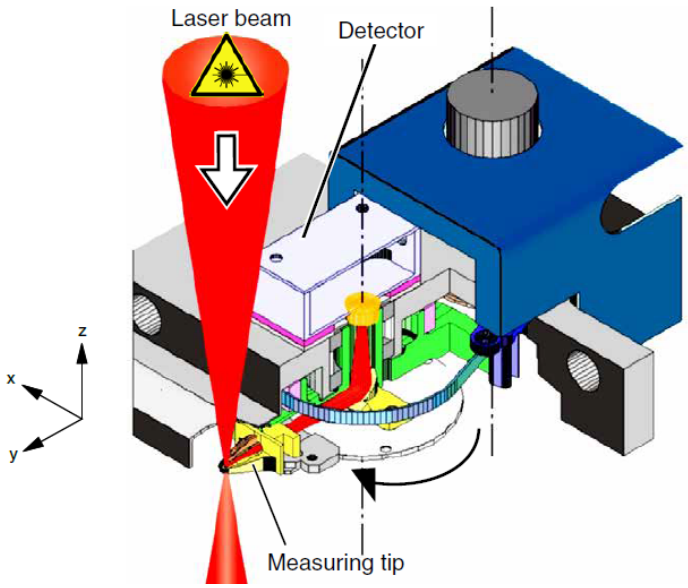

Figure 3.5: A schematic of the opto-mechanical assembly of the PRIMES FocusMonitor FM+ [68].

The beam analyser can measure the power density distribution from which other beam properties like the beam radius, focal position in space and the beam quality (M^2) are determined [68]. To measure the properties of a laser beam the device is placed in the optical path of the beam and within the focusing range of the optics. In this manner the laser beam is incident on a specialised rotating measuring tip with a hole. Part of the beam that fits the hole is guided on to a detector. The measuring tip is capable of translational motions in both Y and Z-directions. Accordingly, the tip performs linear cross-sectional scans of the beam and generates the spatial power density distribution. From the measured distribution, beam radius, focal plane and size, beam quality and the beam parameter product can be determined. The beam parameter product (BPP) is defined as:

$$BPP = \theta \times w_o, \tag{3.1}$$

and the beam quality factor is defined as:

$$M^2 = \frac{\pi \times \theta \times w_o}{\lambda}, \tag{3.2}$$

where, θ is the half-divergence angle of the beam in mrad, w_o is the beam waist radius in mm, and λ being the lasing wavelength. The measured power density distribution can be viewed and analysed using the PRIMES Laser Diagnostic Software and results are presented below.

Laser beam properties- The spatial intensity distribution of the laser beam at Delft is shown in Fig. a and b, which corresponds to intensity profiles at the focal plane with a laser beam spot diameter of 0.2 mm and the plane where the laser beam spot diameter is 0.6 mm. The spatial intensity distribution of the laser beam at Tata Steel in its focal plane with a laser beam spot diameter of 0.6 mm is shown in Fig. 3.6 c. From the measured intensity profile, the corresponding Beam Parameter Product (BPP) and the M^2 factor is obtained for the lasers and is listed in Table 3.5. The BPP and the M^2 factor can be used to characterise the quality

of a laser beam. The M^2 factor is calculated by dividing the BPP of a laser beam by that of an ideal beam which makes it a dimensionless number. A lower value of BPP and M^2 factor is representative of a laser beam with high quality. A high beam quality implies smooth wavefronts (i.e., strong phase correlation across the beam profile), such that focusing the beam with a lens allows one to obtain a focus where the wavefronts are plane [69]. The M^2 factor represents how well a laser beam can be focused for a given divergence and, also determines the radiance (brightness) of the beam, along with the optical power.

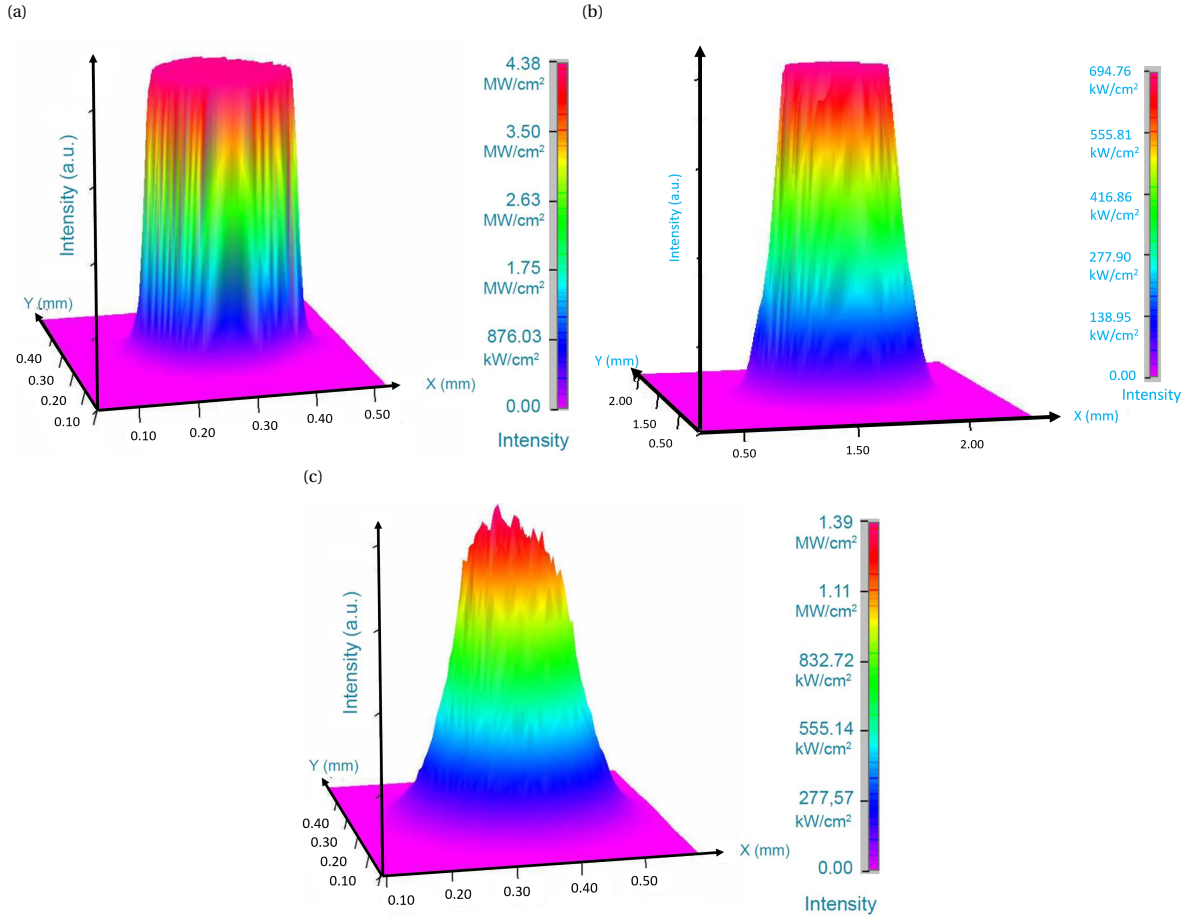

Figure 3.6: Spatial intensity distribution of the laser beam at Delft's LBW facility for a laser beam spot diameter of 0.2 mm in (a), 0.6 mm in (b). Whereas (c), shows the spatial intensity distribution of Tata Steel's LBW facility for a laser beam spot diameter of 0.6 mm.

Table 3.5: Laser beam characteristics of both welding facilities as derived from the respective spatial intensity distribution.

Laser beam welding facility	Delft	Tata Steel
w_o, mm	0.12	0.28
θ, mrad	84.5	90.1
BPP, mm·mrad	10.2	24.9
M^2 factor	30.3	73.7
Beam profile	Top hat distribution	Gaussian distribution

3.4 MICROSTRUCTURAL CHARACTERISATION

3.4.1 SAMPLE PREPARATION

The top surface, transverse and longitudinal cross-sections of the welds were prepared for microstructure investigation. The specimens were hot embedded using a conductive resin. Sample preparation started with a series of mechanical grinding steps using SiC abrasive papers (180 through 2400 grit size) in running water. Grinding was followed by by a two step polishing process. First, a 3 µm diamond suspension was used to get rid of the scratches from prior grinding and in the second step, 1 µm diamond suspension was used to obtain a mirror like surface finish. To reveal the microstructure, 2 % nital solution was used to etch the specimen surface for approximately 10 s followed by a thorough wash with iso-propanol and subsequent drying using an air blower.

3.4.2 OPTICAL MICROSCOPY

The etched specimens were analysed using a Keyence VHX-5000 optical microscope. It is a reflected light microscope which can be used to observe metallic surfaces. The illuminating system of the microscope generates visible light which is used for metallographic observations. A Kohler system directs the generated light beam from the illuminating system towards the specimen being observed and using the same system the reflected light rays from the surface of the specimen are used to form an image of the specimen surface [70]. The generated image can be viewed through an eyepiece or digitally by means of a camera. The relative ease of operation of optical microscopes justifies their extensive use for microstructural characterisation however, the limited resolution at high magnifications is a drawback of these microscopes.

3.4.3 SCANNING ELECTRON MICROSCOPE

Scanning electron microscopy (SEM) is a technique which enables us to achieve resolutions higher than conventional optical microscopes. The resolution of a microscope is limited by the wavelength of the incident beam. In optical microscopy, the incident beam is constituted of packets of photons whose wavelength is limited to 400 nm. In the case of matter waves, the De-Broglie wavelength is dependent on the momentum of the wave, which is in turn controlled by the acceleration voltages. By using electron beams, much lower De-Broglie wavelengths are achievable, depending upon the acceleration voltages, thereby achieving much higher resolutions. Conventional SEM, have typical energy range of (1-30 keV). The incident/primary beam of electrons interact with the constituents of the sample and emit secondary electrons which are detected by a Everhart-Thornley detector. The beam is raster scanned over the entire sample surface thereby generating an image of the entire surface. A backscattered electron detector is also used in some cases. The backscattered electrons originate from the subsurface regions of the sample, and their intensity/contrast is dependent directly on the atomic number of the constituent element. These electrons therefore helps us to gain a better understanding of the subsurface regime of the sample and also provides a quasi-elemental mapping of the surface.

3.5 FINITE ELEMENT MODELLING

Finite Element Modelling (FEM) is a powerful computational technique that is applied to real world engineering problems to develop meaningful solutions to these problems. Computational techniques of FEM are generally applied to a continuum of matter involving field variables. In the scope of FEM a domain is usually defined as a continuum (solid liquid or gas) with a known boundary [71]. The domain is further divided into a set of sub-domains known as finite elements that are connected to each other by a discrete collection of points called nodes [71]. The variables of interest are approximated at the nodes by obtaining solutions to partial differential equations that they satisfy. Whereas, within the elements the variables are calculated using interpolation functions. Therefore, computational time and accuracy of the solutions in a FEM study is directly linked to the size of the sub-domain set.

In this study, a 3-D finite element heat transfer model was set up in COMSOL Multiphysics, to obtain the thermal history of DP-1 and TRIP steel during bead-on-plate laser welding experiments. The thermal history determined from the model was experimentally validated using K-type thermocouples, spot-welded close to the fusion boundary. The heat transfer models were discretised using second order (quadratic shape functions) tetrahedral elements. The sensitivity of the mesh was analysed to determine the maximum element size for which the solution converges. In Fig. 3.7 a and b, the analysis of the mesh for a laser beam spot diameter of 0.2 mm and 0.6 mm is shown, respectively.

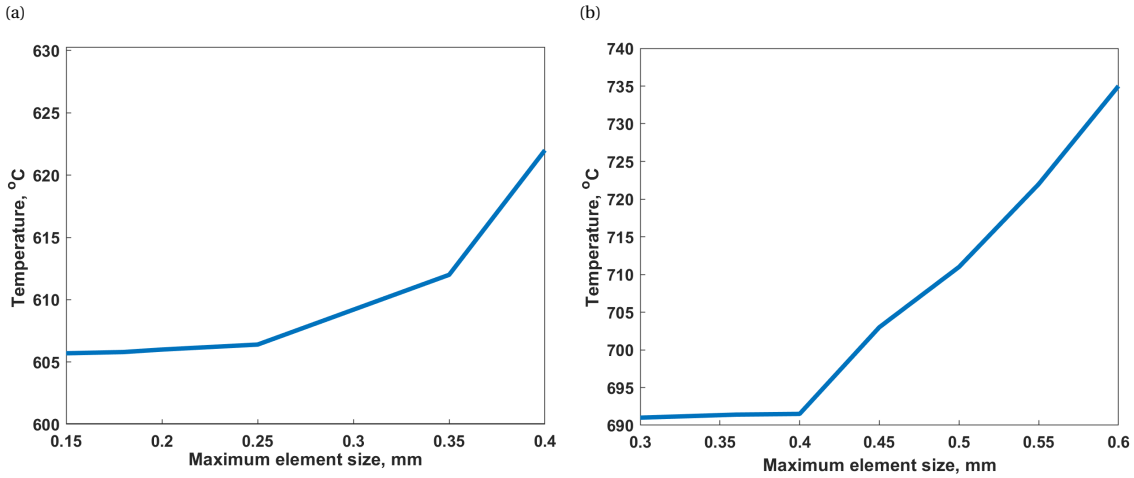

Figure 3.7: Analysis of the mesh in the thermal model with a laser beam spot diameter of 0.2 mm in (a) and 0.6 mm in (b).

The minimum volume of the elements in the weld zone of DP-1 and TRIP steel for different laser beam spot diameters is listed in Table, 3.6.

Table 3.6: Minimum elemental volume used in the heat transfer models of DP-1 and TRIP steel.

Material	Spot size (mm)	Min. element volume (mm^3)
DP-1 steel	0.2	0.0003
	0.6	0.0014
TRIP steel	0.2	0.0005
	0.6	0.0032

Temperature dependent thermo-physical properties were used for TRIP steel namely; thermal conductivity, specific heat capacity and density, and are shown in Fig. 3.8. Latent heat is taken into account following the effective specific heat method and can be expressed as:

$$C_p(T) = \begin{cases} C_{p,s}(T), & \text{T<T}_1 \\ C_p(T) + \frac{L}{T_2 - T_1}, & \text{T}_1 \leq \text{T} \leq \text{T}_2 \\ C_{p,l}(T), & \text{T>T}_2 \end{cases}, \tag{3.3}$$

where, $C_{p,s}$ and $C_{p,l}$ is the specific heat capacity of the solid and the liquid, respectively, L is the latent heat of melting, T_1 is the temperature at which melting begins and T_2 is the temperature at which melting is completed [72]. Due to lack of high temperature material properties of DP-1 steel, room temperature properties were used for it and were derived from the properties of a similar third generation dual-phase AHSS which were averaged over the measured temperature range as shown in Fig. 3.9.

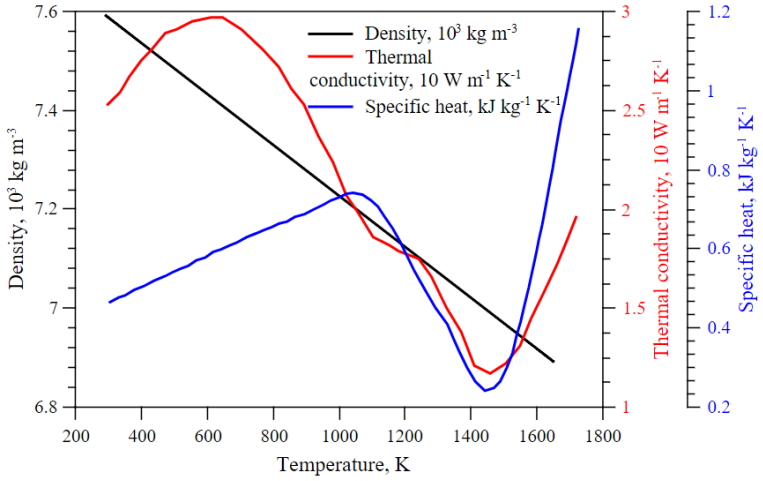

Figure 3.8: Thermo-physical properties for TRIP steel used in this study [73].

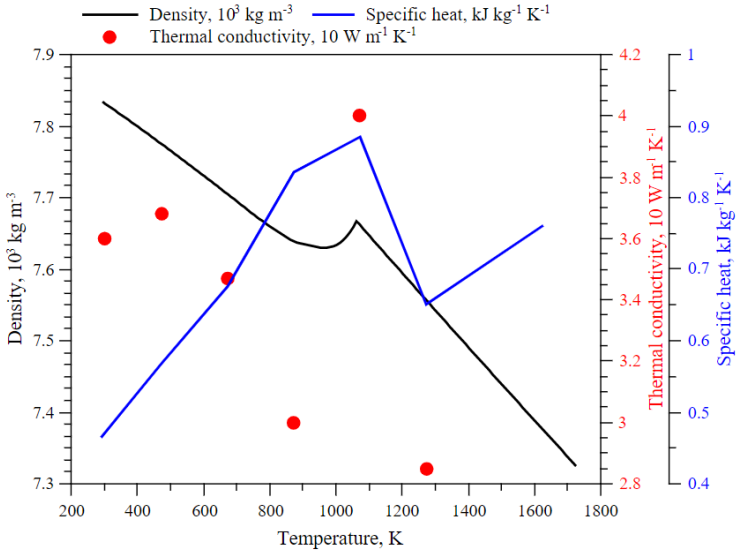

Figure 3.9: Thermo-physical properties of a third generation dual-phase AHSS utilised for obtaining room temperature properties of DP-1 steel used in this study [17].

To account for losses due to natural convection, a value of 10 $W{\cdot}m^{-2}{\cdot}K^{-1}$ was used for the convective heat transfer coefficient of air [74]. Radiative losses were taken into account by assuming a temperature dependent value for the emissivity of the plate surfaces determined by Equation 3.4 [75],

$$\epsilon = 0.7 - 0.02\exp\left(\frac{900}{T}\right). \tag{3.4}$$

To account for the laser heat input, a volumetric moving heat source is used which can be expressed as:

$$Q_v = \frac{Q_o \times \eta}{h}\exp\left[-2\left(\frac{r}{d_o}\right)^n\right], \tag{3.5}$$

where, Q_v is the net volumetric heat flux, Q_o is the peak intensity of the heat source, h is the height of the heat source, η is the net laser welding process efficiency, d_o is the diameter of the heat source on the plate surface, n is a positive integer whose value can be adjusted to take into account the spatial intensity distribution of a laser beam as shown in Fig. 3.10, and r is the radial distance from the centre of the heat source, expressed as:

$$r = \sqrt{x^2 + y^2}. \tag{3.6}$$

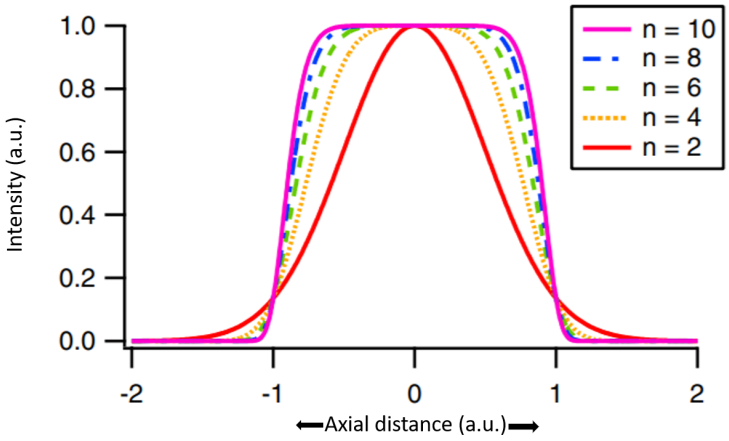

Figure 3.10: Spatial intensity profile of a laser source as a function of n [76].

The efficiency is determined from the model as a fitting factor. Efficiency values are plugged in the model and the numerically obtained thermal history is compared with the experimentally measured thermal history. Additionally, the size of the weld pool obtained from the model is compared with the size of fusion zone derived from microstructural observations. Therefore, the corresponding efficiency values for which the numerically obtained thermal history and weld pool size, agrees well with the experimentally obtained values are considered acceptable. The agreement between the experimental and numerical thermal history along with the size of the weld pool from microstructural observation and the models, also serves as a mean to validate the thermal models. Additionally, the process efficiencies determined from the FE-model are compared with analytically calculated energy transfer efficiency which is defined as the ratio of heat absorbed by the workpiece to the incident laser energy. The energy transfer efficiency (η_t) or the analytical LBW process efficiency can be determined using the Fuerschbach [77] model which is expressed here in the following form [78]:

$$\chi = \eta_t\Gamma\left[0.48 - 0.29\exp\left(\frac{-\eta_t\Gamma}{6.8}\right) - 0.17\exp\left(\frac{-\eta_t\Gamma}{59}\right)\right], \tag{3.7}$$

where, $\chi = v^2 A/\alpha^2$, $\Gamma = Pv/\alpha^2 H_{\mathrm{m}}$, v is the welding speed in mm·s^{-1}, A is the cross sectional area of the fusion zone in mm^2, α is the thermal diffusivity at liquidus temperature in mm^2·s^{-1}, P is the power delivered during the laser welding process in W, and H_m is the enthalpy of melting in J·mm^{-3}. Enthalpy of melting for steel is 10.4 J·mm^3, and the thermal diffusivity at liquidus temperature for DP-1 steel and TRIP steel is 6.2 mm^2·s^{-1} and 5.5 mm^2·s^{-1}, respectively [17] [77]. Lastly, the analytical and numerical values of process efficiency were plotted against the Specific Energy (SE), which is a convenient parameter to compare welds made with different levels of laser beam de-focusing, power and welding speed, and can be expressed as:

$$SE = \frac{P}{d_{\mathrm{f}} \times v}, \tag{3.8}$$

where, P is the laser power in W, d_{f} is the diameter of the laser beam on the workpiece in mm and v is the welding speed in mm·s^{-1}.
In this manner, the thermal history, weld pool characteristics and process efficiencies for different LBW conditions is obtained.

4

EXPERIMENTAL EVALUATION OF HOT CRACKING SUSCEPTIBILITY

In this chapter, the results obtained from the solidification cracking tests are provided. The crack length data for different testing conditions and corresponding weld metal macrographs are presented. A summary of the results arising from the conducted tests is also presented.

4.1 INTRODUCTION

Solidification cracks appear in the fusion zone of the weld with a distinct centre-line morphology as shown in Fig. 4.1 a and b. Solidification cracking arises from a complex interaction between metallurgical and thermo-mechanical factors that develop due to the imposed thermal cycle and the external restraint during welding. In addition to these factors, during laser welding of thin steel sheets process related factors can have an influence on the cracking tendency of an alloy. These factors are mainly identified as the spatial intensity distribution of the laser beam and welding parameters (spot diameter, power, speed and heat input). Processing conditions impact the keyhole during laser welding, which in turn determines a material's response to solidification cracking. Therefore, to establish a complete and concrete understanding of the phenomenon of solidification cracking during laser welding, it is important to comprehend the processing conditions.
Three advanced high strength automotive steels were tested following the testing procedure of the VDEh standard hot cracking test as explained in Section 2.5. The experimental setup is described in Fig. 2.24. The resulting average crack length from the tests is used to rank the alloys for their hot cracking susceptibility. Tests were performed using two different lasers following the similar experimental setup and procedure. A 8 kW Nd:YAG laser (Delft) with a spot diameter of 0.2 mm at focus and 4.5 kW Nd:YAG laser (Tata steel) with a spot diameter of 0.6 mm at focus. From here on, the two lasers are referred to as laser-1 (Delft) and laser-2 (Tata Steel), respectively. The material composition and equilibrium solidification properties are listed in Table 3.1 and Table. 3.2, respectively. Welding parameters used during the hot cracking tests for the two lasers are listed in Table 3.3 and Table 3.4. The results from the experiments are presented in the following sections.

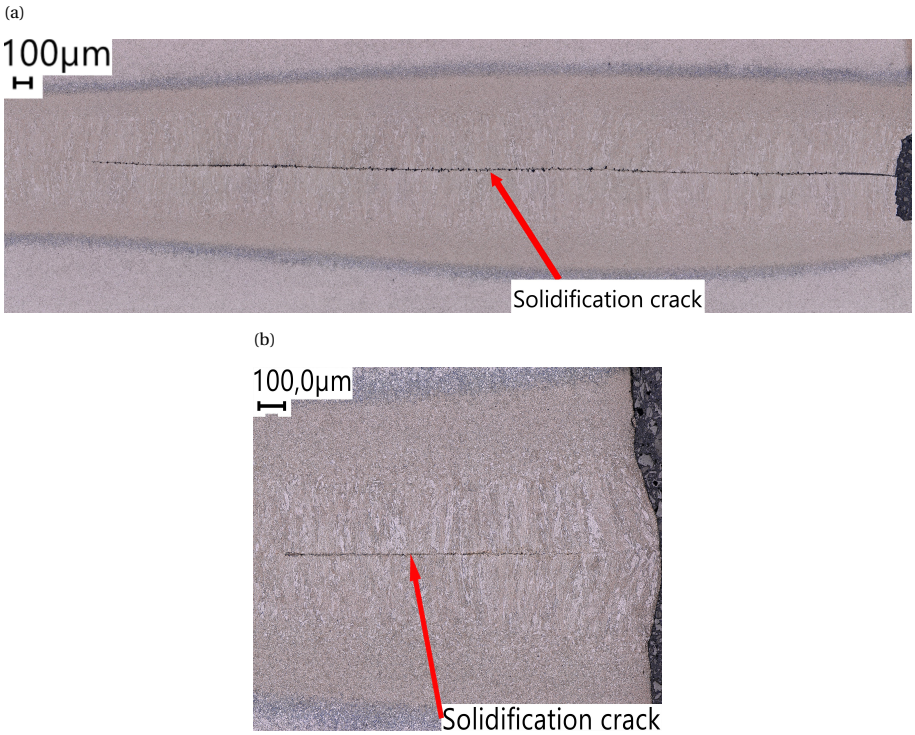

Figure 4.1: Top surface of the bead-on-plate weld indicating the weld centre-line solidification crack.

4.2 EXPERIMENTAL RESULTS OBTAINED USING LASER-1

4.2.1 CRACK LENGTH IN DP-1 STEEL

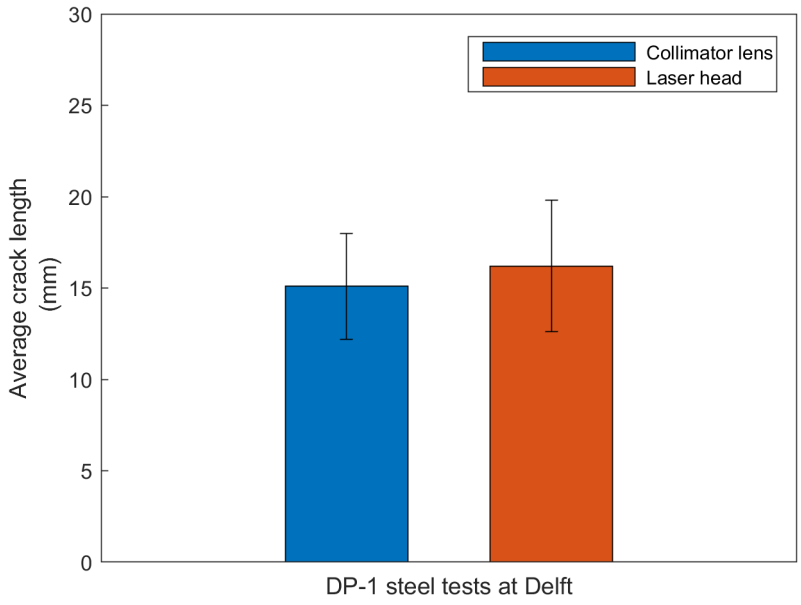

Figure 4.2: Average crack lengths for DP-1 steel tested with a laser beam spot size of 0.6 mm obtained through the movement of collimator lens and the laser head.

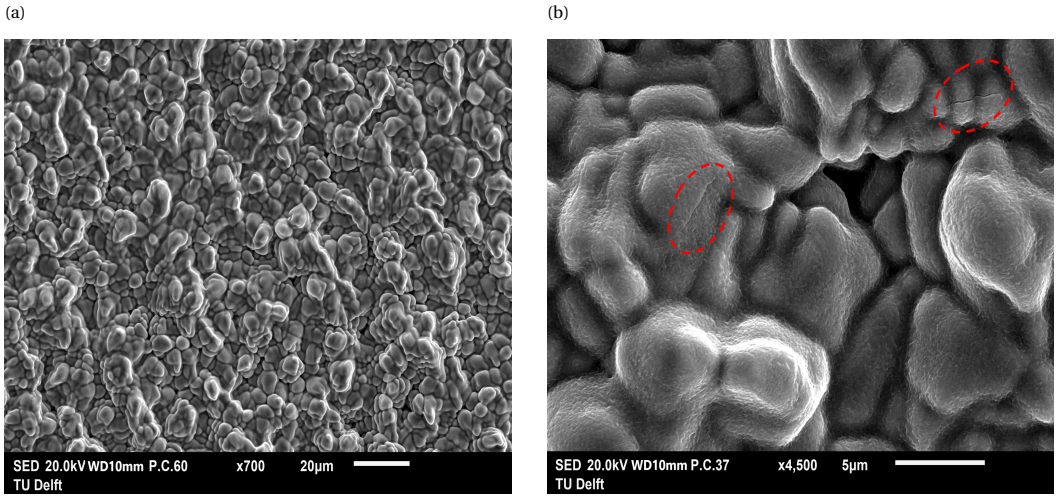

Figure 4.3: Fracture surface of the crack in DP-1 steel analysed using SEM revealing the dendritic morphology of the solidification crack in (a) and micro-cracks at dendrite tips in (b).

Average crack length for DP-1 steel in Fig. 4.2, tested with a laser beam spot diameter of 0.6 mm obtained through the movement of the collimator lens and the laser head is 15.1 mm and 16.2 mm, respectively. The corresponding standard deviation for the tests is 2.9 mm and 3.7 mm, respectively. The fracture surface of the specimen, as shown in Fig. 4.3 a, reveals a dendritic morphology which is typical for solidification cracks and micro-cracks are also observed at dendrite tips as shown in Fig. 4.3 b, that form during the terminal stage of solidification.

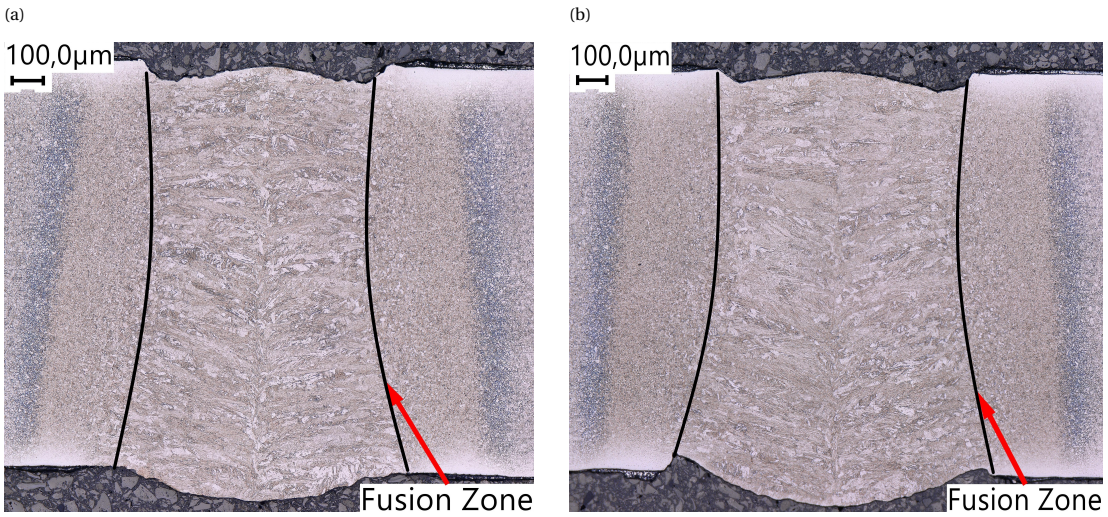

Figure 4.4: Cross section of the bead-on-plate welds perpendicular to the welding direction for DP-1 steel tested with a laser beam spot diameter of 0.6 mm obtained through the movement of collimator lens in (a) and the laser head in (b).

The cross section of the bead-on-plate welds, perpendicular to the welding direction, prepared from the specimens of the above performed tests are shown in Fig. 4.4. These cross sections are prepared at a location which is further ahead of the solidification crack due to which the centreline solidification crack is not visible here. The cross section area of the fusion zone in Fig. 4.4 a and b, is 1.0 mm^2 and 1.1 mm^2, respectively. While performing bead-on-plate welding with a laser spot diameter of 0.2 mm, solidification cracking is not observed. The cross section of the bead-on-plate weld for this case is shown in Fig. 4.5 a and the area of the

fusion zone is 0.4 mm^2. In addition to this, the laser beam spot diameter is decreased from 0.6 mm and bead-on-plate LBW is performed to determine the maximum spot size at which solidification cracking does not occur in DP-1 steel. This is achieved at a laser beam spot diameter of 0.4 mm without changing the welding speed and laser power. The cross section for this case is shown in Fig. 4.5 b, and the area of the fusion zone is 0.6 mm^2. This can be referred to as the critical spot size and weld size of DP-1 steel for the welding speed and laser power listed in Table 3.4.

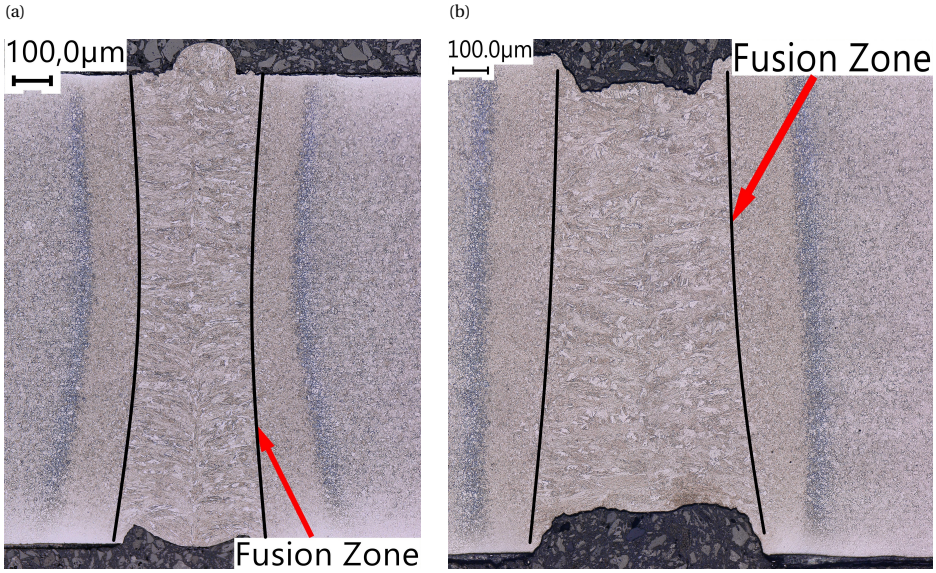

Figure 4.5: Cross section of the bead-on-plate weld perpendicular to the welding direction for DP-1 steel obtained with a laser beam spot diameter of 0.2 mm in (a) and 0.4 mm in (b).

4.2.2 CRACK LENGTH IN DP-2 STEEL

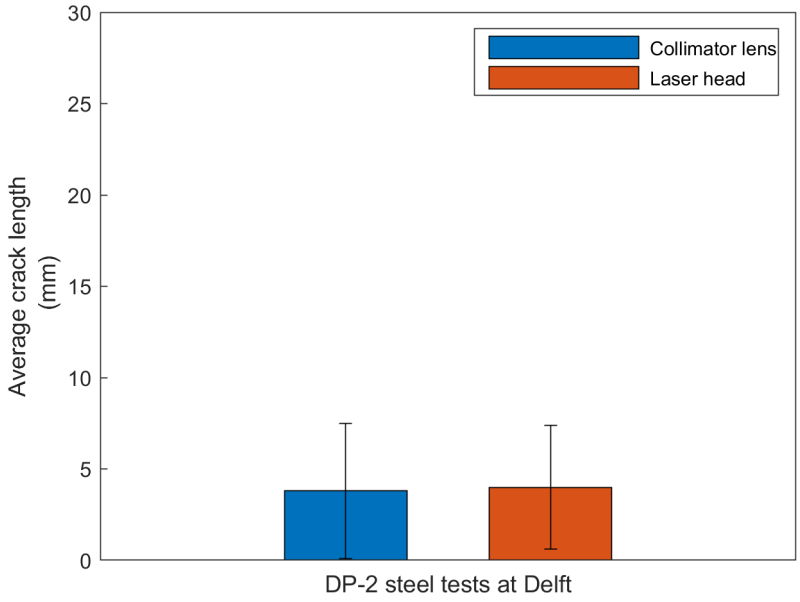

Figure 4.6: Average crack lengths for DP-2 steel tested with a laser beam spot diameter of 0.6 mm obtained through the movement of collimator lens and the laser head.

Average crack length for DP-2 steel in Fig. 4.6, tested with a laser beam spot diameter of 0.6 mm obtained through the movement of the collimator lens and the laser head is 3.8 mm and 4 mm, respectively. The corresponding standard deviation for the tests is 3.7 mm and 3.4 mm, respectively. It can be noted that the resulting average crack length in DP-2 steel is significantly lower than the average crack length in DP-1 steel. The fracture surface of the specimen, as shown in Fig. 4.7 a, reveals a dendritic morphology which is typical for solidification cracks and micro-cracks are also observed at dendrite tips as shown in Fig. 4.7 b, that form during the terminal stage of solidification. The cross section of the bead-on-plate welds, perpendicular to the welding direction, prepared from the specimens of the above performed tests are shown in Fig. 4.8. These cross sections are prepared at a location which is further ahead of the solidification crack due to which the centreline solidification crack is not visible here. The cross section area of the fusion zone in Fig. 4.8 a and b, is 1.0 mm^2 and 1.1 mm^2, respectively.

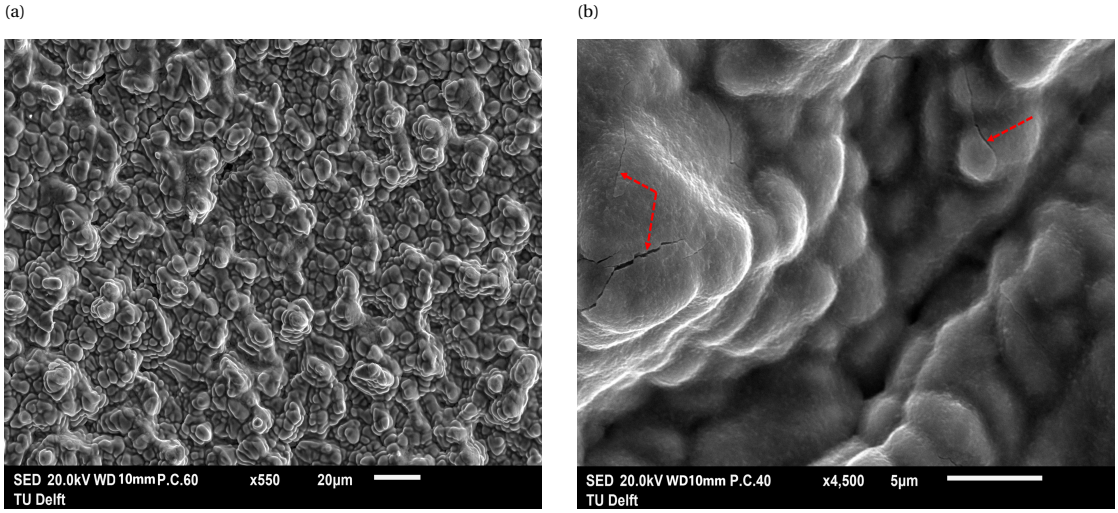

Figure 4.7: Fracture surface of the crack in DP-2 steel analysed using SEM revealing the dendritic morphology of the solidification crack in (a) and micro-cracks at dendrite tips in (b).

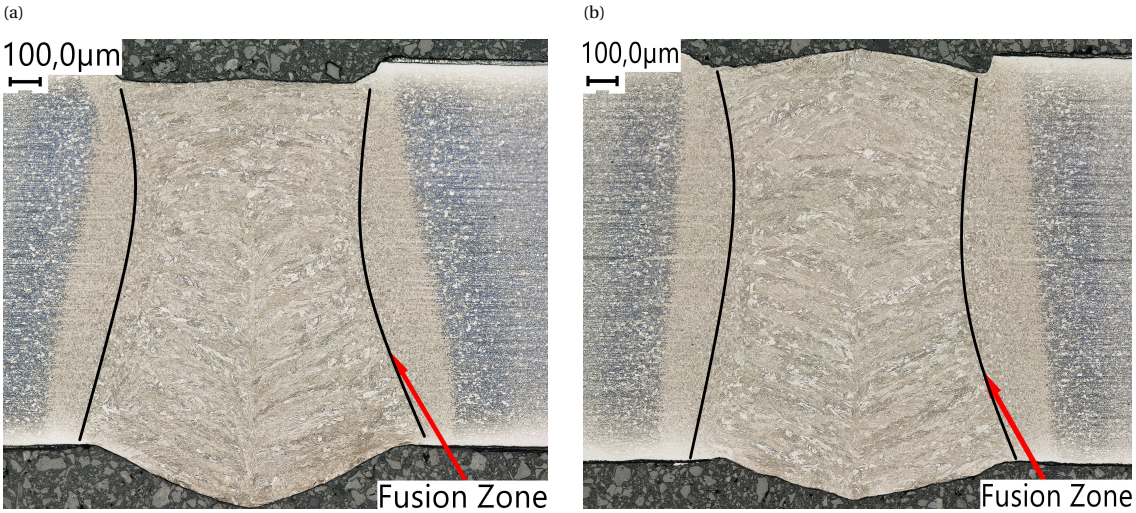

Figure 4.8: Cross section of the bead-on-plate welds perpendicular to the welding direction for DP-2 steel tested with a laser beam spot diameter of 0.6 mm obtained through the movement of collimator lens in (a) and the laser head in (b).

While performing bead-on-plate welding with a laser spot diameter of 0.2 mm, solidification cracking is not

observed. The cross section of the bead-on-plate weld for this case is shown in Fig. 4.9 and the area of the fusion zone is 0.4 mm^2.

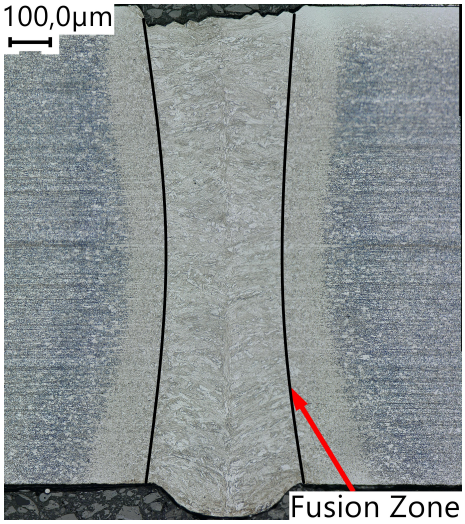

Figure 4.9: Cross section of the bead-on-plate weld perpendicular to the welding direction for DP-2 steel obtained with a laser beam spot diameter of 0.2 mm.

4.2.3 CRACK LENGTH IN TRIP STEEL

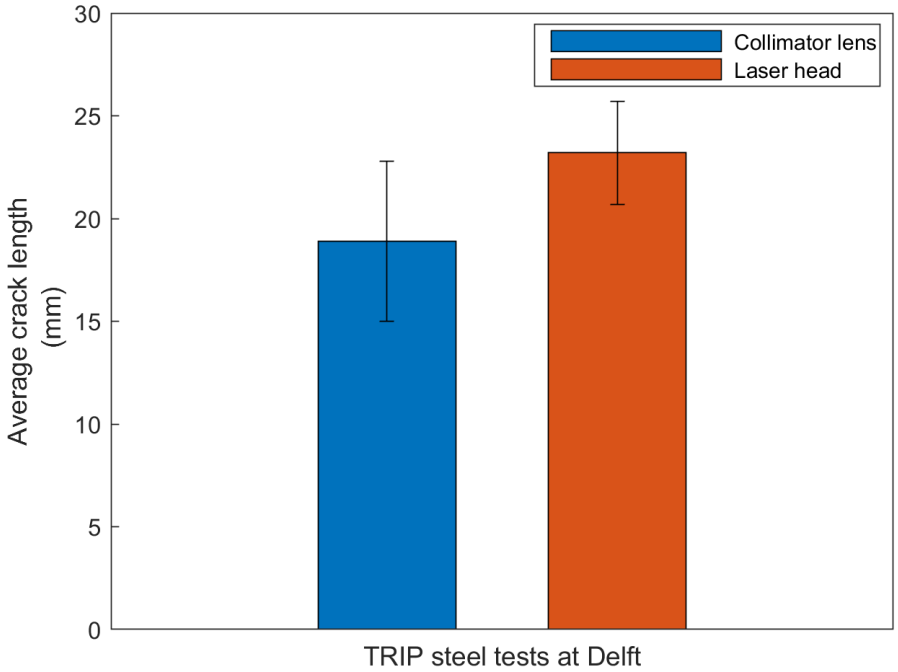

Figure 4.10: Average crack lengths for TRIP steel tested with a laser beam spot diameter of 0.6 mm obtained through the movement of collimator lens and the laser head.

Average crack length for TRIP steel in Fig. 4.10, tested with a laser beam spot diameter of 0.6 mm obtained through the movement of the collimator lens and the laser head is 18.9 mm and 23.2 mm, respectively. The corresponding standard deviation for the tests is 3.9 mm and 2.5 mm, respectively. It can be noted that the

resulting average crack length in TRIP steel is significantly higher than the average crack length in DP-1 steel and DP-2 steel. The fracture surface of the specimen, as shown in Fig. 4.11 a, reveals a dendritic morphology which is typical for solidification cracks and micro-cracks are also observed at dendrite tips as shown in Fig. 4.11 b, that form during the terminal stage of solidification. The cross section of the bead-on-plate welds, perpendicular to the welding direction, prepared from the specimens of the above performed tests are shown in Fig. 4.12. These cross sections are prepared at a location which is further ahead of the solidification crack due to which the centreline solidification crack is not visible here. The cross section area of the fusion zone in Fig. 4.12 a and b, is 1.0 mm^2 and 1.2 mm^2, respectively.

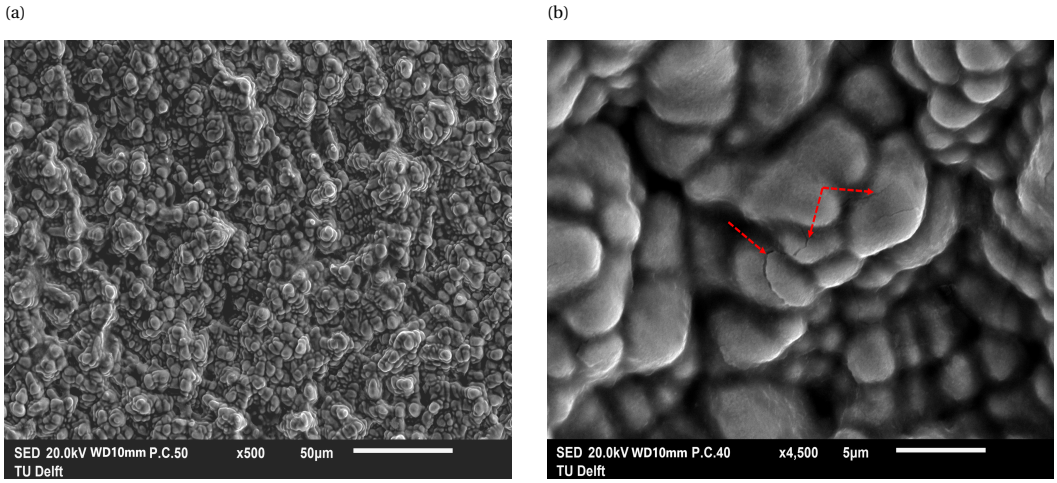

Figure 4.11: Fracture surface of the crack in TRIP steel analysed using SEM revealing the dendritic morphology of the solidification crack in (a) and micro-cracks at dendrite tips in (b).

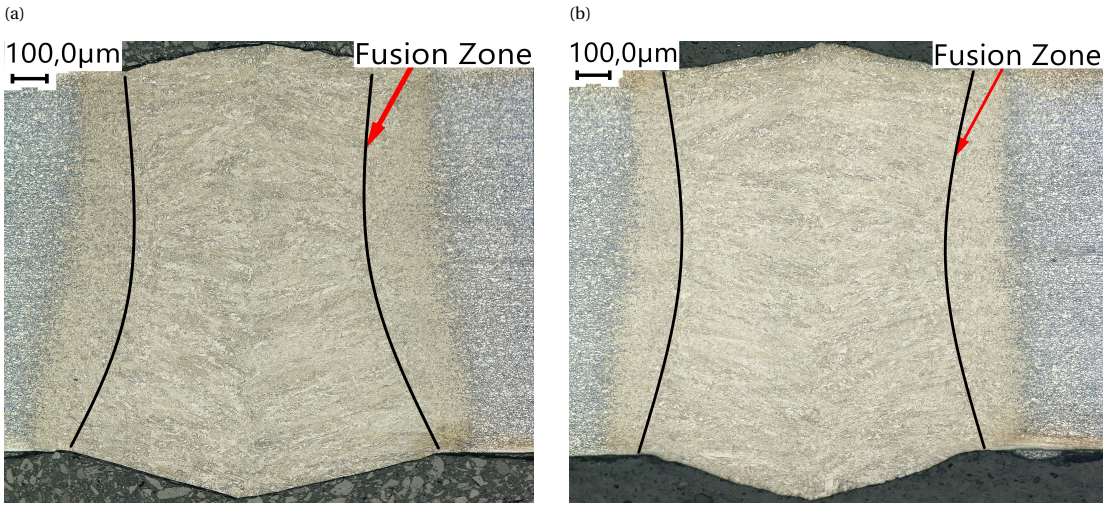

Figure 4.12: Cross section of the bead-on-plate welds perpendicular to the welding direction for TRIP steel tested with a laser beam spot diameter of 0.6 mm obtained through the movement of collimator lens and the laser head.

While performing bead-on-plate welding with a laser spot diameter of 0.20 mm, solidification cracking is not observed. The cross section of the bead-on-plate weld for this case is shown in Fig. 4.13 a, and the area of the fusion zone is 0.4 mm^2. In addition to this, the laser beam spot diameter is decreased from 0.60 mm and bead-on-plate LBW is performed to determine the maximum spot size at which solidification cracking does not occur in TRIP steel. This is achieved at a laser beam spot diameter of 0.25 mm without changing

the welding speed and laser power. The cross section for this case is shown in Fig. 4.13 b, and the area of the fusion zone is 0.5 mm^2. This can be referred to as the critical spot size and weld size of TRIP steel for the welding speed and laser power listed in Table 3.4. The critical spot size for TRIP steel, as determined experimentally, is smaller in comparison to DP-1 steel.

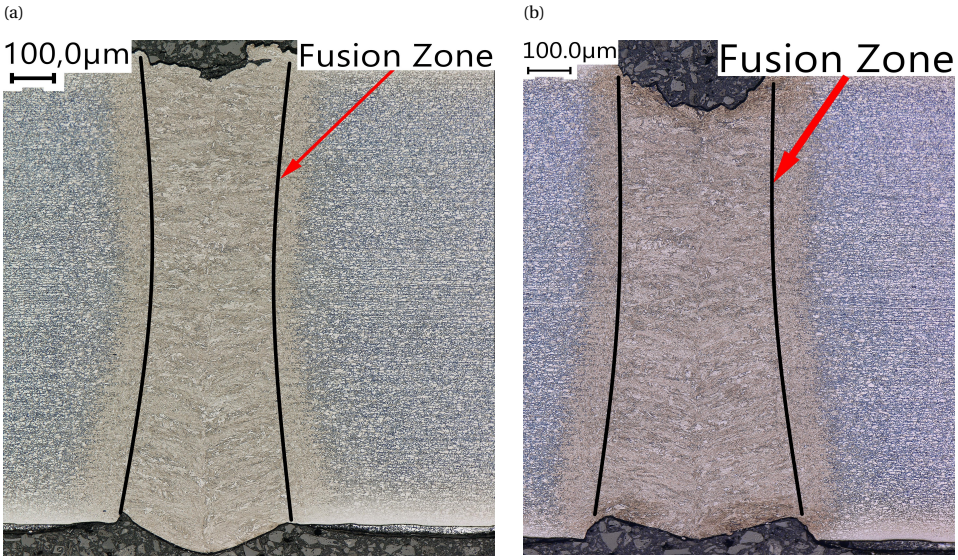

Figure 4.13: Cross section of the bead-on-plate weld perpendicular to the welding direction for TRIP steel obtained with a laser beam spot diameter of 0.2 mm in (a) and 0.25 mm in (b).

4.3 EXPERIMENTAL RESULTS OBTAINED USING LASER-2

4.3.1 CRACK LENGTH IN DP-1 STEEL

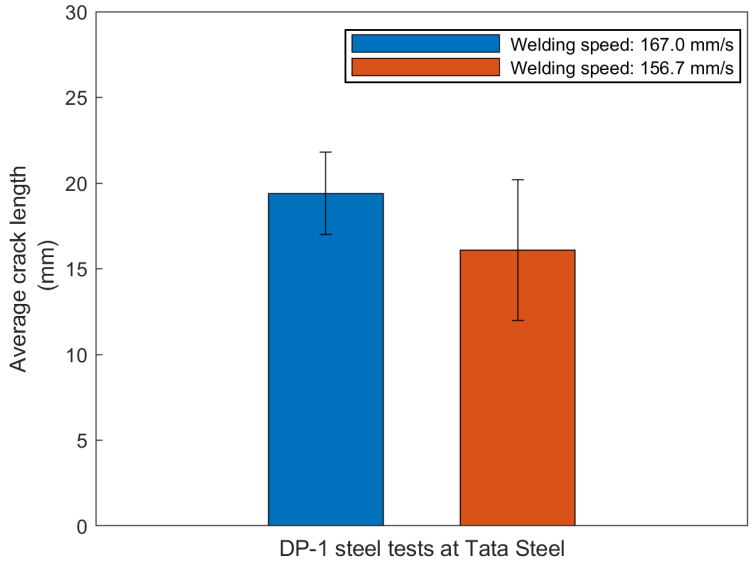

Figure 4.14: Average crack lengths for DP-1 steel tested with a laser beam spot diameter of 0.6 mm at a welding of 167.0 $mm{\cdot}s^{-1}$ and 156.7 $mm{\cdot}s^{-1}$.

Average crack length for DP-1 steel in Fig. 4.14, tested with a laser beam spot diameter of 0.6 mm at a welding speed of 167 mm·s^{-1} and 156.7 mm·s^{-1} is 19.4 mm and 16.0 mm, respectively. The corresponding standard deviation for the tests is 2.4 mm and 4.1 mm, respectively. The cross section of the bead-on-plate welds, perpendicular to the welding direction, prepared from the specimens of the above performed tests are shown in Fig. 4.15. The cross section area of the fusion zone in Fig. 4.15 a and b, is 1.2 mm^2 and 1.1 mm^2, respectively.

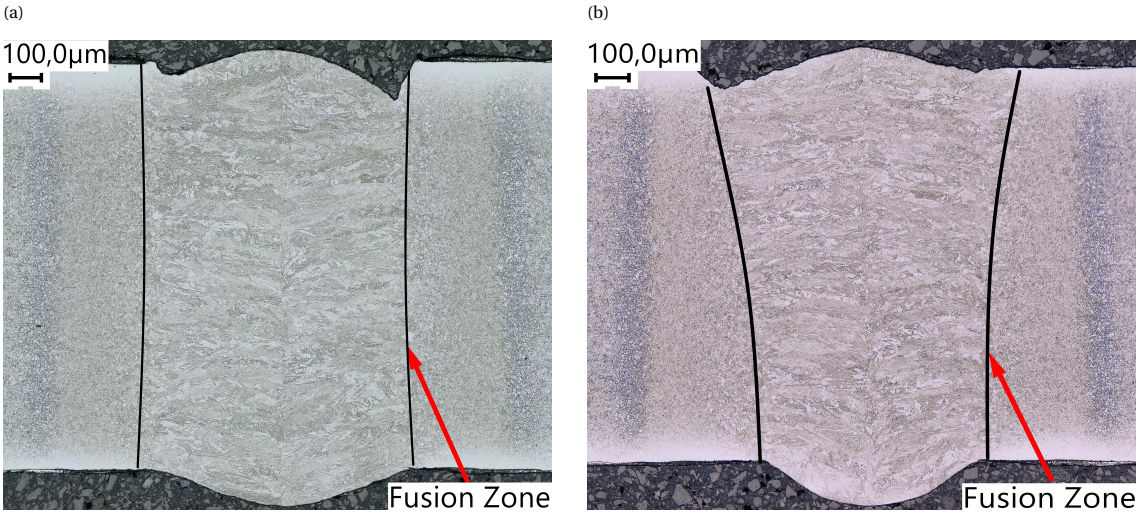

Figure 4.15: Cross section of the bead-on-plate welds perpendicular to the welding direction for DP-1 steel tested with a laser beam spot diameter of 0.6 mm at a welding speed of 167.0 mm·s^{-1} in (a), and 156.7 mm·s^{-1} in (b).

4.3.2 CRACK LENGTHS IN DP-2 STEEL AND TRIP STEEL

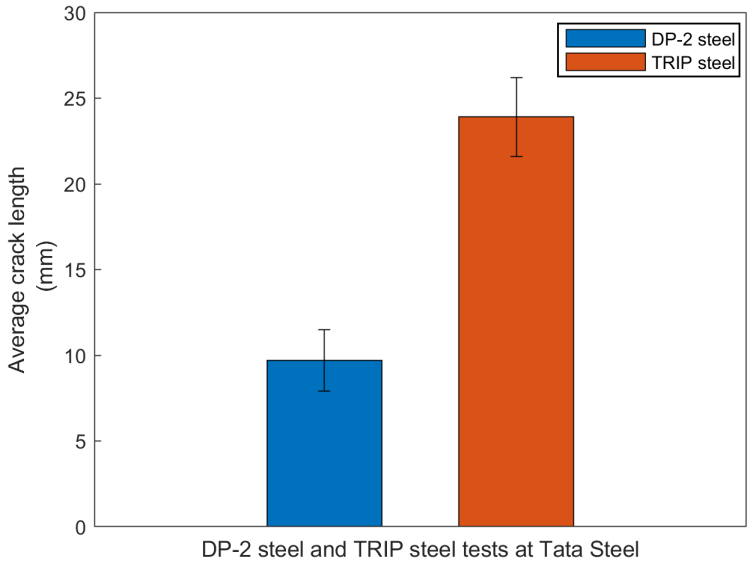

Figure 4.16: Average crack length in DP-2 steel tested with a laser beam spot diameter of 0.6 mm at industrial partner's LBW facility.

In Fig. 4.16, the average crack length for DP-2 steel and TRIP steel is plotted. The average crack length for DP-2 steel is 9.7 mm and the corresponding standard deviation is 1.8 mm. The average crack length for TRIP steel is 23.9 mm and the corresponding standard deviation is 2.3 mm. The cross section of the weld, perpendicular to the welding direction, prepared from the specimen of the above performed test for DP-2 steel and TRIP

steel is shown in Fig. 4.17, a and b, respectively, and the corresponding area of the fusion zone is 1.1 mm^2 and 1.2 mm^2, respectively.

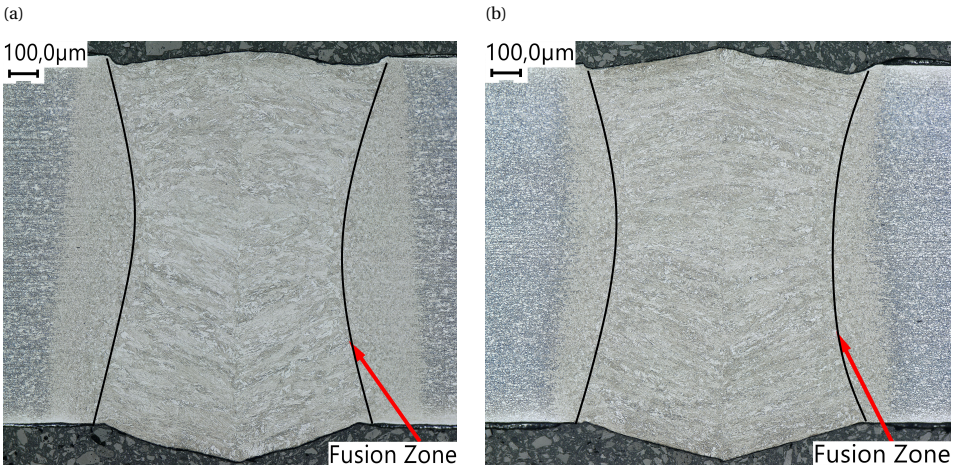

Figure 4.17: Cross section of the bead-on-plate weld for DP-2 steel in (a), and TRIP steel in (b), obtained with a laser beam spot diameter of 0.6 mm.

4.4 SUMMARY OF THE RESULTS

Hot cracking test results- In Table 4.1 and 4.2, the results of the VDEh standard hot cracking tests conducted with laser-1 at a spot size of 0.6 mm obtained using collimator lens and laser head movement are presented, respectively. Similarly in Table 4.3, the results of the tests conducted with laser-2 at a spot size of 0.6 mm are presented. Materials are ranked for their hot cracking susceptibility according to the resulting average crack length in a decreasing order. In Fig. 4.18, the resulting average crack lengths and the standard deviation of the three alloys used in this study from the VDEh standard hot cracking tests are plotted. From the results it can be observed that for the materials used in this study the hot cracking susceptibility ranking of the materials remains similar for both LBW facilities. However, variations in the resulting average crack lengths are found for the same materials tested at the two facilities for similar welding conditions. The standard deviation in DP-2 and TRIP steel tested with laser-1 is higher in comparison to the tests conducted with laser-2. For DP-1 steel tested at a welding speed of 167.0 mm/s with laser-1 at a spot diameter of 0.6 mm obtained using collimator lens movement and laser-2 (spot dia. 0.6 mm at focus), the resulting standard deviation is 2.9 mm and 2.4 mm, respectively. When DP-1 steel is tested with laser-2 at a welding speed of 156.7 mm/s the standard deviation is 4.1 mm. It can be observed that when the welding speed during testing of DP-1 steel with laser-2 is decreased the standard deviation increases significantly. In Fig. 4.19, the average crack length of the three alloys from the hot cracking tests is plotted against the area of the fusion zone. The data points correspond to the critical weld area in DP-1 steel and TRIP steel, and the weld areas in TRIP steel, DP-1 steel and DP-2 steel from Table 4.1 and 4.3. It can be observed that as the macroscopic area of the fusion zone increases, the average crack length also increases. In addition to this, when the observed area of the fusion zone remains approximately similar in the three alloys the sensitivity to solidification cracking turns out to be highest in TRIP steel, followed by DP-1 steel and DP-2 steel.

Table 4.1: Results of hot cracking tests conducted at Delft with a laser beam spot size of 0.6 mm obtained using collimator lens movement.

Ranking	Avg. crack length (mm)	Std. deviation (mm)	Max. crack length (mm)	Min. crack length (mm)	Weld area (mm^2)
TRIP steel	18.9	3.9	25.2	14.0	1.0
DP-1 steel	15.1	2.9	19.4	10.1	1.0
DP-2 steel	3.8	3.7	8.6	-	1.0

Table 4.2: Results of hot cracking tests conducted at Delft with a laser beam spot size of 0.6 mm obtained using laser head movement.

Ranking	Avg. crack length (mm)	Std. deviation (mm)	Max. crack length (mm)	Min. crack length (mm)	Weld area (mm^2)
TRIP steel	23.2	2.5	26.9	20.5	1.2
DP-1 steel	16.2	3.7	21.5	10.3	1.1
DP-2 steel	4.0	3.4	7.3	-	1.1

Table 4.3: Results of hot cracking tests conducted at Tata Steel with a laser beam spot size of 0.6 mm at focus.

Ranking		Avg. crack length (mm)	Std. deviation (mm)	Crack length (mm)		Weld area (mm^2)
				Max.	Min.	
DP-1 steel	TRIP steel	23.9	2.3	27.9	20.1	1.2
	Weld. speed: 167 mm/s	19.4	2.4	24.4	17.1	1.2
	Weld. speed: 156.7 mm/s	16.0	4.1	21.1	9.7	1.1
	DP-2 steel	9.7	1.8	12.5	7.0	1.1

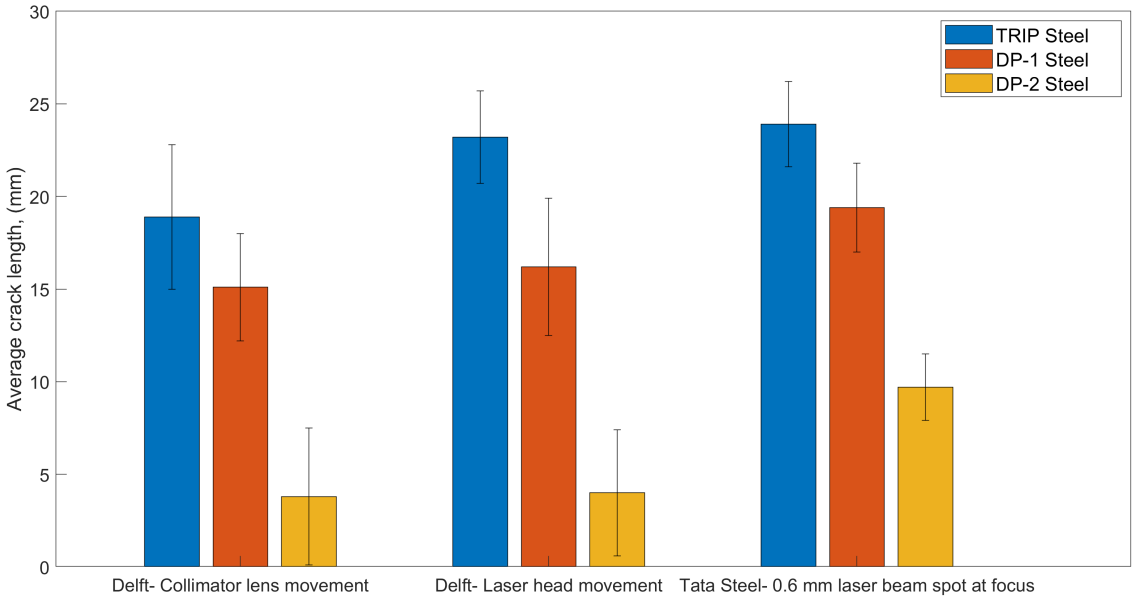

Figure 4.18: Summary of the results from the VDEh standard hot cracking test conducted on the three alloys used in this study.

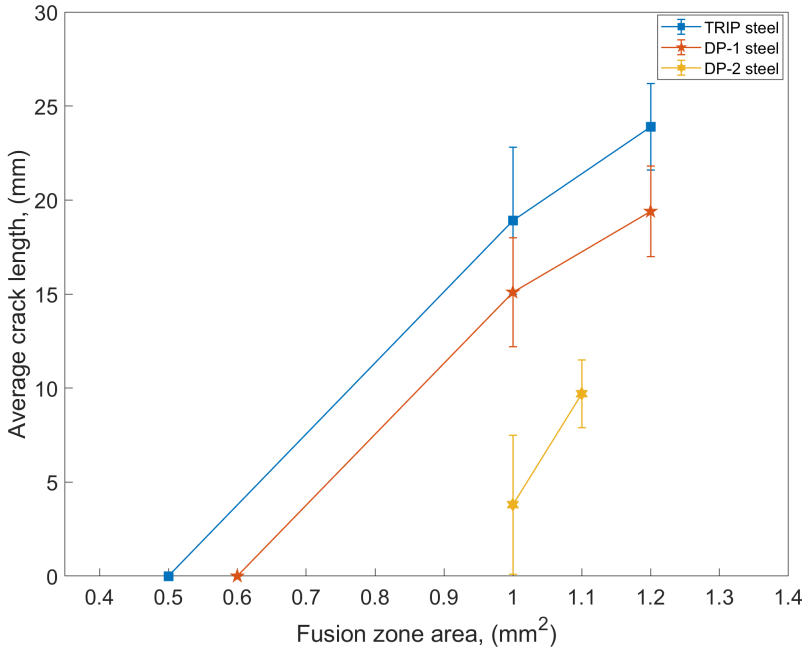

Figure 4.19: Average crack length of the three alloys used in this study plotted against the observed area of the fusion zone.

Shape of the fusion zone- From the cross sections of the specimens tested with laser-1, the shape of the fusion zone observed in the three alloys can be characterised as an hour glass shape. De-focusing of the laser beam to change the spot diameter and the welding speed, can be seen to affect the morphology of the hour glass shape of the fusion zone. For example, when the laser beam spot diameter is 0.2 mm the hour glass shape of the fusion zone is shown in Fig. 4.20, and has an approximately similar size at the top and bottom. Whereas, when the laser beam is de-focused to obtain a spot diameter of 0.6 mm, the hour glass shape of the fusion zone widens at the bottom in comparison to the top as observed in Fig. 4.4, 4.8 and 4.12, for DP-1, DP-2 and TRIP steel, respectively.

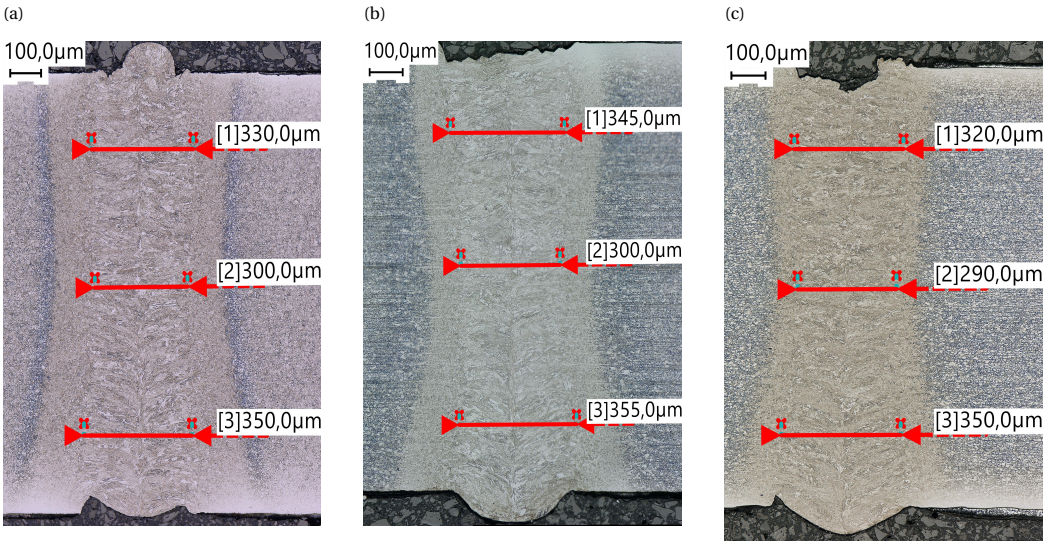

Figure 4.20: Size of the fusion zone in (a), DP-1 steel (b), DP-2 steel and (c), TRIP steel from tests conducted at Delft with a laser beam spot size of 0.2 mm.

From the cross section of the specimens tested with laser-2, the hourglass shape of the fusion zone is observed in DP-2 and TRIP steel as shown in Fig. 4.17, a and b, respectively. In DP-1 steel, when LBW is performed at a speed of 167.0 mm·s^{-1} the fusion line remains straight through the thickness of the plate as shown in Fig. 4.15 a. When the welding speed is reduced to 156.7 mm·s^{-1}, the shape of the fusion zone can be observed to shift towards the hourglass shape as shown in Fig. 4.15 b, which is identical to the shape observed in DP-1 steel tested with laser-1 but, inverted i.e., wider at the top than the bottom. Similarly, when the welding speed was reduced while performing bead-on-plate welding with laser-1 at a spot size of 0.2 mm on DP-2 steel, the hourglass shape of the fusion zone widened at the top in comparison to the bottom. The transverse cross section of DP-2 steel at a welding speed of 176.0 mm·s^{-1} and 167.0 mm·s^{-1} are shown in Fig. 4.21 a and b, respectively, while keeping the laser power (4 kW) and spot size (0.20 mm) constant.

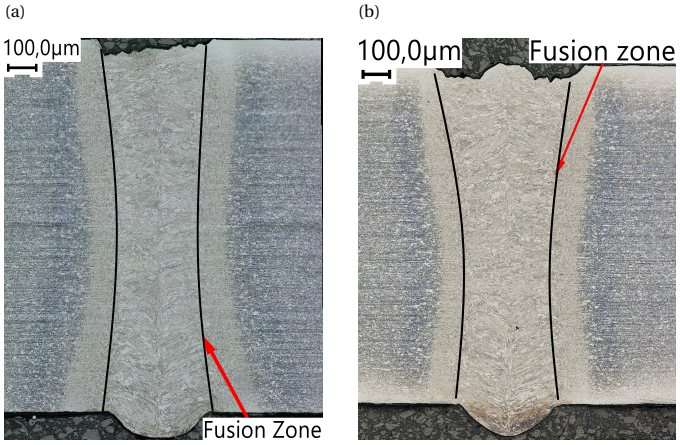

Figure 4.21: Cross section of the bead-on-plate weld perpendicular to the welding direction for DP-2 steel at a welding speed of 176.0 mm·s^{-1} in (a) and 167.0 mm·s^{-1} in (b).

The following observations can be deduced from the results presented in this Chapter which are discussed in Chapter 6:

- The resulting average crack lengths from tests conducted with laser-1 and laser-2 are different in the three alloys.
- When the area of the fusion zone is similar in the three alloys the susceptibility to solidification cracking is highest in TRIP steel, followed by DP-1 and DP-2 steel.
- Reducing the spot size of the laser beam below a critical value mitigates solidification cracking in alloys.
- As the welding speed is reduced, a minimum in the solidification cracking tendency is achieved, while keeping the spot size and laser power constant.
- The morphology of the hourglass shape of the fusion zone is affected by, de-focusing of the laser beam at constant welding speed and laser power, and welding speed at constant spot size and laser power.

5

EXPERIMENTAL AND NUMERICAL EVALUATION- WELD POOL SHAPE AND PROCESS EFFICIENCY

In this chapter, thermally validated finite element heat transfer models are used to determine the weld pool shape during laser welding. The numerically obtained weld pool shapes and size for materials used in this study are presented. Lastly, the validated model is used to determine the net process efficiency which is further compared with the existing model that can be used to calculate process efficiencies during laser welding.

5.1 INTRODUCTION

Generally, two types of weld pool shapes i.e., teardrop and elliptical, as described in section 2.1.3 and schematically shown in Fig. 2.4 are observed during welding. Thermo-physical properties, material composition and processing parameters are the determining factors for the shape of the weld pool during welding. For a given material, welding speed alone can have a significant influence on the resulting weld pool shape. The relationship between welding speed and the weld pool shape is such that as the welding speed increases the weld pool changes its shape from circular to elliptical and finally to a teardrop shape. Laser welding in automotive industry is performed at high welding speeds to maximise the production rate and limit the heat application to the material which reduces the extent of the resulting HAZ from welding. Therefore, it is likely that a teardrop shaped weld pool persists while performing welding at high speeds.

5.2 EXPERIMENTAL SETUP

Bead-on-plate laser welding experiments were performed using a 8 kW Nd:YAG laser on rectangular specimens (90×45 mm^2) prepared from DP-1 and TRIP steel sheets. The chemical composition of the steels used

is listed in Table 3.1. Welding parameters for the two materials used during the tests are listed in Table 5.1 and full penetration is obtained using these parameters. The thermal field during welding was measured using K-type thermocouples which were spot welded to the plate close to the fusion boundary at several positions.

Table 5.1: Laser beam welding parameters for DP-1 and TRIP steel during the experiments.

Material	Welding speed (mm/s)	Laser power (kW)	Spot size (mm)
DP-1	167.0	4	0.20, 0.40 and 0.60
TRIP	167.0	4	0.20, 0.25 and 0.60

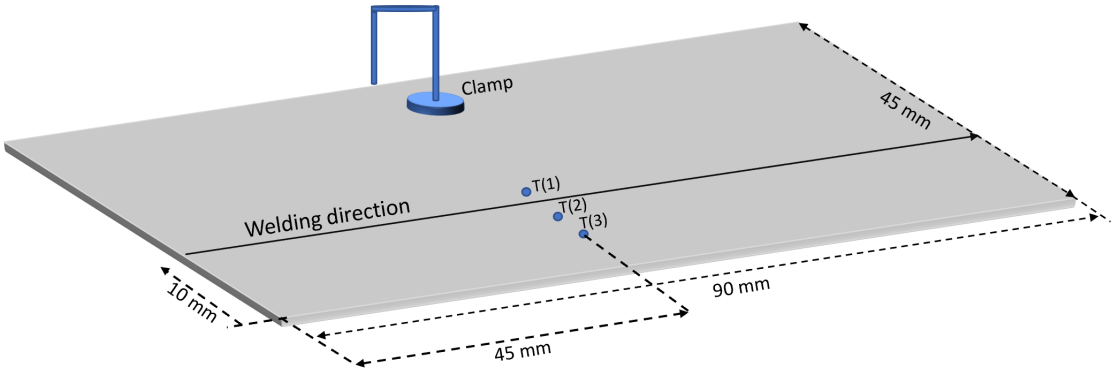

Figure 5.1: A schematic of the experimental setup for validating the finite element heat transfer model with positions of the thermocouples on the plate indicated as T(1), T(2) and T(3).

Welding is performed at a distance of 10 mm, parallel to the free edge. A schematic of the experimental setup is shown in Fig. 5.1. The positions of the thermocouples on the plate from the weld centreline are mentioned in Table 5.2 and 5.3, for DP-1 steel and TRIP steel, respectively.

Table 5.2: Thermocouple positions on the plate from the weld centreline in DP-1 steel.

Material	Spot diameter (mm)	Thermocouple distance from weld centreline (mm)		
		T(1)	T(2)	T(3)
DP-1 steel	0.20	0.8	0.9	1.9
	0.60	1.0	1.4	1.9

Table 5.3: Thermocouple positions on the plate from the weld centreline in TRIP steel.

Material	Spot diameter (mm)	Thermocouple distance from weld centreline (mm)		
		T(1)	T(2)	T(3)
TRIP steel	0.20	0.9	1.1	2.0
	0.60	0.7	1.8	2.3

5.3 RESULTS

5.3.1 TEMPERATURE CYCLE DURING LASER BEAM WELDING OF DP-1 STEEL AND TRIP STEEL

The experimental and numerical temperature cycles during LBW of DP-1 steel and TRIP steel are shown in Fig. 5.2 and 5.3, respectively. Good agreement can be observed between the experimental and numerical temperature cycles. In both alloys, the highest temperature is registered at thermocouple T(1), followed by T(2) and T(3). The peak temperatures at thermocouple locations T(1), T(2) and T(3), are higher when the laser beam spot diameter is 0.6 mm in comparison to 0.2 mm. However, the net heat input is considerably larger when the spot size is 0.6 mm in comparison to a spot spot size of 0.2 mm. Due to this, the cooling rates are expected to be higher when the spot size is 0.2 mm in comparison to a spot size of 0.6 mm. The experimental and numerical temperature gradients obtained between the thermocouple locations T(1), T(2) and, T(2), T(3) are mentioned in Table 5.4 and 5.5, for DP-1 and TRIP steel, respectively. The maximum difference in the experimental and numerical temperature gradients of DP-1 steel and TRIP steel is approximately 13 % and 7 %, respectively.

Table 5.4: Experimental and numerical temperature gradients between thermocouple locations T(1), T(2) and, T(2), T(3) in DP-1 steel.

Material	Spot diameter (mm)	Temperature gradient (°C/mm)			
		[T(1) - T(2)]		[T(2) - T(3)]	
		Exp.	Num.	Exp.	Num.
DP-1 steel	0.20	180	205	172	185
	0.60	283	288	196	202

Table 5.5: Experimental and numerical temperature gradients between thermocouple locations T(1), T(2) and, T(2), T(3) in TRIP steel.

Material	Spot diameter (mm)	Temperature gradient (°C/mm)			
		[T(1) - T(2)]		[T(2) - T(3)]	
		Exp.	Num.	Exp.	Num.
DP-1 steel	0.20	305	310	137	143
	0.60	294	315	68	72

(a) Thermocouple T(1)

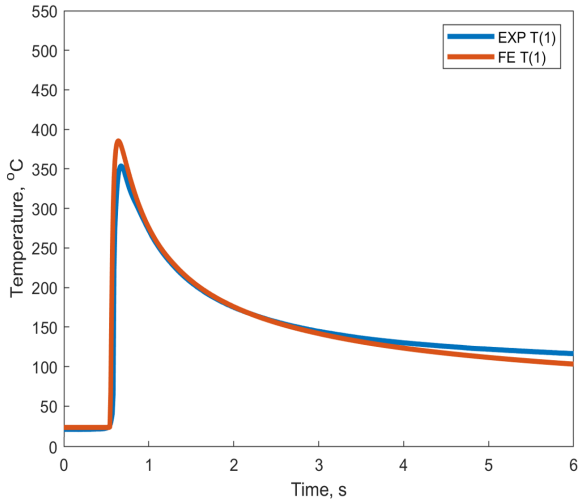

(d) Thermocouple T(1)

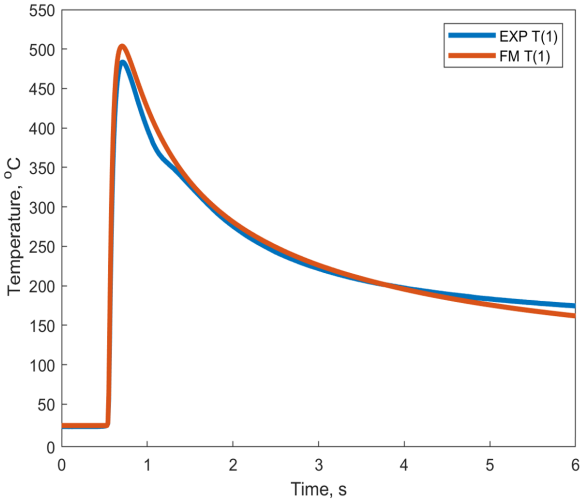

(b) Thermocouple T(2)

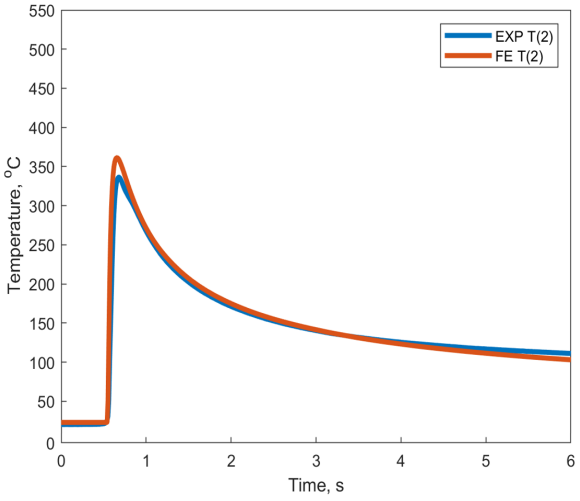

(e) Thermocouple T(2)

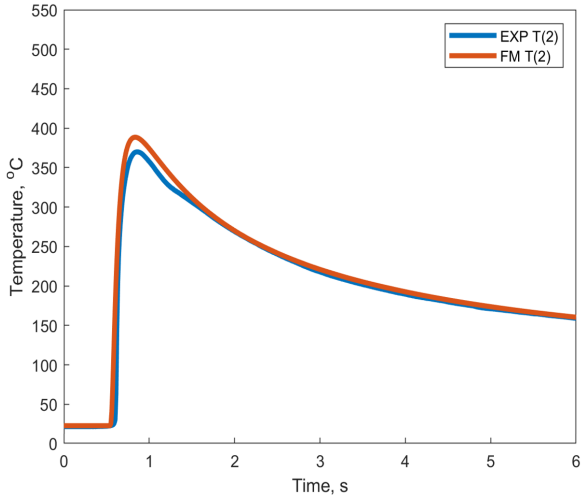

(c) Thermocouple T(3)

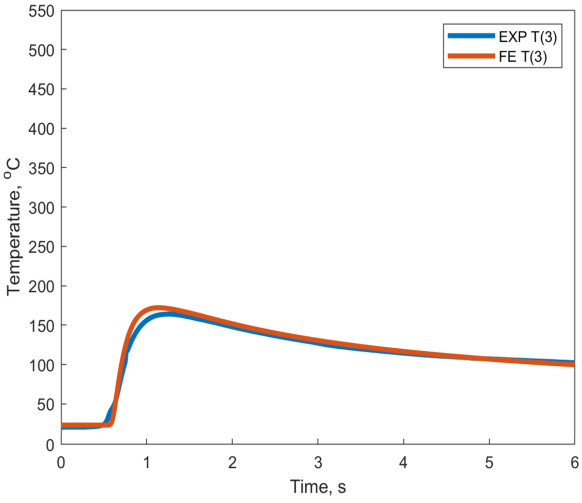

(f) Thermocouple T(3)

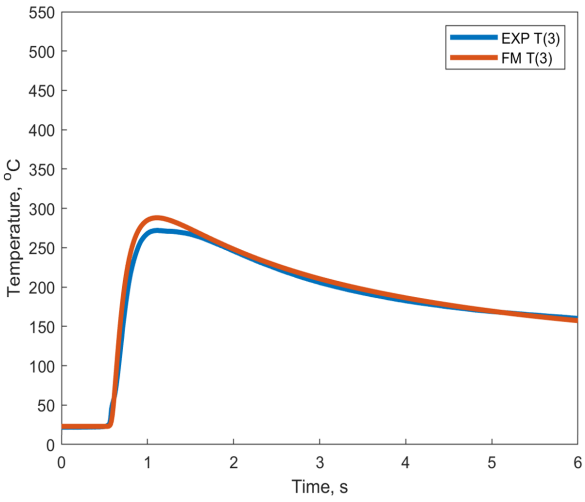

Figure 5.2: (a), (b) and (c) shows the experimental and numerical temperature cycle during LBW of DP-1 steel with a spot diameter of 0.2 for thermocouple positions T(1), T(2) and T(3), respectively. Whereas, (d), (e) and (f) shows the experimental and numerical temperature cycle obtained with a spot diameter of 0.6 mm for thermocouple positions T(1), T(2) and T(3), respectively.

(a) Thermocouple T(1)

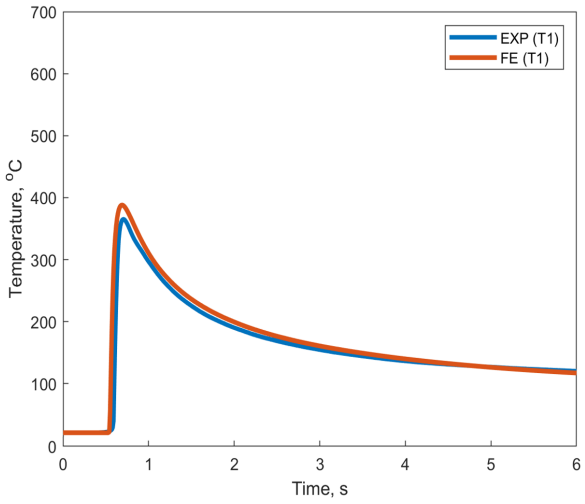

(d) Thermocouple T(1)

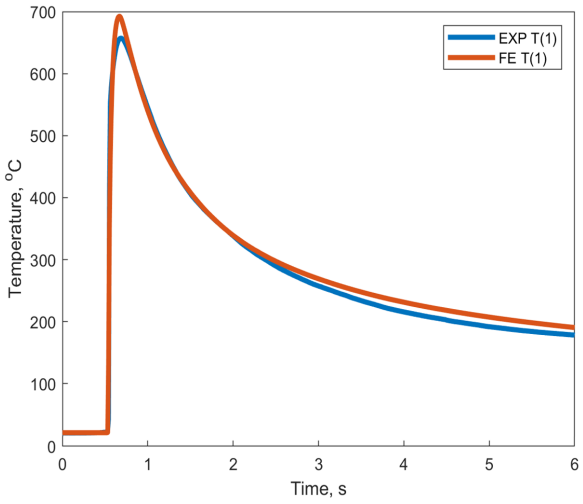

(b) Thermocouple T(2)

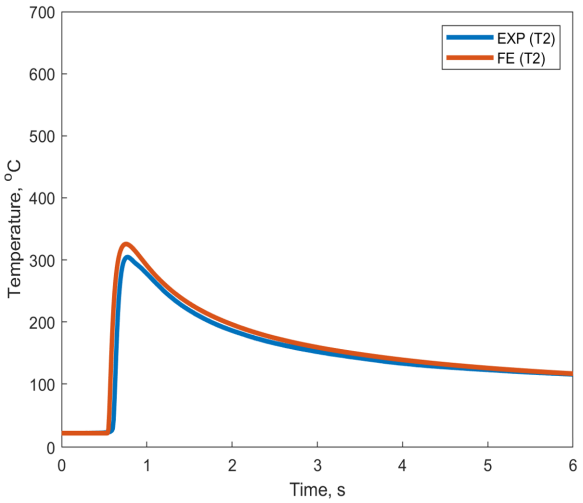

(e) Thermocouple T(2)

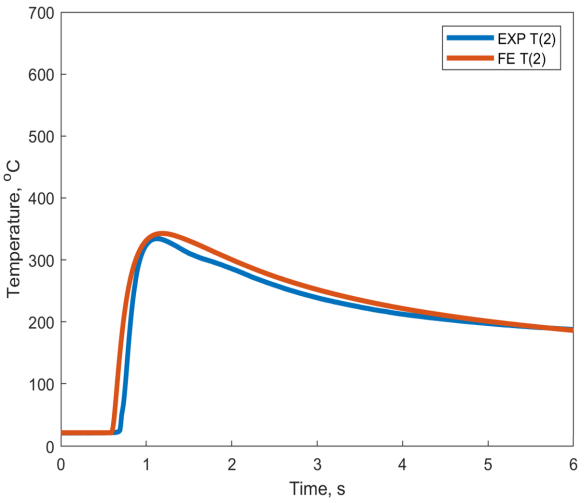

(c) Thermocouple T(3)

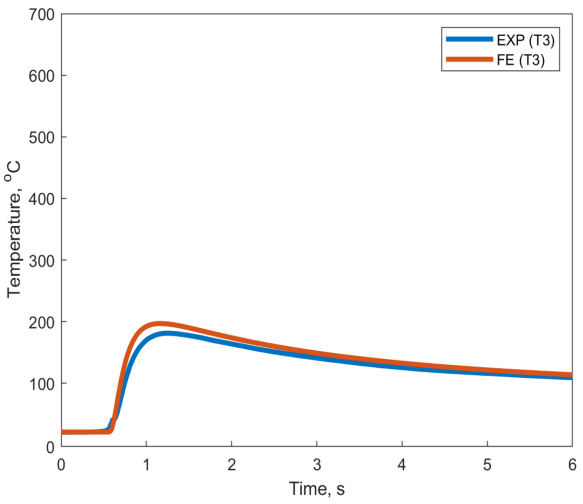

(f) Thermocouple T(3)

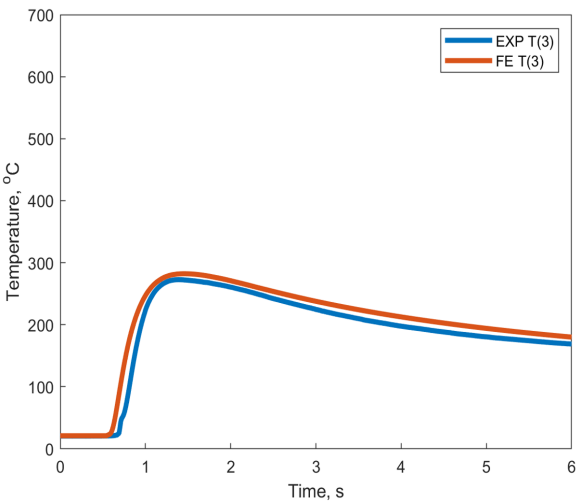

Figure 5.3: (a), (b) and (c) shows the experimental and numerical temperature cycle during LBW of TRIP steel with a spot diameter of 0.2 for thermocouple positions T(1), T(2) and T(3), respectively. Whereas, (d), (e) and (f) shows the experimental and numerical temperature cycle obtained with a spot diameter of 0.6 mm for thermocouple positions T(1), T(2) and T(3), respectively.

5.3.2 WELD POOL SHAPE AND MUSHY ZONE OF DP-1 STEEL

The numerically determined weld pool shape and the mushy zone during LBW with a spot diameter of 0.2 mm and 0.6 mm is shown in Fig. 5.4 a and b, respectively. The liquidus temperature for this steel is 1790 K and is used in the model to define the liquidus isotherm of the weld pool. The solidus temperature as determined from the Schiel solidification model is 1712 K. The mushy region of the weld pool is determined using these temperature values to define the liquidus and solidus isotherm. The weld pool shape and the mushy zone for the critical laser beam spot diameter of 0.4 mm, i.e., maximum spot size at which solidification cracking does not occur in DP-1 steel, is shown in Fig. 5.4 c. A teardrop shape of the weld pool is predicted for the

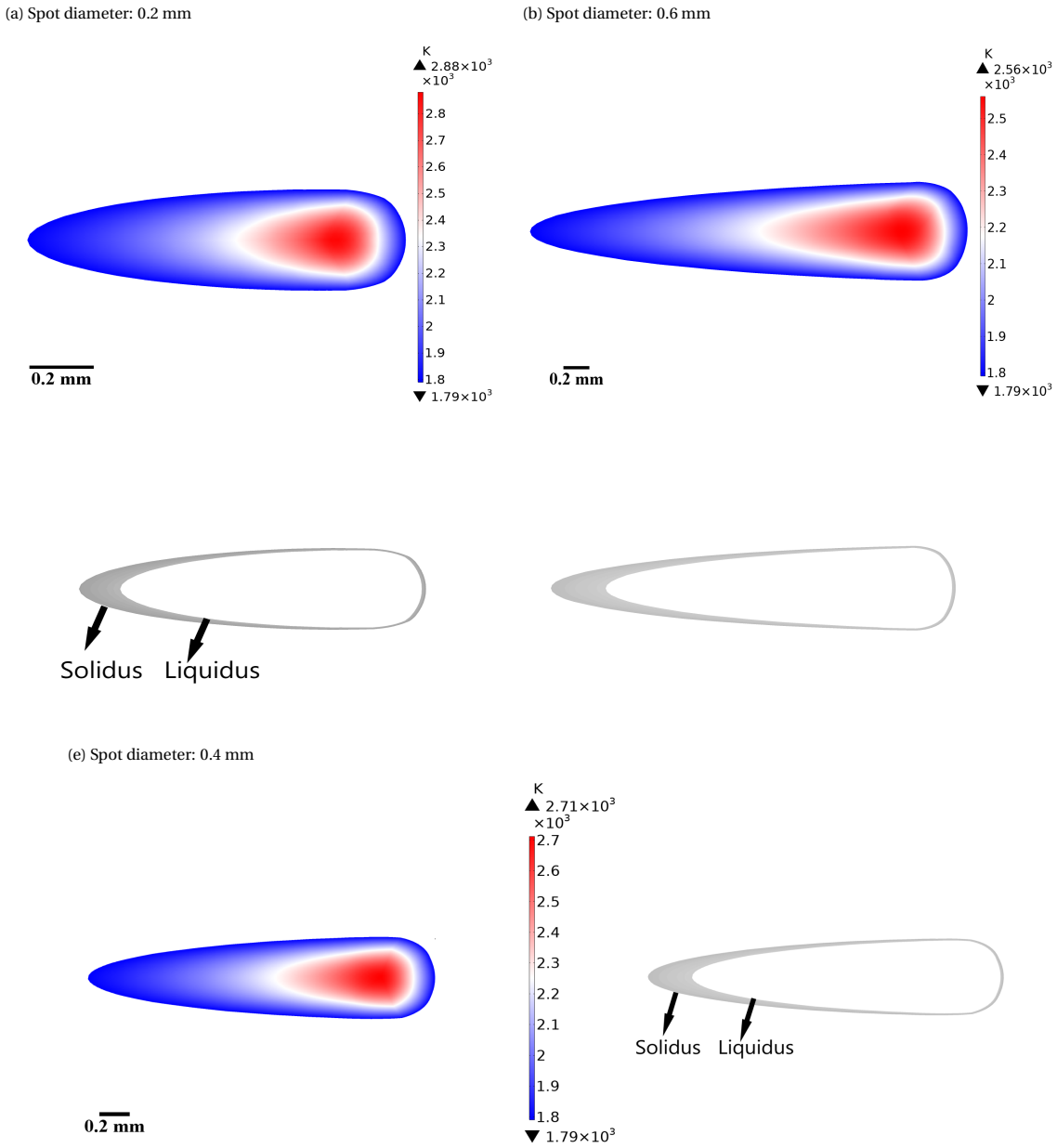

Figure 5.4: (a), (b) and (c) shows the numerically determined weld pool shape and mushy region of DP-1 steel for laser beam spot diameters of 0.2 mm, 0.6 mm and 0.4 mm, respectively.

three laser beam spot diameters. The size of the weld pool determined from the model and the size of the fusion zone observed from the bead-on-plate LBW experiments is listed in Table 5.6. An increase in the size

of the weld pool is observed as the laser beam spot diameter is increased, while keeping the laser power and welding speed constant. The length of the mushy zone is also determined from the model and is found to increase with increasing diameter of the laser beam, and weld pool length.

Table 5.6: Experimental and numerical size of the fusion zone and weld pool in DP-1 steel.

Material	Spot diameter (mm)	Width of fusion zone (mm)		Length of weld pool (mm)	Length of mushy zone (mm)
		Exp.	Num.	Num.	
DP-1 steel	0.20	0.30	0.40	1.20	0.10
	0.40	0.50	0.60	2.20	0.30
	0.60	0.70	0.80	3.40	0.50

5.3.3 WELD POOL SHAPE AND MUSHY ZONE OF TRIP STEEL

The numerically determined weld pool shape and the mushy zone during LBW with a spot diameter of 0.2 mm and 0.6 mm is shown in Fig. 5.5 and 5.6, respectively. The liquidus temperature for this steel is 1786 K and is used in the model to define the liquidus isotherm of the weld pool. The solidus temperature as determined from the Scheil solidification model is 1592 K. The mushy region of the weld pool is determined using these temperature values to define the liquidus and solidus isotherm. The weld pool shape and the mushy zone for the critical laser beam spot diameter of 0.25 mm, i.e., maximum spot size at which solidification cracking does not occur in TRIP steel, is shown in Fig. 5.7. A teardrop shape of the weld pool is predicted for the three laser beam spot diameters. The size of the weld pool determined from the model and the size of the fusion zone observed from the bead-on-plate LBW experiments is listed in Table 5.7. An increase in the size of the weld pool is observed as the laser beam spot diameter is increased while keeping the laser power and welding speed constant. The length of the mushy zone is also determined from the model and is found to increase with increasing diameter of the laser beam and weld pool length. The experimental and numerical width of the weld pool is relatively similar in DP-1 steel and TRIP steel for identical welding parameters namely, laser beam spot diameter, laser power and welding speed. However, at these identical welding parameters, the length of the weld pool and mushy zone is significantly larger in TRIP steel in comparison to DP-1 steel.

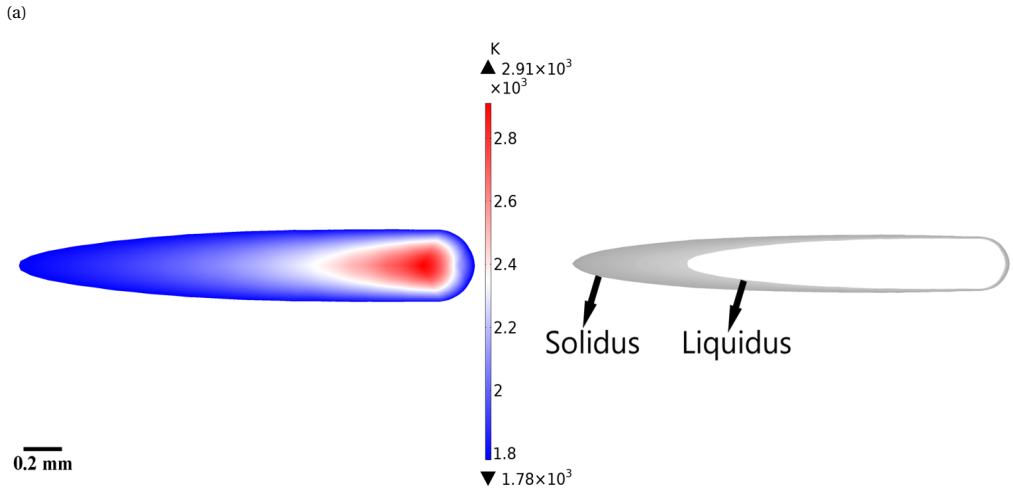

Figure 5.5: shows the numerically determined weld pool shape and mushy region of TRIP steel for a laser beam spot diameter of 0.2 mm.

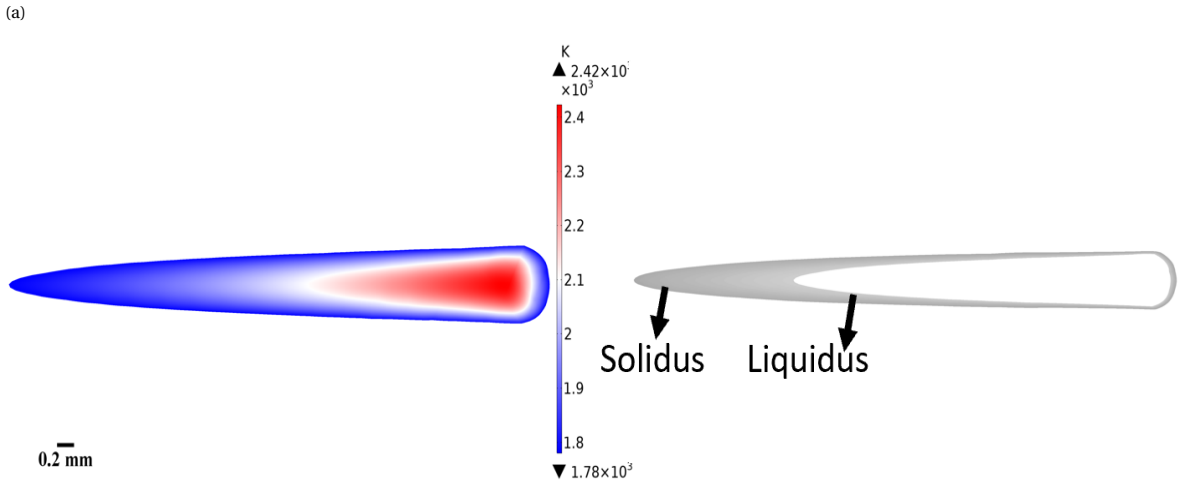

Figure 5.6: shows the numerically determined weld pool shape and mushy region of TRIP steel for a laser beam spot diameter of 0.6 mm.

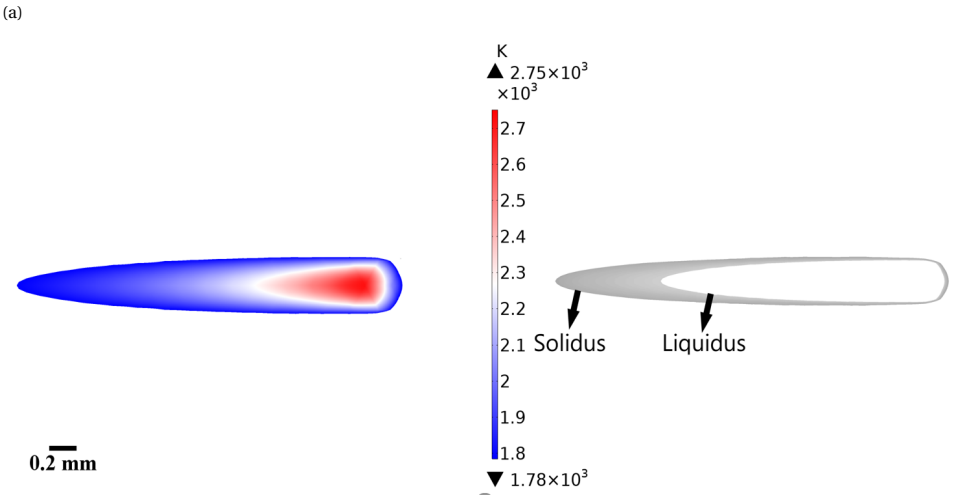

Figure 5.7: shows the numerically determined weld pool shape and mushy region in TRIP steel at a critical laser beam spot diameter of 0.25 mm.

Table 5.7: Experimental and numerical size of the fusion zone and weld pool in TRIP steel.

Material	Spot diameter (mm)	Width of fusion zone (mm)		Length of weld pool (mm)	Length of mushy zone (mm)
		Exp.	Num.	Num.	
TRIP steel	0.20	0.3	0.4	2.4	0.8
	0.25	0.4	0.5	2.8	1.0
	0.60	0.7	0.8	6.1	2.6

5.3.4 EFFICIENCY OF THE LASER BEAM WELDING PROCESS

The efficiency of the LBW process was plugged in the thermal models as a fitting factor to obtain a reasonable agreement between the experimental and numerical temperature cycles, and the size of the weld pool

(fusion zone). The numerical process efficiency used in the models to obtain the previously described temperature cycles and weld pool characteristics (size, shape and mushy region) in DP-1 steel and TRIP steel are plotted in Fig. 5.8, a and b, respectively. The analytically calculated process efficiency using Equation 3.7, for different laser beam spot diameters are also plotted in these figures. Specific Energy (SE) values of 120.0 J·mm^{-2} and 40.0 J·mm^{-2}, in DP-1 and TRIP steel, correspond to laser beam spot diameters of 0.20 mm and 0.60 mm, respectively. Whereas, SE values of 60.0 J·mm^{-2} and 96.0 J·mm^{-2} correspond to the experimentally determined critical laser beam spot diameters of 0.40 mm and 0.25 mm, in DP-1 steel and TRIP steel, respectively. The experimental data points for laser beam spot diameters of 0.60 mm correspond to the efficiency values calculated with cross sectional areas of the welds obtained with laser-1 and laser-2. Whereas, data points at spot diameters of 0.20, 0.25, and 0.40 are only for cross sectional areas of the welds obtained with laser-1. The numerical data points of the efficiency values for all laser beam spot diameters also correspond to bead-on-plate welds made using laser-1. From the efficiency plots of DP-1 steel and TRIP steel, it can be observed that the LBW process efficiency increases with increasing spot size of the laser beam. This is true for both numerical and analytical calculation of the process efficiency. The process efficiency at laser beam spot diameter of 0.6 mm using laser-2 is significantly overestimated when determined analytically. For laser-1, the process efficiency values at this spot size drop below the values of laser-2 but still remain higher than the numerically obtained values. A reasonable agreement exists between the analytical and numerical values of the process efficiency for the remaining laser beam spot diameters. For the critical laser beam spot diameters in DP-1 Steel and TRIP steel, the corresponding process efficiencies are listed in Table 5.8. The critical process efficiency can be interpreted as the critical heat input during LBW above which solidification cracking occurs and is higher for DP-1 steel in comparison to TRIP steel.

Table 5.8: Numerical and analytical critical process efficiency of LBW in DP-1 steel and TRIP steel.

Material	Spot diameter (mm)	Process efficiency, η (%)	
		Analytical	Numerical
DP-1 steel	0.40	53	60
TRIP steel	0.25	41	44

5.3.5 SUMMARY OF THE RESULTS

Table 5.9: Numerically determined weld pool shape and size, the mushy zone size and the efficiency of the laser welding process in DP-1 steel for variable diameters of the laser beam spot.

Spot dia. (mm)	Weld pool length (mm)	Weld pool width (mm)	Mushy zone length (mm)	Weld pool shape	Efficiency (η)
0.2	1.2	0.4	0.1	Teardrop	0.44
0.4	2.2	0.6	0.3	Teardrop	0.60
0.6	3.4	0.8	0.5	Teardrop	0.77

In Table 5.9 and 5.10, the size of the weld pool, mushy zone and the process efficiency during LBW of DP-1 steel and TRIP steel are listed, respectively. The following observations can be deduced from the results presented in this Chapter which are discussed in Chapter 6:

- From the temperature cycles of DP-1 steel and TRIP steel, in general, higher peak temperatures are

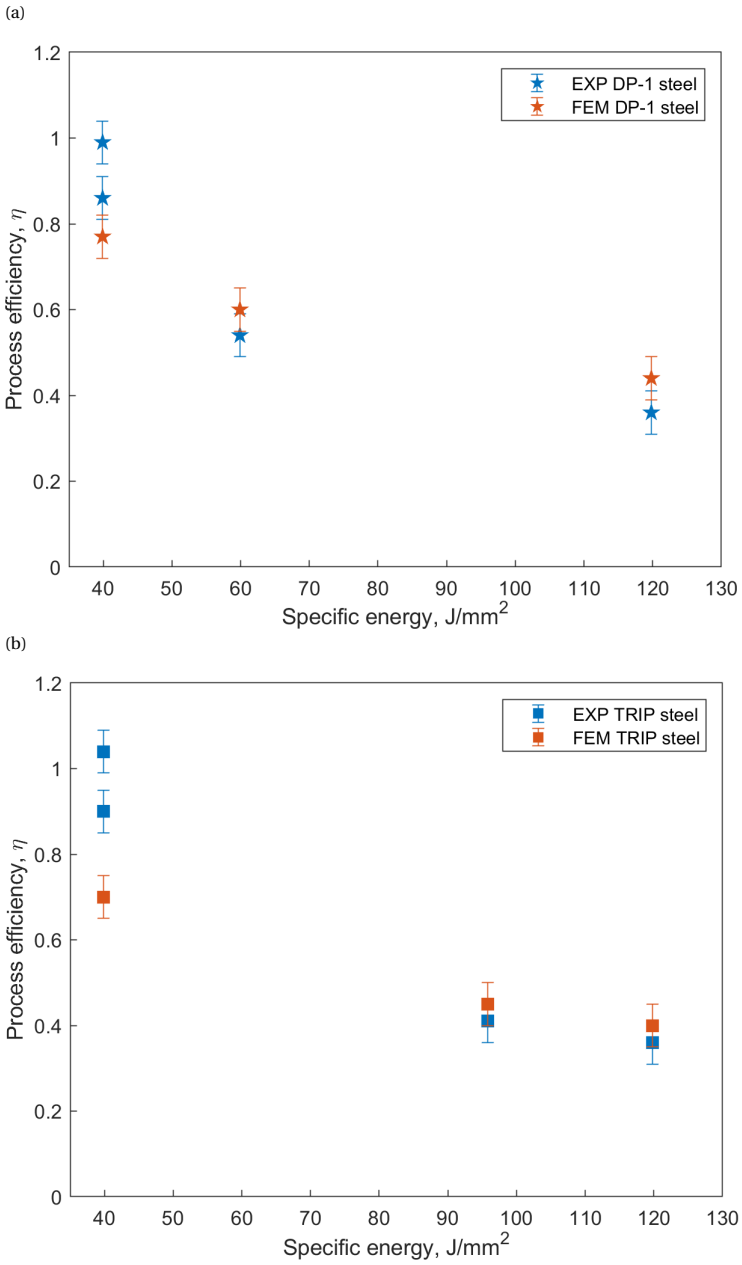

Figure 5.8: Analytical and numerical process efficiencies during bead-on-plate LBW of DP-1 steel in (a) and TRIP steel in (b).

Table 5.10: Numerically determined weld pool shape and size, the mushy zone size and the efficiency of the laser welding process in TRIP steel for variable diameters of the laser beam spot.

Spot dia. (mm)	Weld pool length (mm)	Weld pool width (mm)	Mushy zone length (mm)	Weld pool shape	Efficiency (η)
0.20	2.4	0.4	0.8	Teardrop	0.40
0.25	2.8	0.5	1.0	Teardrop	0.45
0.60	6.1	0.8	2.6	Teardrop	0.70

experienced at thermocouple locations T(1), T(2) and T(3) in both alloys when the laser beam spot diameter is 0.6 mm in comparison to a spot diameter of 0.2 mm.

- The shape of the weld pool is insensitive to changes in laser beam spot diameter, while maintaining the

welding speed and laser power constant, as the thermal models predict a teardrop shape of the weld pool for different spot diameters.

- The length of the weld pool is found to increase with increasing laser beam spot diameters. This is also true for the length of the mushy region in the weld pool.
- When the laser power, welding speed and laser beam spot diameter are similar during LBW of DP-1 steel and TRIP steel, the numerical and experimental width of the weld pool and fusion zone, respectively, is relatively similar in both alloys. However, the predicted length of the weld pool is considerably larger in TRIP steel in comparison to DP-1 steel. This is also true for the length of the mushy region in TRIP steel.
- The process efficiency during LBW of DP-1 steel and TRIP steel increases as the laser beam spot diameter increases. Also, during LBW of DP-1 steel and TRIP steel with similar welding parameters (power, speed and spot diameter), the process efficiency for DP-1 steel is higher than TRIP steel.
- The critical process efficiency or the critical heat input above which solidification cracking occurs, is higher in DP-1 steel in comparison to TRIP steel.

6

DISCUSSION

In this chapter, the results of the standard hot cracking tests are discussed for the materials used in the study. The variations in the results are explained using microstructural observations. Effect of welding speed, laser beam spot diameter and laser beam de-focusing on solidification cracking is also discussed. This is followed by a discussion on the analytically and numerically derived laser beam welding process efficiency and weld pool characteristics.

6.1 VARIATIONS IN MEASURED AVERAGE CRACK LENGTHS

The resulting average crack length for DP-1 steel obtained from tests conducted with laser-1 (Delft) and laser-2 (Tata Steel) is 15.1 mm and 19.4 mm, respectively. The welding parameters during these tests, namely, the welding speed, laser power and laser beam spot size are kept constant for both facilities. But, the keyhole configuration that prevails during these tests is different. As discussed in Section 2.1.1, full penetration LBW can be carried out in two modes or configurations; closed keyhole configuration and open keyhole configuration. Closed keyhole mode welding is possible in a narrow range of process parameters and is sensitive to disturbances (such as variations in the energy transfer, shielding conditions, mechanical vibrations). Shielding conditions are affected due to the fumes that are generated during the LBW process. Mechanical vibrations are inherent due to dynamic movements during the process. Variations in energy transfer can occur due to differences in the spatial intensity distribution and quality of the laser beam, as the interaction of the laser beam with the material is affected by these factors. The spatial intensity distribution of the two lasers used for the tests was measured at a spot size of 0.6 mm and is presented in Chapter 3, Fig 3.6 a and c, for laser-1 and laser-2, respectively. Laser-1 has a top-hat distribution and a higher beam quality (low divergence) whereas, laser-2 has a Gaussian distribution and a lower beam quality (high divergence). Due to the above stated variations during LBW, the closed keyhole configuration can easily switch to the open keyhole configuration. A random occurrence of open/closed keyhole mode welding, and sometimes lack of full penetration can also be observed due to the highly sensitive nature of the closed keyhole mode welding [16]. While conducting hot cracking tests with laser-1, it was observed that the keyhole existed more towards open keyhole configuration

between the tests, and sometimes random oscillations between open and closed keyhole mode occurred in the same test. The open keyhole configuration during the test was verified from longitudinal cross sections of the welds prepared parallel to the welding direction. The lower average crack length for DP-1 steel tested with laser-1 is a result of the keyhole existing more towards the open keyhole configuration during these tests, as shown in Fig. 6.1. The response of DP-1 steel to the etchant is such that the morphology of the fusion line can be observed as it appears blue coloured in Fig. 6.1. The fusion line remains nearly straight through the thickness of the plate which is indicative of the keyhole remaining open at the bottom surface of the plate. As described in Section 2.1.1, in the open keyhole configuration the laser beam can escape from the bottom and the top openings of the keyhole after being reflected off the keyhole walls, which increases the energy losses from the plate [15] [16] [79]. Due to this, the resulting size of the weld (fusion zone) is reduced, which decreases the tendency of solute segregation and the extent of thermal stresses/strains imposed on the solidifying microstructure. Therefore, the susceptibility of DP-1 steel to solidification cracking is reduced in this case.

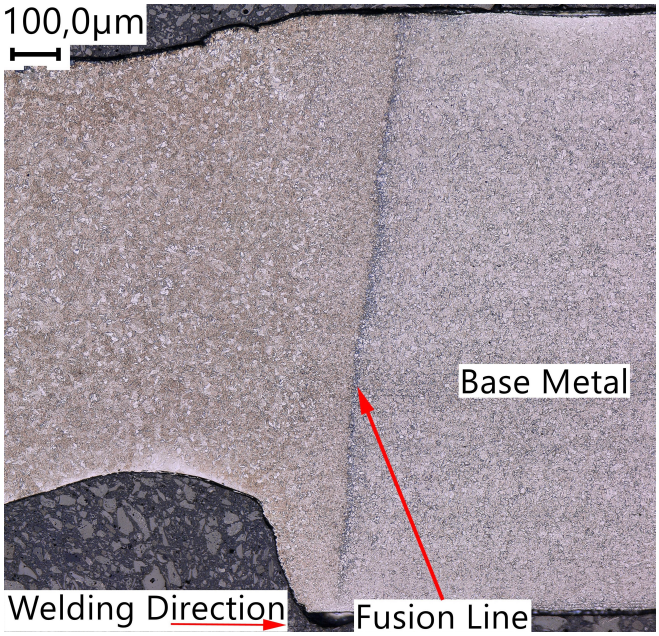

Figure 6.1: Longitudinal cross section of the weld parallel to the welding direction describing the open-keyhole configuration.

In the case of hot cracking tests conducted with laser-2, the higher average crack length at similar welding conditions arises from the existence of the keyhole in the closed keyhole configuration during LBW. The longitudinal cross section of the weld parallel to the welding direction is shown in Fig. 6.2. In this case, the fusion line (coloured blue) curves towards the bottom surface of the plate, in the thickness direction, indicating that the keyhole is closed at the bottom. Due to closing of the keyhole at the bottom surface of the plate, the laser beam and the vaporised metal can only escape from the top aperture which results in a longer beam path in the keyhole and higher energy absorption in comparison to the open keyhole mode [15] [16]. The higher energy absorption is a result of multiple reflection and absorption of the laser beam at the keyhole walls as schematically shown in Fig. 2.2 b, and described in Section 2.1.1. The end result of the welds made in the closed keyhole configuration is that the increased energy absorption by the plate translates to an increase in the total melt volume or a larger size of the weld (fusion zone). This in turn is likely to increase the extent of solute segregation and the stress/strain build-up in the solidifying microstructure which leads to an increased cracking tendency of DP-1 steel.

Size of the fusion zone- The fusion zone size in DP-1 steel from tests conducted with laser-1 and laser-2 are shown in Fig. 6.3 a and b, respectively. Due to the closed keyhole configuration in tests conducted with

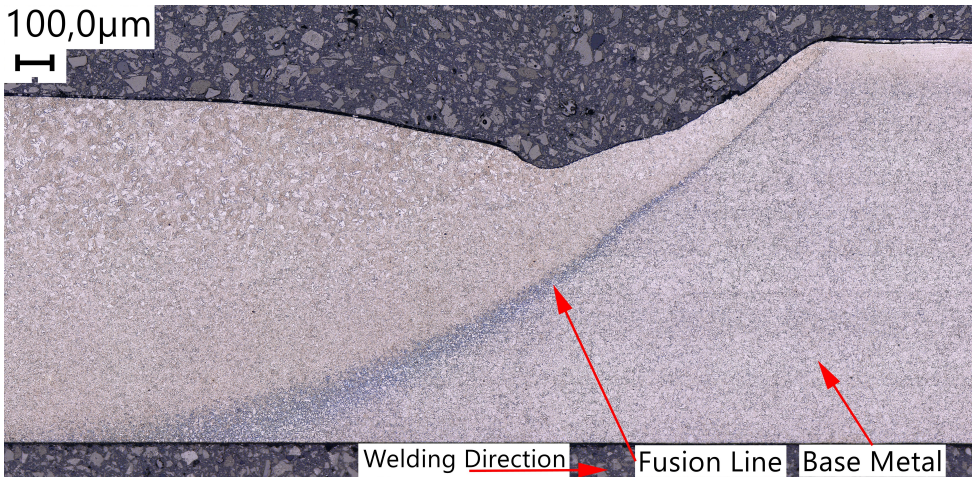

Figure 6.2: Longitudinal cross section of the weld parallel to the welding direction describing the closed keyhole configuration.

laser-2, the size of the fusion zone is larger and the resulting bead-on-plate welds have approximately 15-20 % greater melt volume in comparison to the bead-on-plate welds made using laser-1. This increase in melt volume affects the thermal-mechanical and metallurgical conditions of the solidifying structure, resulting in a higher average crack length from the tests.

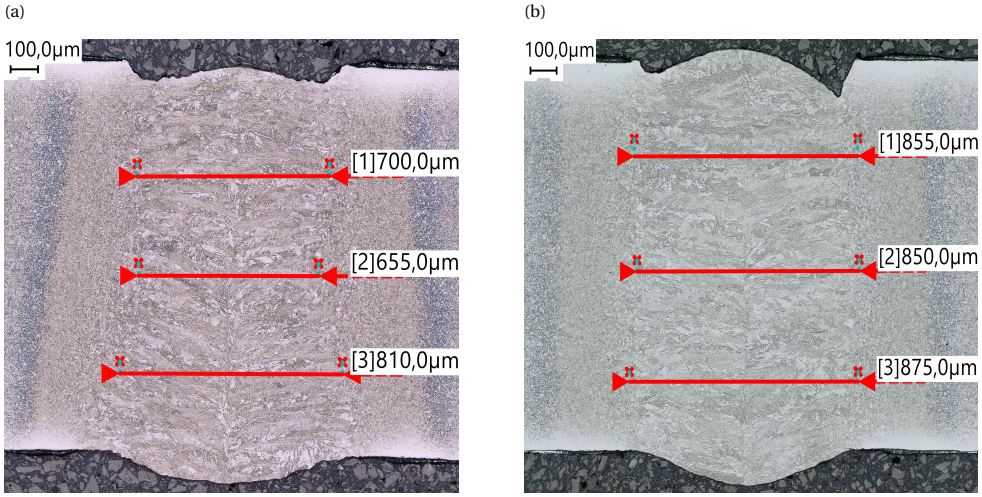

Figure 6.3: Size of the fusion zone in DP-1 steel from tests conducted with laser-1 in (a) and laser-2 in (b).

6.2 EFFECT OF LASER BEAM SPOT SIZE AND WELDING SPEED

Decreasing the spot size of the laser beam, while keeping power and welding speed constant, results in an increased power density of the laser beam. In this manner, the resulting keyhole can exist in an open configuration and energy losses from the bottom opening of the keyhole are enhanced. The open configuration of the keyhole was verified from the longitudinal cross section of the weld, (parallel to the welding direction) as shown in Fig. 6.4, where the straight morphology of the fusion line (blue coloured) can be observed and is

indicative of an open-keyhole configuration.

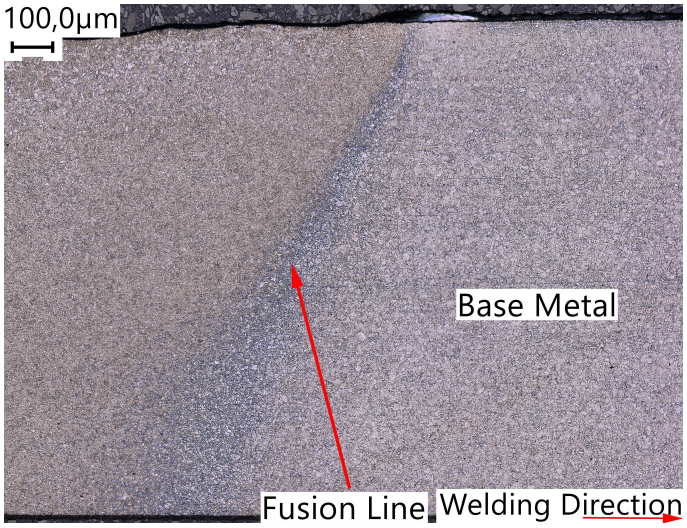

Figure 6.4: Longitudinal cross section of the weld parallel to the welding direction describing the open keyhole configuration obtained with a laser beam spot size of 0.2 mm.

For the the three materials used in the study, a laser beam spot size of 0.2 mm was used to perform bead-on-plate welds and solidification cracking was not observed in the three alloys. Cross sections of the welds perpendicular to the welding directions for a spot size of 0.2 mm are shown in Fig. 4.20, for DP-1, DP-2 and TRIP steel, respectively. It is interesting to note that regardless of the composition and thermo-physical properties of the alloys, the size of the fusion zone for the three alloys is relatively similar and solidification cracking was not observed. The pronounced effect of the open keyhole configuration, resulting in high energy losses, dominates over the composition of the alloys thereby, decreasing the solidification cracking tendency of the alloys drastically. Additionally, the spot size was increased from 0.2 mm to determine the maximum or the critical spot size at which solidification cracking occurs in DP-1 steel and TRIP steel, while maintaining the laser power and welding speed constant. A critical spot size of 0.40 mm and 0.25 mm was experimentally determined for DP-1 steel and TRIP steel, respectively, and the keyhole remained in the open keyhole configuration. The effect of spot size on solidification cracking is schematically described in Fig. 6.5.

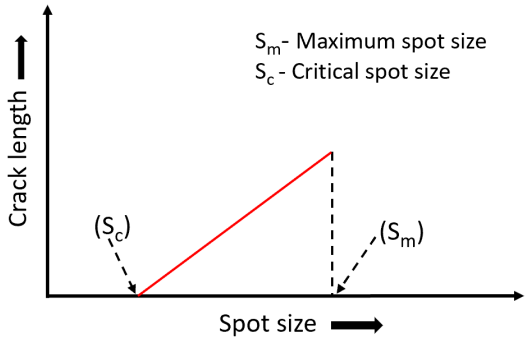

Figure 6.5: A schematic showing the effect of changing the spot size on the solidification cracking tendency at constant welding speed and laser power.

When the spot size is decreased from the maximum spot size (S_m), which defines the upper limit of the spot size to achieve complete penetration at constant welding speed and laser power, the solidification cracking

tendency (crack length) starts to decrease. This is due to the increasing power density with decreasing spot size, which enforces the open keyhole configuration welding. Once the critical spot size (S_c) is achieved, solidification cracking does not not occur. The magnitude of this critical spot size, is influenced by the susceptibility of an alloy to solidification cracking. This in turn is dependent on the metallurgy of an alloy, and is higher for alloys with relatively low susceptibility (DP-1 steel) in comparison to alloys with high susceptibility (TRIP steel).

Effect of welding speed- The keyhole can be shifted to the open keyhole configuration from the closed keyhole configuration by reducing the welding speed, while maintaining the power and spot size of the laser beam constant. The extent of the reduction in welding speed determines whether the keyhole shifts completely to the open keyhole configuration or the random open/closed keyhole configuration from the closed keyhole configuration. For example, on slight reduction of the welding speed the closed keyhole configuration shifts to the random open/closed configuration before completely shifting to the open keyhole configuration on further reduction of the welding speed, The average crack length for DP-1 steel from tests conducted with laser-2 at a welding speed of 167 mm·s^{-1} and 156.7 mm·s^{-1} is 19.4 mm and 16.0 mm, respectively. The nominal heat input increases from 24.9 J·mm^{-1} to 25.5 J·mm^{-1} when the welding speed is decreased. The increased heat input shifts the closed keyhole configuration towards the open keyhole configuration or a randomly occurring open/closed keyhole configuration, which causes energy losses from the bottom opening of the keyhole. This was verified from the observed reduced size of the weld (fusion zone) while decreasing the welding speed from 167 mm·s^{-1}, as shown in Fig 6.6 a, to 156.7 mm·s^{-1}, as shown in Fig 6.6 b.

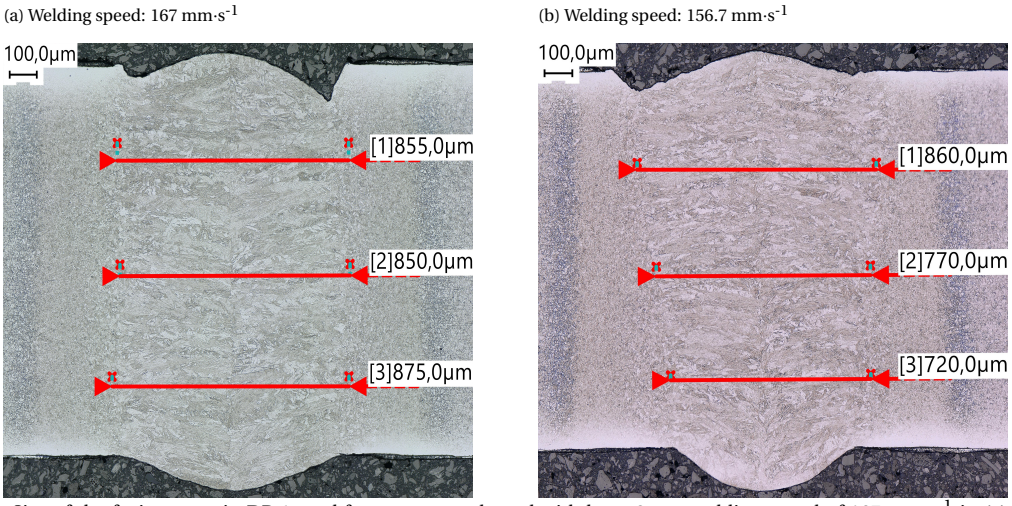

Figure 6.6: Size of the fusion zone in DP-1 steel from tests conducted with laser-2 at a welding speed of 167 mm·s^{-1} in (a) and 156.7 mm·s^{-1} in (b).

The effect of welding speed on solidification cracking tendency is schematically described in Fig. 6.7, in which three regions can be identified namely, region (1), (2) and (3). For constant laser power and spot size, consider three arbitrary values for the welding speed, (a), (b) and (c) such that region (1), (2) and (3) is attained, respectively. Starting from welding speed (c) in region 3, as the welding speed is reduced to attain region (2), the keyhole starts to shift towards the random open/closed keyhole configuration (decreasing crack length), and finally to the open keyhole configuration from the closed keyhole configuration at welding speed (c). The shift in the keyhole configuration arises due to the increased heat input, while reducing the welding speed from (c) towards (b). At a welding speed of (b), in region (2), a balance exists between the imposed

thermo-mechanical load from welding, and the energy losses resulting from the open keyhole configuration. Corresponding to this, the minimum solidification cracking tendency (crack length) is achieved. When the welding speed is further reduced from (b) towards (a), such that region (1) is attained, the energy losses due to the open keyhole configuration can no longer compensate for the increased thermo-mechanical due to the increased heat input from reducing the welding speed. Therefore, moving from region (2), to region (1) and (3), increases the solidification cracking tendency of an alloy. This is due to the increased thermo-mechanical load arising from reducing the welding speed in region 1, and shifting of the keyhole to the closed keyhole configuration in region 3, in comparison to region 2.

Reducing the laser beam spot size and welding speed, increases the power density of the laser beam and the

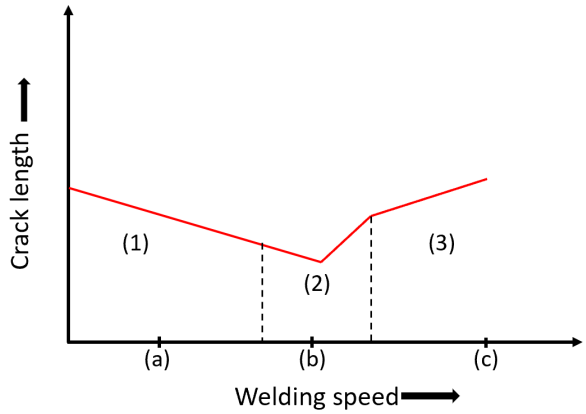

Figure 6.7: A schematic showing the effect of changing the welding speed on the solidification cracking tendency at constant welding speed and laser power.

nominal heat input, respectively, which facilitates welding in the open keyhole configuration. This results in a reduced size of the fusion zone which is likely to decrease the extent of solute segregation and the stress/strain build-up in the solidifying microstructure, leading to a lower solidification cracking tendency of an alloy. However, decreasing the welding speed to decrease the solidification cracking susceptibility of an alloy can only be utilised until the reduced welding speed, at constant power and laser beam spot diameter, does not result in a less advantageous thermo-mechanical load [80].

Standard deviation of the tests- In general, a higher standard deviation is observed in hot cracking tests conducted with laser-1 when compared to laser-2. The free edge distance was controlled (3.0 mm) for each test by measuring the size of the plate prior to clamping and suitably adjusting the position of the clamping setup. It was previously mentioned that for the tests with laser-1 the keyhole existed more towards the open keyhole configuration or a randomly occurring open/closed keyhole configuration. Whereas with laser-2, the closed keyhole configuration was prevalent during the tests, apart from testing of DP-1 steel at a speed of 156.7 mm·s^{-1}. The decreased welding speed shifted the closed keyhole configuration in DP-1 steel at welding speed of 167.0 mm·s^{-1} with laser-2 to the open keyhole or the random open/closed keyhole configuration. Consequently, the standard deviation in the tests of DP-1 steel at a welding speed of 156.7 mm·s^{-1} was also increased. This can be attributed to the instability in the keyhole behaviour which results in the open or random open/closed keyhole configuration, thereby, affecting the solidification crack length, which in turn impacts the range and the standard deviation of tests.

6.3 EFFECT OF DE-FOCUSING MANNER

As explained in Section 2.1.2, de-focusing of the laser beam can be achieved by movement of the collimator lens or the laser head to achieve the desired spot size of the laser beam (Fig. 2.3 in Chapter2). In the first case, i.e. 0.6 mm spot size with collimator lens movement, the average crack length for DP-1, DP-2 and TRIP steel from tests conducted with laser-1 is 15.1 mm, 3.8 mm and 18.9 mm, respectively. In the second case, i.e. 0.6 mm spot size with laser head movement, the average crack length for the three steels from tests is 16.2 mm, 4.0 mm and 23.2 mm, respectively. When the laser beam is de-focused, the plane of the laser beam at which the spot size is 0.6 mm is not the same for the two cases. Due to this, the spatial intensity distribution of the laser beam is different for the two cases which affects the laser beam interaction with the workpiece and the corresponding energy absorption. The higher average crack lengths in the second case can be attributed to the increase in the size of the fusion zone of the three steels in comparison to the first case, which is most likely the result of the different spatial intensity distribution of the laser beam for the two cases.

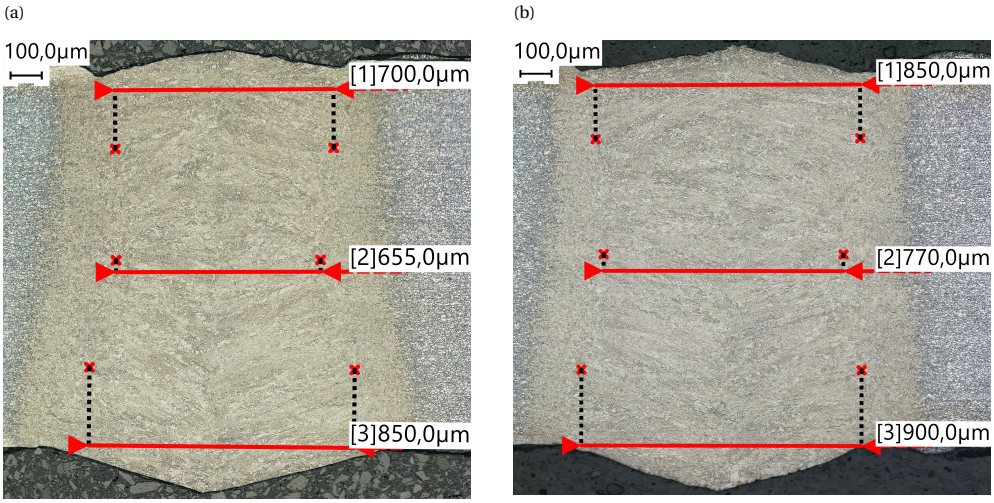

Figure 6.8: Size of the fusion zone in TRIP steel from tests conducted with laser-1 at a laser beam spot size of 0.6 mm obtained using collimator lens movement in (a), and laser head movement in (b).

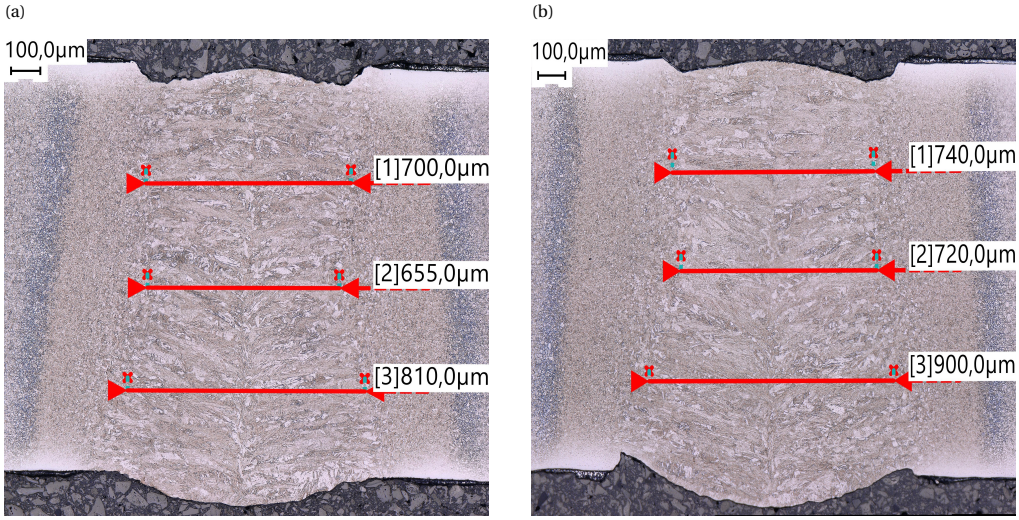

Figure 6.9: Size of the fusion zone in DP-1 steel from tests conducted with laser-1 at a spot size of 0.6 mm obtained using collimator lens movement in (a), and laser head movement in (b).

Shape of fusion zone- From previous studies it was reported that welds made in open keyhole mode welding tend to have an hour glass shape with nearly equal weld bead width at the top and bottom [16]. For open keyhole mode welds made at Delft in DP-1, DP-2 and TRIP steel, the observed shape of the fusion zone can be discussed as two cases, depending on the placement of the focal plane of the objective lens with respect to the workpiece. In the first case, the focal plane of the objective lens coincides with the top surface of the plate and the resulting hourglass shape of the fusion zone has a nearly equal width at the top and bottom. This was observed for bead-on-plate welds made with laser-1 at a spot size of 0.2 mm and laser-2 at a spot size of 0.6 mm for which the transverse cross section of the alloys are shown in Chapter 4, Fig. 4.20 and 4.17, for laser-1 and laser-2, respectively. In the second case, the focal plane of the objective lens remains above the workpiece due to de-focusing of the beam to obtain a laser beam spot diameter of 0.6 mm (laser-1). Due to this, a continuously diverging beam is incident on the surface of the workpiece which may cause the heat source (keyhole) to widen at the bottom. The resulting weld bead width in this case is wider at the bottom in comparison to the top. The transverse cross section of the open keyhole mode bead-on-plate weld using laser-1 at a spot size of 0.6 mm on DP-1 steel is shown in Fig. 6.9, and supports this observation. A difference in the morphology of the shape of the fusion zone in the open keyhole mode welding is observed due to de-focusing of the laser beam. Additionally, the welding speed was also found to influence the morphology of the shape of the fusion zone during the open keyhole mode welding. As the welding speed is reduced, while keeping the laser power and spot size constant, the keyhole shifts towards the open keyhole configuration and the hourglass shape of the fusion zone is wider at the top than the bottom. This was observed for bead-on-plate welds made with laser-2 on DP-1 steel at a spot size of 0.6 mm when the welding speed was reduced from 167.0 $mm{\cdot}s^{-1}$ to 156.7 $mm{\cdot}s^{-1}$ as shown in Fig. 6.6 a and b. Similarly, this was also observed for bead-on-plate welds made at a spot size of 0.2 mm with laser-1 on DP-2 steel while reducing the welding speed from 176.0 $mm{\cdot}s^{-1}$ to 167.0 $mm{\cdot}s^{-1}$, as shown in Chapter 4, Fig. 4.21 a and b, respectively. To summarise, the morphology of the shape of the fusion zone during the open keyhole mode welding is affected by de-focusing of the laser beam and welding speed. Further study in terms of quantifying the effect of the changing fusion zone morphology on micro-segregation along the weld centreline could provide insight on how the solidification cracking tendency is affected.

6.4 WELD POOL SHAPE AND PROCESS EFFICIENCY

Weld pool shape- It is known that welding at high speeds facilitates the formation of teardrop shaped weld pools.The numerically determined shape of the weld pool is shown in Chapter 5, Fig. 5.4 and 5.6, for DP-1 steel and TRIP steel, respectively. For both alloys the shape of the weld pool for various spot sizes of the laser beam remains teardrop. Therefore, changing the spot size at constant laser power and welding speed is found to have no effect on the shape of the weld pool. Furthermore, the composition of the two alloys has relatively no impact on the shape of the weld pool when the welding speed is considerably high. The predicted shape of the weld pool was verified from the micrographs of the weld metal top surface as shown in Fig. 6.10 a and b, for DP-1 and TRIP steel, respectively. It can be observed that the solidified grains follow epitaxial growth from the fusion lines and impinge at the weld centreline where bending of grains is not observed, which confirms the teardrop shape of the weld pool. Teardrop shaped weld pools have a tendency to cause increased weld centreline segregation due to the morphology of solidifying grains and increased strain localisation on the centreline grain boundary. Due to this, a weld pool with teardrop shape increases the susceptibility of an alloy to solidification cracking.

In case of bead-on-plate laser welding of DP-1 and TRIP steel with a spot size of 0.2 mm and at the critical

spot size, i.e. 0.25 mm in TRIP steel and 0.40 mm in DP-1 steel, even though a teardrop weld pool shape prevails, solidification cracking is not observed. This could be attributed to the reduced size of the fusion zone when smaller spot sizes are used during LBW which facilitate the open keyhole mode welding. Another possible explanation could be the finer grain structure in the weld metal when smaller spot sizes are used in comparison to a spot size of 0.6 mm. Finer grains reduce the extent of strain localisation at the centreline grain boundary, which in turn reduces the susceptibility to solidification cracking.

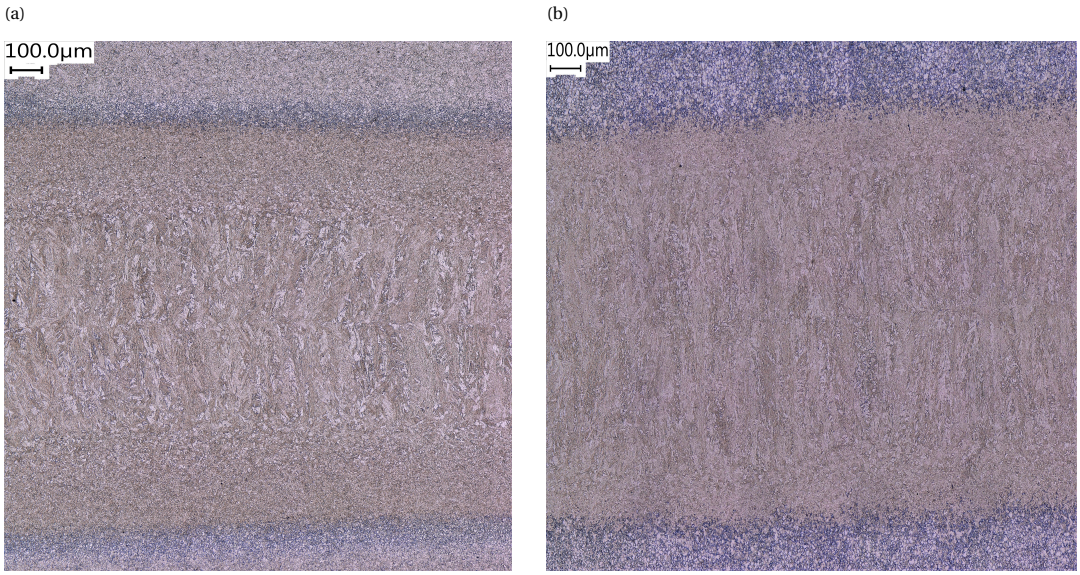

Figure 6.10: Macrograph of the top surface of the bead-on-plate laser weld in (a), DP-1 steel and (b), TRIP steel.

Weld pool and mushy zone size- The size of the weld pool and the mushy zone in DP-1 steel and TRIP steel is obtained numerically and it was observed that in both alloys the size of the weld pool and mushy zone increases as the laser beam spot diameter increases. This is because a larger spot size of the laser beam facilitates increased laser beam absorption by the material. However, the size of the weld pool and mushy zone is larger in TRIP steel when compared to DP-1 steel. This can attributed to the larger solidification temperature range of TRIP steel (194 K) in comparison to DP-1 steel (78 K). This also affects the critical weld size below which solidification cracking does not occur, and in TRIP steel (0.5 mm wide) it is smaller in comparison to DP-1 steel (0.6 mm wide). An extended weld pool and mushy zone forms during LBW of TRIP steel due to its metallurgy (high phosphorous content, large solidification temperature range), which makes it most susceptible to solidification cracking.

LBW process efficiency- Efficiency of the LBW process for DP-1 steel and TRIP steel is shown in Fig. 5.8 a and b, respectively. For both alloys, there is a good agreement between the numerically obtained and analytically calculated process efficiency when the spot size is 0.20 mm which corresponds to a specific energy value of 120.0 J·mm^{-2}. In this case, the keyhole was found to exist in an open configuration for both alloys. However, a poor agreement is found between the two efficiency values when the laser beam spot size is 0.60 mm which corresponds to a specific energy value of 40.0 J·mm^{-2}. In this case, the keyhole exists in the closed keyhole and random open/closed keyhole configuration for TRIP steel. Whereas, for DP-1 steel the keyhole exists more towards the open keyhole configuration in addition to just closed keyhole configuration. The analytically calculated process efficiency for TRIP steel is 104 %, and for DP-1 steel is 99.5 %, when the keyhole exists in the closed keyhole configuration. Clearly, these values are unrealistic and are a result of the increased cross sectional area of the fusion zone due to the closed configuration of the keyhole. In DP-1 steel when the

Table 6.1: Numerical and analytical critical efficiency of the LBW process for DP-1 steel and TRIP steel.

Material	Critical efficiency (%)	
	Analytical	Numerical
DP-1 steel	53	60
TRIP steel	41	44

keyhole exists more towards open keyhole configuration a reasonable agreement can be observed in the numerical and analytical process efficiency. The efficiency values can be seen to drop a little in TRIP steel when the keyhole is in the random open/closed keyhole configuration, but still remains significantly higher than the numerically determined process efficiency. A strong dependence of the Fuerschbach model (Equation 3.7 in Chapter 3) on the cross sectional area of the weld can be observed. This signifies that the application of the model to predict the efficiency during LBW is limited and can only be used when the combination of processing conditions (laser power, welding speed and spot size), result in the open keyhole configuration welding. It was also observed that below a certain critical weld size, solidification cracking was not observed in DP-1 and TRIP steel. For this weld size, the critical process efficiency during LBW is determined numerically and analytically. This critical efficiency of the process is representative of the critical heat input above which solidification cracking occurs. Therefore, the critical efficiency of the process can serve as a parameter to choose a set of welding conditions such that the critical heat input or efficiency is not exceeded and solidification cracking is mitigated. In Table 6.1, the numerical and analytical process efficiency is presented for DP-1 and TRIP steel. The critical spot size corresponding to the critical process efficiency resulted in the open keyhole configuration welding in both, DP-1 and TRIP steel. As mentioned earlier, the application of the analytical model to calculate the process efficiency is viable during the open keyhole mode welding. Due to this a reasonable agreement can also be observed between the analytical and numerical critical process efficiency. The accuracy of the numerical model to predict the temperature cycle, weld pool shape and process efficiency is mainly dependent on the availability of high temperature material properties. Since these properties were readily available for TRIP steel and were determined for DP-1 steel from a similar third generation AHSS, the agreement between the numerical and experimental values is much better for TRIP steel in comparison to DP-1 steel.

6.5 METALLURGICAL CONTRIBUTION TO SOLIDIFICATION CRACKING

In Chapter 4, Fig. 4.19, the average crack length of the three alloys is plotted against the area of the fusion zone. A trend can be observed between the recorded average lengths and the cross section area of the fusion zone. As the macroscopic area of the fusion zone increases the average solidification crack length also increases. It can be concluded that the size of the fusion zone corroborates with the solidification cracking tendency of the alloys. However, for similar areas of the fusion zone in DP-1, DP-2 and TRIP steel, the average crack length is highest for TRIP steel, followed by DP-1 and DP-2 steel. Additionally, the critical spot size, weld size and process efficiency above which solidification cracking occurs is higher for DP-1 steel in comparison to TRIP steel. These results point towards the contribution of the metallurgy of an alloy to solidification cracking. TRIP steel has a higher P content (0.089 wt. %) in the base metal when compared to DP-1 (0.01 wt. %) and DP-2 (0.009 wt. %) steel. During solidification, phosphorous in steel segregates to grain boundaries and has a tendency of forming the low melting-point Fe-Fe_3P eutectic (1321 K), which results in a broadened solidification range of the alloy. Segregation of phosphorous in the weld metal of TRIP steel at the prior

austenitic grain boundaries was previously confirmed through EPMA [81].

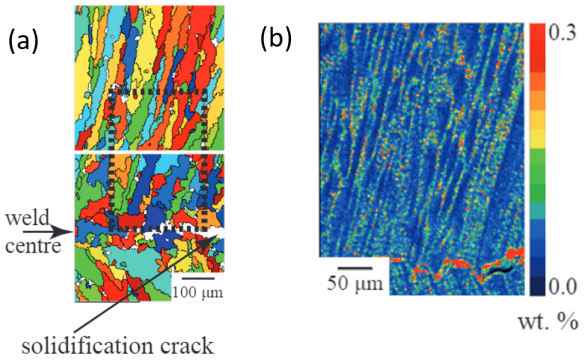

Figure 6.11: Phosphorous elemental map in TRIP steel (b) corresponding to the weld metal region in (a) [81]

In Fig. 6.11 a, the prior austenite grains in the weld metal of TRIP steel are revealed from EBSD and the corresponding phosphorus elemental map is shown in Fig. 6.11 b, which gives the evidence of phosphorous segregation at prior austenite grain boundaries. Due to this, the non-equilibrium solidification temperature range is highest in TRIP steel, followed by DP-1 steel and DP-2 steel. The broadened solidification temperature range results in an elongated weld pool and mushy region in TRIP steel in comparison to DP-1 steel at similar welding parameters. Therefore, near the terminal stage of solidification, there is an increased likelihood of greater stress/strain build-up at the centreline liquid film boundary in the mushy region of TRIP steel. Because of this the mushy region in TRIP steel is rather weak in comparison to DP-1 steel. Consequently, the critical spot size, weld size and the process efficiency is lower for TRIP steel and it is rendered as the most susceptible to solidification cracking followed by DP-1 steel and DP-2 steel.

7

CONCLUSIONS AND SCOPE FOR FURTHER RESEARCH

7.1 CONCLUSIONS

The conclusions arising from the results and discussion presented previously are stated below:

- Testing of AHSS alloys at different LBW facilities resulted in variations in the measured average crack lengths, while maintaining the welding parameters constant. This was due to differences in quality and spatial intensity distribution of the laser beam which changed the keyhole configuration during LBW and consequently the solidification cracking tendency of the alloys.
- Solidification cracking can be completely avoided if a smaller spot size of the laser beam is utilised during welding which results in a narrow weld bead. This has proven to be effective even for TRIP steel with significant phosphorus content, and without compromising the welding speed.
- If a LBW facility is limited in terms of choices for the laser beam spot size then, an open configuration of the keyhole is effective in reducing the solidification cracking tendency. This can be achieved by careful selection of other welding parameters namely, welding speed and laser power.
- While changing the spot size during LBW, a critical spot size of the laser beam can be identified which results in a critical size of the weld above which solidification cracking occurs in alloys. Below the critical weld size, thermo-mechanical and metallurgical conditions necessary for solidification cracking are not significant. Corresponding to this critical spot size and weld size, a critical efficiency of the process can be obtained which can serve as a parameter to select optimum process parameters such that solidification cracking does not occur. The magnitude of the critical spot size is influenced by the solidification cracking susceptibility of the alloy in consideration, which in turn is dependent on the metallurgy. In general, as the susceptibility to solidification cracking increases, the critical spot size at which solidification cracking is mitigated decreases.

- Numerical modelling is useful for predicting the weld pool shape and process efficiency during laser beam welding. The changes in the size of the weld (fusion zone) and the mushy zone are well captured by the numerical models. Therefore, for a set of welding conditions the numerical tools could be used to comment on the solidification cracking tendency of an alloy a priori. On the other hand, application of the analytical model to obtain the process efficiency under various processing conditions is limited to the open keyhole configuration.

7.2 SCOPE FOR FUTURE RESEARCH

On the basis of the present study, the following possibilities can be explored for further research:

- A fundamental study can be undertaken to understand why DP-1 steel, which has a lean compositions, is susceptible to solidification cracking. DP-2 steel is a similar third generation AHSS, but has a significantly lower susceptibility to solidification cracking. Therefore, the two steels can be analysed together and the results can be compared to determine what is responsible for promoting solidification cracking in DP-1 steel.
- For the various processing conditions identified to have an impact the solidification cracking tendency of AHSS, advanced characterisation tools such as, EPMA and EBSD, can be utilised to quantify their contribution in promoting segregation of elements like phosphorous and boron *etc.* SEM-EDS was utilised to gain information on solute distribution in the fusion zone following bead-on-plate laser welding however, the results were inconclusive.
- Corresponding to the critical size of the weld above which alloys are susceptible to solidification cracking, the threshold strain can be determined.
- To further build upon the understanding of the influence of laser beam characteristics on solidification cracking, alloys can be tested at LBW facilities with differences in spatial intensity distribution and quality of the laser beam.

GLOSSARY

AHSS Advanced High Strength Steels.

BIW Body-in-White.

BTR Brittle Temperature Range.

CK Closed Keyhole.

CO_2 Carbon Dioxide.

CST Critical Strain Tangent.

DP Dual Phase.

LBW Laser Beam Welding.

OK Open Keyhole.

SEM Scanning Electron Microscope.

TRIP Transformation Induced Plasticity.

ULSAB Ultr-Light Steel Auto Body.

BIBLIOGRAPHY

[1] WORLDSTEELASSOCIATION, *World steel in figures 2019,* (2019).

[2] WORLDSTEELASSOCIATION, *Steel in automotive,* (2019).

[3] Audi media centre, *Audi a4,* (2019).

[4] P. G. Schurter, *ULSAB-advanced vehicle concepts–manufacturing and processes*, Tech. Rep. (SAE Technical Paper, 2002).

[5] M. Shome and M. Tumuluru, *Welding and joining of advanced high strength steels (AHSS)*, 85 (Elsevier, 2015).

[6] S. Riches, *Industrial laser and applications in automotive welding,* Lasers in the Automotive Industry, październik (1998).

[7] A. M. Lokka, *An economic evaluation of tailor welded blanks in automotive applications*, Ph.D. thesis, Massachusetts Institute of Technology (1997).

[8] National Oceanic and Atmospheric Administration, *Atmospheric co_2,* (2019).

[9] J. Svenungsson, I. Choquet, and A. F. Kaplan, *Laser welding process–a review of keyhole welding modelling,* Physics procedia **78**, 182 (2015).

[10] L. Quintino, A. Costa, R. Miranda, D. Yapp, V. Kumar, and C. Kong, *Welding with high power fiber lasers–a preliminary study,* Materials & Design **28**, 1231 (2007).

[11] S. Shi and S. Westgate, *Laser welding of ultra-high strength steels for automotive applications,* in *Pacific International Conference on Applications of Lasers and Optics*, Vol. 2008 (Laser Institute of America, 2008) pp. 134–139.

[12] A. Y. Nee, *Handbook of manufacturing engineering and technology* (Springer, 2015).

[13] K.-M. Hong and Y. C. Shin, *Prospects of laser welding technology in the automotive industry: A review,* Journal of Materials Processing Technology **245**, 46 (2017).

[14] T. Ltd, *How does laser welding work,* (2012).

[15] M. Y. Krasnoperov, R. R. Pieters, and I. M. Richardson, *Solidification features of the thin steel sheets in keyhole welding,* ICALEO 2003 - 22nd International Congress on Applications of Laser and Electro-Optics, Congress Proceedings **509** (2003), 10.2351/1.5060151.

[16] M. Y. Krasnoperov, R. R. Pieters, and I. M. Richardson, *Weld pool geometry during keyhole laser welding of thin steel sheets,* Science and Technology of Welding and Joining **9**, 501 (2004).

[17] G. Agarwal, *Study of solidification cracking during laser welding in advanced high strength steels: A combined experimental and numerical approach*, Ph.D. thesis, Delft University of Technology (2019).

[18] Wikiwand, *Weld pool,* (2012).

[19] C. Heiple, H. CR, *et al., Mechanism for minor element effect on gta fusion zone geometry,* (1982).

[20] R. Trivedi, S. David, M. Eshelman, J. Vitek, S. Babu, T. Hong, and T. DebRoy, *In situ observations of weld pool solidification using transparent metal-analog systems,* Journal of applied physics **93**, 4885 (2003).

[21] R. Kuziak, R. Kawalla, and S. Waengler, *Advanced high strength steels for automotive industry: A review,* Archives of Civil and Mechanical Engineering **8**, 103 (2008).

[22] T. Nanda, V. Singh, V. Singh, A. Chakraborty, and S. Sharma, *Third generation of advanced high-strength steels: Processing routes and properties,* Proceedings of the Institution of Mechanical Engineers, Part L: Journal of Materials: Design and Applications **233**, 209 (2019).

[23] T. Hilditch, T. de Souza, and P. Hodgson, *Properties and automotive applications of advanced high-strength steels (ahss),* in *Welding and Joining of Advanced High Strength Steels (AHSS)* (Elsevier, 2015) pp. 9–28.

[24] B. Ma, *A Study of Processing, Microstructure and Mechanical Properties of Ultra-High Strength Microalloyed Steel Hot Band Coils for Automotive Applications*, Ph.D. thesis, University of Pittsburgh (2017).

[25] O. Kwon, K. Lee, G. Kim, and K. G. Chin, *New trends in advanced high strength steel developments for automotive application,* Materials Science Forum **638-642**, 136 (2010).

[26] M. Rossini, P. R. Spena, L. Cortese, P. Matteis, and D. Firrao, *Investigation on dissimilar laser welding of advanced high strength steel sheets for the automotive industry,* Materials Science and Engineering: A **628**, 288 (2015).

[27] J. H. Schmitt and T. Iung, *New developments of advanced high-strength steels for automotive applications,* Comptes Rendus Physique **19**, 641 (2018).

[28] D. K. Matlock and J. G. Speer, *Third Generation of AHSS: Microstructure Design Concepts,* Microstructure and Texture in Steels , 185 (2009).

[29] O. Bouaziz, H. Zurob, and M. Huang, *Driving force and logic of development of advanced high strength steels for automotive applications,* Steel Research International **84**, 937 (2013).

[30] C. C. Tasan, M. Diehl, D. Yan, M. Bechtold, F. Roters, L. Schemmann, C. Zheng, N. Peranio, D. Ponge, M. Koyama, *et al., An overview of dual-phase steels: advances in microstructure-oriented processing and micromechanically guided design,* Annual Review of Materials Research **45**, 391 (2015).

[31] ArcelorMittal Global Automotive & Mobility Solutions, *Dual phase steels,* (2019).

[32] W. Bleck, X. Guo, and Y. Ma, *The trip effect and its application in cold formable sheet steels,* steel research international **88**, 1700218 (2017).

[33] K. Hansson and H. Fredriksson, *Influence of cooling rate on the hot cracking formation of nickel rich alloys,* ISIJ international **42**, 512 (2002).

[34] D. G. Eskin and L. Katgerman, *A quest for a new hot tearing criterion,* Metallurgical and Materials Transactions A: Physical Metallurgy and Materials Science **38 A**, 1511 (2007).

[35] S. Kou, *A criterion for cracking during solidification,* Acta Materialia **88**, 366 (2015).

[36] S. Kou, *Welding metallurgy* (John Wiley & sons, 2003).

[37] S. Kou, *Solidification and liquation cracking issues in welding,* Jom **55**, 37 (2003).

[38] K. Easterling, *Introduction to the physical metallurgy of welding* (Elsevier, 2013).

[39] J. C. Lippold *et al.*, *Welding metallurgy and weldability* (Wiley Online Library, 2015).

[40] W. Pumphrey, *A consideration of the nature of brittleness at temperatures above the solidus in castings and welds in aluminium alloys,* J. of the Inst. of Metals **75**, 235 (1948).

[41] P. Kammer, K. Masubuchi, and R. Monroe, *Cracking in High-strength Steel Weldments: A Critical Review,* Vol. 197 (Defense Metals Information Center, Battelle Memorial Institute, 1964).

[42] W. Pellini, *Strain theory of hot tearing,* Foundry **80**, 125 (1952).

[43] D. G. Eskin, Suyitno, and L. Katgerman, *Mechanical properties in the semi-solid state and hot tearing of aluminium alloys,* Progress in Materials Science **49**, 629 (2004).

[44] J. Borland, *Generalized theory of super-solidus cracking in welds,* Br. Weld. J. **7**, 508 (1960).

[45] V. Shankar, T. P. Gill, S. L. Mannan, and S. Sundarlsan, *Solidification cracking in austenitic stainless steel welds,* Sadhana - Academy Proceedings in Engineering Sciences **28**, 359 (2003).

[46] F. MATSUDA, H. NAKAGAWA, and K. SORADA, *Dynamic observation of solidification and solidification cracking during welding with optical microscope (i): Solidification front and behavior of cracking (materials, metallurgy & weldability),* Transactions of JWRI **11**, 67 (1982).

[47] D. Manitsas and J. Andersson, *Hot cracking mechanisms in welding metallurgy: A review of theoretical approaches,* in *MATEC Web of Conferences*, Vol. 188 (EDP Sciences, 2018) p. 03018.

[48] N. Prokhorov and N. N. Prokhorov, *Fundamentals of the theory for technological strength of metals while crystallising during welding,* Transactions of the Japan Welding Society **2**, 205 (1971).

[49] J. C. Lippold, *Characterization of Weld Solidification Cracking in a Duplex Stainless Steel Introduction Duplex stainless steels have become an important alternative to con- ventional austenitic stainless steels in marine , petroleum , and chemical processing applicatio,* **19**, 1 (1989).

[50] T. Böllinghaus and H. Herold, *Hot cracking phenomena in welds* (Springer Science, 2005).

[51] N. Coniglio and C. E. Cross, *Mechanisms for solidification crack initiation and growth in aluminum welding,* Metallurgical and Materials Transactions A **40**, 2718 (2009).

[52] C. E. Cross, *On the origin of weld solidification cracking,* Hot Cracking Phenomena in Welds , 3 (2005).

[53] F. Matsuda *et al.*, *Solidification crack susceptibility of weld metal,* in *Recent Trends in Welding Science and Technology* (ASM International Metals Park, OH, 1990) pp. 127–136.

[54] J. Lippold, *Solidification behavior and cracking susceptibility of pulsed-laser welds in austenitic stainless steels,* Welding Journal Including Welding Research Supplement **73**, 129s (1994).

[55] F. C. Hull, *Effect of delta ferrite on the hot cracking of stainless steel,* WELD J **46**, 399 (1967).

[56] K. Nishimoto, K. Saida, K. Kiuchi, and J. Nakayama, *Hot Cracking Phenomena in Welds III* (2011) pp. 183–208.

[57] U. Feurer, *Influence of alloy composition and solidification conditions on dendrite arm spacing, feeding and hot tearing properties of aluminum alloys,* in *Qual. Control Eng. Alloys Role Met. Sci, Proc. Int. Symp* (1977) pp. 131–145.

[58] T. Zacharia *et al.*, *Dynamic stresses in weld metal hot cracking,* Welding Journal Including Welding Research Supplement **73**, 164 (1994).

[59] T. Kannengiesser and T. Boellinghaus, *Hot cracking tests - An overview of present technologies and applications,* Welding in the World **58**, 397 (2014).

[60] N. Prokhorov, *The problem of the strength of metals while solidifying during welding,* Svarochnoe Proizvodstvo **6**, 5 (1956).

[61] T. Senda, F. Matsuda, and G. Takano, *Solidification crack susceptibility for weld metals with the transvarestraint test. pt. 2. commercially used aluminum and aluminum alloys,* Yosetsu Gakkai- Shi **42**, 48 (1973).

[62] G. Agarwal, A. Kumar, H. Gao, M. Amirthalingam, S. C. Moon, R. J. Dippenaar, I. Richardson, and M. Hermans, *Study of solidification cracking in a transformation-induced plasticity-aided steel,* Metallurgical and Materials Transactions A **49**, 1015 (2018).

[63] H. Gao, G. Agarwal, M. Amirthalingam, and M. Hermans, *Hot cracking investigation during laser welding of high-strength steels with multi-scale modelling approach,* Science and Technology of Welding and Joining **23**, 287 (2018).

[64] C. E. Cross and N. Coniglio, *Weld solidification cracking: Critical conditions for crack initiation and growth,* Hot Cracking Phenomena in Welds II , 39 (2008).

[65] Y.-C. Zhang, H. Nakagawa, and F. Matsuda, *Development of restraint-relaxation u-form hot cracking device,* Transactions of JWRI **15**, 159 (1986).

[66] K. Shinozaki, H. Kuroki, X. Luo, H. Ariyoshi, and M. Shirai, *Comparison of hot cracking susceptibilities of various ni-base, heat-resistant superalloys by u-type hot cracking test. study of laser weldability of ni-base, heat-resistant superalloys (2nd report),* Welding international **13**, 952 (1999).

[67] I. Woo, C. Kang, and K. Nishimoto, *Influence of electron beam welding parameters and metallurgical factors on intergranular liquation cracking susceptibility of cast alloy 718,* Metals and Materials International **7**, 349 (2001).

[68] PRIMES, *Focusmonitorfm+,* (2019).

[69] R. Paschotta *et al.*, *Encyclopedia of laser physics and technology*, Vol. 1 (Wiley Online Library, 2008).

[70] Y. Leng, *Materials characterization: introduction to microscopic and spectroscopic methods* (John Wiley & Sons, 2009).

[71] E. Madenci and I. Guven, *The finite element method and applications in engineering using ANSYS®* (Springer, 2015).

[72] P. Lamberg, R. Lehtiniemi, and A.-M. Henell, *Numerical and experimental investigation of melting and freezing processes in phase change material storage,* International Journal of Thermal Sciences **43**, 277 (2004).

[73] E. A. A. Ahmed and U. Reisgen, *Laser welding of advanced high strength steels*, RWTH-CONV-125622 (Lehrstuhl und Institut für Schweißtechnik und Fügetechnik, 2011).

[74] H. Gao, *Residual stress development due to high-frequency post weld impact treatments for high-strength steels,* (2014).

[75] E. M. Van der Aa, *Local cooling during welding: prediction and control of residual stresses and buckling distortion,* (2007).

[76] K. Gillen-Christandl, G. D. Gillen, M. Piotrowicz, and M. Saffman, *Comparison of gaussian and super gaussian laser beams for addressing atomic qubits,* Applied Physics B **122**, 131 (2016).

[77] P. Fuerschbach, *Measurement and prediction of energy transfer efficiency in laser beam welding,* Welding Journal **75** (1996).

[78] C. Walsh, H. Bhadeshia, A. Lau, B. Matthias, R. Oesterlein, and J. Drechsel, *Characteristics of high-power diode–laser welds for industrial assembly,* Journal of Laser Applications **15**, 68 (2003).

[79] M. Y. Krasnoperov, R. R. Pieters, and I. M. Richardson, *Laser welding of thin steel sheets: Energy transfer efficiency,* PICALO 2004 - 1st Pacific International Conference on Applications of Laser and Optics, Conference Proceedings **207**, 33 (2004).

[80] C. Hagenlocher, D. Weller, R. Weber, and T. Graf, *Analytical Description of the Influence of the Welding Parameters on the Hot Cracking Susceptibility of Laser Beam Welds in Aluminum Alloys,* Metallurgical and Materials Transactions A: Physical Metallurgy and Materials Science **50**, 5174 (2019).

[81] G. Agarwal, A. Kumar, I. Richardson, and M. Hermans, *Evaluation of solidification cracking susceptibility during laser welding in advanced high strength automotive steels,* Materials & Design **183**, 108104 (2019).